DISSERTATION

PCB Thermal Flow Sensor for Heating, Ventilating, and Air Cooling Systems

ausgeführt zum Zwecke der Erlangung des akademischen Grades
eines Doktors der technischen Wissenschaften unter der Leitung von

Ao. Univ.-Prof. Dipl.Ing Dr. Franz Keplinger
Institut für Sensor- und Aktuatorsysteme

eingereicht an der Technischen Universität Wien
Fakultät für Elektrotechnik und Informationstechnik

von

Thomas Glatzl
Matr.-Nr. 1128905

Wien, im Oktober 2017

Supervisor:	*Ao. Univ.-Prof. Dr. Franz Keplinger*
Co-supervisor:	*Dr. Franz Kohl*

Referee I:	*Ao. Univ.-Prof. Dr. Franz Keplinger*
	Institute of Sensor and Actuator Systems
	Vienna University of Technology, Austria
Referee II:	*Priv.-Doz. Dr. Hubert Brückl*
	Center of Integrated Sensor Systems
	Danube University Krems, Austria

The research presented in this thesis was carried out at the Institute of Sensor and Actuator Systems, Vienna University of Technology and the Center for Integrated Sensor Systems, Danube University Krems, Wiener Neustadt.

This work was supported by the European Regional Development Fund, the province of Lower Austria, and the Austrian Research Promotion Agency (LISE and ESENSE Projects, Project Nr.: 834175 and 834481).

"Happiness lies not in the mere possession of money. It lies in the joy of achievement, in the thrill of creative effort."

Franklin D. Roosevelt

"If you cannot measure it, you cannot improve it."

William Thomson, 1. Baron Kelvin

"Give me a lever long enough and a fulcrum on which to place it, and I shall move the world. "

Archimedes of Syracuse

Contents

Kurzfassung

Ein erheblicher Teil der produzierten Energie fließt in Gebäude wo wiederum sehr viel von sogenannten HLK (Heitzung, Lüftung, Klima) Anlagen verbraucht wird. Um den Energieverbrauch von solchen Anlagen reduzieren zu können, muss man zuerst den aktuellen Zustand erfassen. Dafür können unterschiedliche Parameter wie Temperatur, Feuchtigkeit, Strömungsgeschwindigkeit, Druck, Dichte, CO_2 Anteil, usw, mit verschiedensten Sensoren gemessen werden. Die Messung all dieser Parameter in jedem Raum oder Kanal ist jedoch weder energieeffizient noch unbedingt nötig. Durch Messung des Volumenstroms an strategisch günstigen Positionen kann bereits eine Aussage über Ineffizienz und möglichem Einsparungspotential getroffen werden.

Ziel dieser Arbeit ist das Design und ein proof-of-concept eines thermischen Strömungssensors welcher nur mit der Printplattentechnologie hergestellt wird. Es werden zwei Auslesemethoden des kalorimetrischen Prinzips angewendet, wobei bei der ersten ein konstanter Strom durch eine Kupferbahn fließt und die von der Strömungsgeschwindigkeit abhängige Übertemperatur durch umliegende Sensorelemente gemessen wird. Bei der zweiten Methode hält ein Regler eine definierte Übertemperatur mittels einer Heizspannung konstant. Mit steigender Geschwindigkeit muss der Regler mehr heizen und damit wird die Heizspannung abhängig von der Strömungsgeschwindigkeit.

Ein analytisches Modell und FEM Simulationen wurden erstellt um das Prinzip zu testen. Verschiedene Wandlerdesigns wurden entwickelt, hergestellt und mittels verschiedener Experimente charakterisiert. Der Fokus der Experimente liegt auf reproduzierbaren Widerstandswerten welche die größte Herausforderung darstellten wie auch das zeitliche Verhalten der Kupferbahnen. In Experimenten mit einem Lock-in Verstärker wurde die Strömungsabhängigkeit der Sensoren gemessen. Abschließend wurden die Sensoren in einer realen HLK Anlage getestet und damit der proof-of-concept des neuen Konzepts erbracht.

Abstract

An considerable amount (about 39 quadrillion British thermal units) of the energy produced was consumed by the residential and commercial sectors, which is mostly building related for heating, cooling, and lighting. More than one third of this energy is consumed by so-called heating, ventilating, and air conditioning (HVAC) systems. To reduce this energy consumption the installation of a sufficiently large number of sensors is required to obtain a detailed picture of the actual state of the HVAC system by sensing parameters like temperature, humidity, air flow velocity, flow, but also pressure, density, and CO2-concentration. However, placing various sensors to measure all these parameters in each room is neither energy efficient nor necessary. Simply measuring the volume flow rate at strategic points will reveal inefficiency and cost-reduction potential.

The aim of this work is the design and a proof-of-concept of a thermal flow sensor that is only based on PCB technology. The calorimetric principle is envisioned for the readout method where two operation modes are investigated, constant current and constant temperature mode. At the constant current mode, a specific current heats up a copper lead of the PCB sensor and surrounding sensing elements evaluate the excess temperature which is flow dependent. At the constant temperature mode, a controller keeps a specific excess temperature between the sensing elements at a constant level. With increasing flow velocity, the controller has to adjust the heating to maintain this specific excess temperature, therefore, the heating voltage becomes a function of the flow velocity.

An analytical model is set up followed by FEM simulations to verify that the targeted principle is feasible. Several sensor designs are developed, fabricated, and then characterized with measurements. These measurements focus on resistance values as well as the transient behavior of the copper leads, experiments with a lock-in amplifier reveal the flow dependency of the sensor, and experiments in a real HVAC system prove the concept feasible.

Nomenclature

Abbreviations

µC	Micro Controller
AC	Alternating Current
ADC	Analog Digital Converter
API	Application Programming Interface
AVC	Automatic Voltage Control
CAD	Computer Aided Design
CCA	Constant Current Anemometer
CFD	Computational Fluid Dynamics
CMOS	Complementary Metal Oxide Semiconductor
CT	Constant Temperature
CTA	Constant Temperature Anemometer
DAC	Digital Analog Converter
DC	Direct Current
FEM	Finite Element Method
GPIB	General Purpose Instrumentation Bus
Gr	Grashof number
HDF	Hierarchical Data Format
HVAC	Heating, Ventilating, and Air Conditioning
IC	Integrated Circuit

IQR	Interquartile Range
MEMS	Micro Electro Mechanical Systems
Nu	Nusselt number
OpAmp	Operational Amplifier
PC	Personal Computer
PCB	Printed Circuit Board
PLL	Phase Locked Loop
Pr	Prantl number
PSD	Pase Sensitive Detection
Re	Reynolds number
RMS	Root Mean Square
TCR	Temperature Coefficient of Resistance
USB	Universal Serial Bus

Constants

c	Speed of light	$299792458\,\mathrm{m/s}$
e	Elementary charge	$1.602176462 \cdot 10^{-19}\,\mathrm{C}$
g	Gravitational acceleration	$9.80665\,\mathrm{m/s^2}$
h_c	Planck constant	$6.62606876 \cdot 10^{-34}\,\mathrm{Js}$
K	Boltzmann constant	$1.3806503 \cdot 10^{-23}\,\mathrm{J/K}$

Symbols

α_ht	Heat flow coefficient	$\mathrm{W/(m^2K)}$
α_R	Adsorption ratio	1
α_s	Thermoelectric (Seebeck) coefficient	V/K
α_TCR	Temperature coefficient of resistance	1/K

$\bar{v}_{1,2}$	Mean flow velocites	m/s
$\bar{v}_{\mathrm{a}}$	Mean flow velocity	m/s
β	Thermal expansion coefficient	1/K
$\dot{m}$	Mass flow rate	kg/s
$\dot{Q}$	Heat flux	W
$\dot{q}$	Heat flux density	$\mathrm{W/m^2}$
$\dot{V}$	Volume flow	$\mathrm{m^3/s}$
η	Dynamic viscosity	Pa s
λ	Thermal conductivity	W/(mK)
$\mathrm{d}p_{\mathrm{corr}}$	Differential pressure offset corrected	Pa
$\mathrm{d}p$	Differential pressure	Pa
ν	Kinematic viscosity	$\mathrm{m^2/s}$
ρ_{R}	Transmission ration	1
τ_{R}	Reflection ratio	1
ε	Emission ratio	1
φ	Humidity	1
ϖ	Fluidity	$\mathrm{m^2/Ns}$
ϱ	Density	$\mathrm{kg/m^3}$
ς	Volume viscosity	$\mathrm{Ns/m^2}$
ϑ	Temperature	°C
Υ	Inflow velocity	m/s
$\vec{\Gamma}_{\mathrm{fluid}}(\vec{r},t)$	Rotation of a fluid	$\mathrm{s^{-1}}$
$\vec{\omega}$	Energy density	$\mathrm{J/m^3}$
$\vec{v}$	Velocity of fluid particles	m/s
$\vec{F}$	Force	N
$\vec{f}$	Outer accerleration	$\mathrm{m/s^2}$
$\vec{F}_{\mathrm{a}}$	Outer force	N
$\vec{F}_{\mathrm{p}}$	Pressure force	N

$\vec{F}_{\mathrm{R}}$	Friction force	N
$\vec{j}$	Mass flow density	kg/(m^{2}s)
$\vec{n}$	Normal vector	m
$\vec{r}$	Position vector	m
A	Area	m^2
a	Thermal diffuivity	m/s^2
c_{p}	Specific heat capacity	J/(kgK)
E	Heat	J
h	Specific enthalpie	J
I_{C}	Collector current	A
I_{R}	Reference current	A
L	Chracterisitc length	m
m	Mass of the fluid	kg
m_{T}	Mass of a fluid particle	kg
p	Pressure	N/m^2
$Q_{\mathrm{fluid}}(\vec{r}, t)$	Divergence of a fluid	s^{-1}
R	Electrical resistance	Ω
R_0	Electrical resistance at temperature T_0	Ω
S	Entropy	J/K
s	Specific entropy	J/(K kg)
T	Temperature	K
t	Time	s
T_0	Reference temperature	K
u	Characterisitc flow veloctiy	m/s
U_{BE}	Voltage drop of a base-emitter junction	V
U_{TES}	Emerging voltage of a thermoelectric Sensor	V
V_{G}	Material band gap	V
V_{T}	Volume of a fluid particle	m^3

Chapter 1

Introduction

This work aims on the design, fabrication and implementation of thermal flow sensors. Due to the large number of flow measuring principles and techniques, it is necessary to give an overview, to summarize the state-of-the-art and to review commercial sensors.

1.1 Overview

This thesis is structured in five chapters followed by an appendix. The first chapter gives an introduction on the topic with a review of thermal flow sensor principles. Additionally, commercial flow sensors are considered because they are widely used and have been established over the centuries. The second chapter describes briefly the relevant theoretical fundamentals of fluid mechanics and heat transfer from the branch thermodynamics. The third chapter deals with design and fabrication of the sensor. Hence, a simplified yet accurate enough analytical sensor model has been developed to estimate the characteristics to be expected. With these results, simulations with parameter sweeps are set up to find an optimum design. Different production technologies are analyzed and several designs are fabricated. The fourth chapter describes the experiments and depicts the results to optimize the simulations, the sensor design, and to characterize the sensor. Then, the sensor is tested in a real HVAC system to prove the concept feasible. The final chapter includes a discussion, a conclusion and an outlook.

1.2 Objective of the Thesis

There is a severe lack of thermal flow sensors for measuring flow velocities in existing HVAC systems which are accurate enough, easy to install and suitable for mass production. It is the aim of this thesis to design a flow sensor merely based on PCB technology as well as to fabricate and characterize a demonstrator to see if it is suitable for the use in HVAC systems.

The idea is to start with a simple model for testing the targeted approach with the chosen technology. Therefore, the possibilities of the PCB technology are studied and the limits of the PCB manufacturer are evaluated. Based on these results a FEM simulation is set up to develop a suitable design. The measurement range of the sensor should be $0 - 8\,\mathrm{m/s}$ to measure the emerging flow velocities in existing, old service buildings.

After finding a proper design, a PCB sensor is manufactured. Several parameters are varied to characterize the sensor. With these results the simulation is further optimized and repeated until a promising sensor design is found. For readout purposes analog front-end electronics are developed where a micro controller may be added later for easier digitalization and integration in a sensor network.

Last but not least, experiments in an experimental HVAC environment are carried out to test the sensor. Furthermore, experiments in a real HVAC system with several sensor nodes are carried out if time allows.

1.3 State-of-the-Art

Global warming, climate change and their resulting problems are a product of man's lavish use of fossil fuels. There is an urgent need to cut the fossil fuel consumption over the next few years. Statistics show that by 2012 in Europe energy consumption has reached 1080 Mtoe (Mega Tons of Oil Equivalent), broken down in percentages: 44% oil, 23.9% gas, 20.2% electricity, 4.8% solid fuels, 4.2% renewables and 2.8% derived heat [1]. In the USA approximately 50% of the total energy is consumed by residential and commercial sectors [2]. In Europe, this amount is 40-45% according to EUR-Lex [3] and EEA [4]. In buildings, more than one third of the energy is consumed by so-called heating, ventilating, and air conditioning (HVAC) systems. Two thirds of this amount are imputable to private living space and one third is attributed to service buildings [5, 6]. Reducing this energy consumption would help in achieving the required reduction and its importance is reflected in the "Building Research Establishment Environmental Assessment Method" [7], the "High Environmental Quality" [8], the "Leadership in Energy and Environmental Design" [9], or the "Comprehensive Assessment System for Built Environment Efficiency" [10].

Therefore, expensive research and improvements have been made in the building sector [11–14] and especially in the HVAC sector [15–17] in the last years. In the private sector, significant improvements have been made to reduce the overall energy consumption and optimize the energy demand of existing buildings. On the other hand, there are concerns about the absence of such an adequate progress in the service sector. To improve the status installation of a sufficiently large number of sensors is required to obtain a detailed picture of the actual state of a HVAC systems [18, 19]. Hence, sensing numerous parameters is a precondition for optimized building automation and to enable environmental monitoring. What are these required parameters? They are mainly temperature, humidity, air flow velocity, flow

direction, but also pressure, density, CO_2-concentration, and concentration of other pollution describing the air quality of a room. Placing various sensors to measure all parameters in each room is neither energy efficient nor necessary. Simply measuring the volume flow rate ($\dot{V}$) at strategic points will reveal inefficiency and saving potentials. For flat, plane cross-sections the volume flow rate can be expressed as

$$\dot{V} = \bar{v}_\mathrm{a} A \quad , \tag{1.1}$$

where $\bar{v}_\mathrm{a}$ is the mean flow velocity in a pipe (flow channel), and A is the cross-sectional area of the pipe. Equation 1.1 represents a simplified case of the continuity equation (Eq. 2.7) and is deduced in Sec. 2.1. Basically, for more complex cross-sections Eq. 1.1 turns into a surface integral (Eq. 2.6). However, the cross-sectional area of the pipes is fixed through the installation of the HAVC system and it is known due to the installation plan. Therefore, it is only necessary to measure the mean flow velocity but this velocity is usually not constant over the cross-section [20] which can be expressed as:

$$\bar{v}_\mathrm{a} = \frac{1}{A} \int_A \vec{v}_{(\mathrm{y,z})} \, \mathrm{d}A \quad , \tag{1.2}$$

where $\vec{v}_{(\mathrm{y,z})}$ is the velocity vector at a flow in x-direction. This leads to the research question: How can this mean flow velocity be measured?

Flowmeters

So-called flowmeters are one possible answer. They typically measure quantities of fluids such as mean velocity, volume flow rate or mass flow rate in pipes or open channels. There are a lot of different types of flowmeters [21]: the oldest includes different pressure, turbine, and positive displacement meters. The flow can also be measured with Coriolis, vortex, ultrasonic, magnetic, or thermal flowmeters. Relatively new groups are flowmeters based on optical or sonar technologies.

Different pressure sensors correlate flow with the difference in pressure upstream and downstream from a constriction in the flow. This constriction is created by orifice plates, flow nozzles, pitot tubes, wedge elements or venturi tubes. Therefore, there are a lot of possibilities to realize such a different pressure sensor [22–24].

Turbine flowmeters have a spinning rotor which is mounted on bearings in a housing. The rotor has propeller wings and it spins as the fluid passes through it. The rotational speed of the rotor is proportional to the flow velocity. The turbine flowmeters are classified according to the design of their spinning rotor [25, 26].

The basic principle of positive displacement flowmeters is counting how often a known reservoir is filled and emptied in a defined period of time. There are several types of positive displacement flowmeters depending on the way they trap the fluid into reservoirs of different shape [27, 28].

In Coriolis flowmeters the fluid passes through one or more vibrating bent tubes. The Coriolis force results from the acceleration caused by the mass moving toward or away from a center of rotation and is proportional to the mass flow rate [29, 30].

Vortex flowmeters are based on the von Karman[1] principle, where a fluid passes by a bluff body and generates vortices with a frequency that is proportional to the flow velocity [31–33].

Ultrasonic flowmeters can be classified in two main types: transit time and Doppler[2] ultrasonic flowmeters. The first one determines the time difference of a signal passing the pipe in and against the direction of the flow. This time difference is proportional to the flowrate [34–36]. The other ultrasonic flowmeters utilize the Doppler effect where the frequency shifts proportional to the mean velocity of the fluid [37, 38].

With Faraday's[3] Law of Electromagnetic Induction magnetic flowmeters (magneto-hydrodynamic generators) measure the flowrate of a conductive medium. Wire coils that generate a magnetic field in a pipe section are mounted on the pipe. A voltage is generated when the conductive fluid passes through this magnetic field because charges are separated by the Lorentz force. Electrodes detect this voltage and a faster flowing fluid results in a higher voltage [39, 40].

For sonar flowmeters two measurement methods are utilized to calculate the volume flow rate. They measure either the velocity of naturally occurring turbulent eddies or the speed at which sound waves propagate through the fluid [41, 42].

Optical flowmeters measure the speed of particles in the fluid via optical laser technology. When a laser illuminates an area, a quantity of photons will be scattered by the particles in the fluid depending on their speed [43, 44].

Thermal flowmeters heat the flow and use its thermal properties to measure the velocity. The different methods are described later in detail (Sec. 1.3).

HVAC Systems

Choosing a suitable measurement method is a critical step and several factors have to be considered. Target application and occurring velocities are main aspects. So, an investigation of existing HVAC systems is mandatory.

According to literature and industrial application HVAC systems can be divided into air-systems and air-water-systems. Heating and cooling rooms with air is sub-classified into low- and high-velocity systems. Moreover, systems are distinguished in single channel systems with constant or variable volume flow rate and in double channel systems with constant or variable volume flow rate. The air flow velocities in ventilation ducts are limited to avoid noise generation and high pressure drop.

---

[1] Theodore von Karman, Hungarian-American mathematician, aerospace engineer and physicist, 1881 - 1963

[2] Christian Andreas Doppler, Austrian mathematician and physicist, 1803 - 1853

[3] Michael Faraday, English scientist, 1791 - 1867

Duct type	Mean velocity range	
	Public buildings m/s	**Industrial plant m/s**
Air intake from outside	2.5 - 4.5	5.0 - 6.0
Heater connection to fan	3.5 - 4.5	5.0 - 7.0
Main supply ducts	5.0 - 8.0	6.0 - 12.0
Branch supply ducts	2.5 - 3.0	4.5 - 9.0
Supply registers and grilles	1.2 - 2.3	1.5 - 2.5
Low level supply registers	0.8 - 1.2	
Main extract ducts	4.5 - 8.0	6.0 - 12.0
Branch extract ducts	2.5 - 3.0	4.5 - 9.0

Table 1.1: Mean velocity ranges of the various ducts used in public buildings and industrial plants [45].

In industrial plants there is a significantly higher background noise than in public buildings. Therefore, more duct-generated noise (caused by higher flow velocities) must be accepted. Table 1.1 lists the mean velocity ranges of different duct types in public buildings and industrial plants. The whole mean velocity range for public buildings comprises 0.8 up to 8 m/s and for industrial ones 1.5 up to 12 m/s. However, high velocities are only reached in high pressure ducts which are not common anymore. So, if the sensor is capable of measuring up to 8 m/s all public HAVC systems are covered.

When it is not required to achieve the highest sensing accuracy, but to get robust, flexible in design and in layout, and cost-effective sensors, manufacturing technologies are needed which are suited for mass production based on polymers. Moreover, the fabrication should only require few and inexpensive process steps to keep the total costs of the system affordable.

Printed circuit board (PCB) technology is suitable for high-volume production used in the consumer electronics market and is also applied for sophisticated devices in the medical, aerospace, and industrial area. Therefore, it is not surprising that this technology has become interesting for the production of various senor types. Often, PCB is the platform where the sensor is integrated. Cruz et al. [46] presented a pressure sensing platform for health monitoring or Prijic et al. [47] integrated a thermal energy harvesting wireless sensor node in an aluminum core PCB. Nojdelov et al. [48] introduced a capacitive sensor interface based on the charge balancing method. A fully integrated microfluidic measurement system was developed by Lötters et al. [49]. They used this system to determine gas and liquid mixtures

compositions in real time. There are also publications where the PCB itself is utilized as a sensor, like Ngyuen et al. [50], where the PCB acted as fluidic capacitive sensor for detection of air bubbles inside engine lubricant. The three-electrode sensor structure is designed and simulated for monitoring and estimating the amount and size of the air bubbles. Petervari et al. [51] built highly sensible pressure sensors embedded in a cuneiform probe. When air streams over the probe the sensors measure inflow disturbances. Arpaia et al. [52] investigated the metrological performance of a magnetic field transducer. The transducer consisted of a fiberglass cylinder hosting three PCB coils with a diameter of 7.5 mm. A capacitive microsensor for tilt measurement was designed and fabricated by Baby et al. [53]. Two electrode configurations are etched on a double sided PCB and convert the movement of a membrane into a change in capacitance.

Printed Circuit Board

Each PCB is custom-designed and its design has a strong effect on the mechanical and electrical performance. The material properties are given by the determinded type of board, the way it is laminated and its interconnections between the conductive layers. The board layers consist of a conductive laminate material and an insulating dielectric substrate. The conductive material is commonly a copper foil. It is adhesively bonded onto the substrate by applying heat and pressure. The most common substrates are phenolic paper (synthetic resin bonded paper) and glass reinforced epoxy (FR4) [54]. The fabrication of a flow sensor with these PCB technologies fits the requirements of a thermal micromachined flow sensor, such as: sufficiently large temperature coefficient of the active material and thermally insulating substrate.

Thermal Flow Sensor Principles

This section will give a brief review on thermal flow sensors. The basic principles have been well established for several years and sensational advances have not been made in recent years nor are any expected in the near future. Nevertheless, a great deal of work has been done in science to provide adequate solutions for modern measurement problems. These problems deal with improving requirements for flow measurement like accuracy, reliability, interchangeability, costs, and safety [55].

Thermal flow sensors measure flow velocity based on the effect of forced convection. The correlation to thermal variables such as temperature and heating power can be used to evaluate the flow velocity. The sensors are categorized by their thermoelectrical conversion in:

* thermoresistive
* thermocapacitive
* thermoelectric
* thermoelectronic

* pyroelectric
* frequency analog sensors

Thermoresistive Sensors

They are based on the relation between the electrical resistance R and temperature T:

$$R(T) = R_0[1 + \alpha_{\mathrm{TCR1}}(T - T_0) + \alpha_{\mathrm{TCR2}}(T - T_0)^2 + ... \\ ... + \alpha_{\mathrm{TCRn}}(T - T_0)^n + ...] \quad , \tag{1.3}$$

where R_0 is the resistance at temperature T_0 and α_{TCR1} to α_{TCRn} are the corresponding temperature coefficients of resistance (TCR). Here, TCR specifies the relative change of resistance per unit change of the temperature and thus determines the sensitivity. In the respective linear range of thermoresistive sensors, Eq. 1.3 reduces to:

$$R(T) = R_0\,[1 + \alpha_{\mathrm{TCR}}(T - T_0)] \quad , \tag{1.4}$$

where α_{TCR} denotes the linear temperature coefficient of resistance (TCR). Transducers for thermoresistive sensors can be fabricated from different materials such as single- or polycrystalline silicon, metals, or metal alloys. There are three different types of thermoresistive principles: Hot-film (or hot-wire), Calorimetric, and Time-of-Flight (Fig. 1.1).

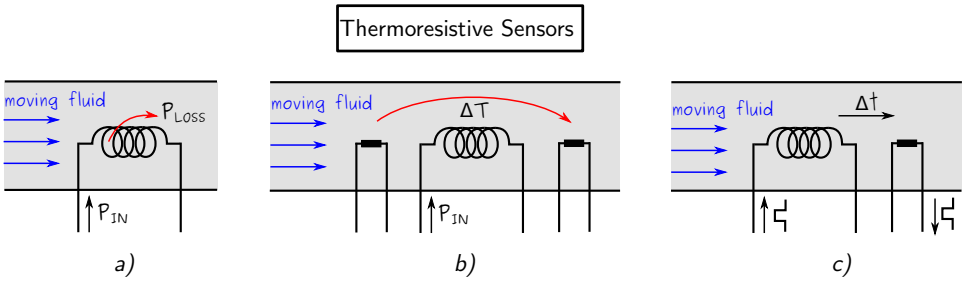

Figure 1.1: Sketch of the three thermoresistive principles. a) hot-film (hot-wire) anemometer determines the fluid velocity by the power loss at the heat; b) calorimetric anemometer measures the fluid velocity via the temperature difference between sensors placed up- and downstream around the heater; c) time-of-flight sensor utilizes the time difference of a heating pulse to determine the fluid velocity.

A **hot-film or hot-wire** anemometer is one of the most well known thermal anemometer which measures the fluid velocity by noting the heating power convected away by a fluid. The only difference between hot-film and hot-wire is the form of substrate which is used for the heater, either a thin film or a wire. The principles of the anemometer is to heat the film (wire) with a constant current (CCA - constant current anemometer) or maintain at a constant temperature (CTA - constant temperature anemometer). By monitoring the change of the film (wire)

temperature under the constant current or the current required to maintain a constant film (wire) temperature, the heat loss can be obtained. In both cases, the heating power lost to the fluid is a function of the fluid velocity according to the convective theory. Ivanov et al. [56] used such a hot-film flow sensor to evaluate lamination with elastomer bags. The sensor is integrated onto the inner surface of a tube segment and consists of six sectors of meander-formed conductive traces (200 µm both width and pitch) evenly distributed on the circumference of the tube.

Xu et al. [57] analyzed the measurement accuracy of a hot film air flow sensor on basis of SiN_x influenced by moisture. With measurement results simulations are carried out and the sensor behavior is predicted.

Calorimetric anemometers use a heating element in combination with one or more sensing elements to measure the fluid velocity. As with Hot-Film the heater can be supplied with a constant current or the sensing elements can be maintained at a constant temperature. These additional sensing elements are usually placed up- and downstream from the heater, which also allows the measurement of the flow direction. Through the heater a thermal profile occurs around all sensing elements symmetrically as long as the fluid is not flowing. When the velocity starts to increase the thermal profile shifts downwards and a temperature difference - corresponding to a resistance difference - arises at the sensing elements. This difference in the resistance is a function of the fluid velocity. Xu et al. [58] presented a low-cost temperature-compensated thermoresistive micro calorimetric flow sensor. A commercial 0.35 µm CMOS MEMS technology was used. The sensor achieved a normalized sensitivity of 230 mV/(m/s)/mW with a bidirectional flow detection of nitrogen. The design and characterization of a novel thermal-calorimetric flow-meter using suspended-cantilever-structure was investigated by Valizadeh et al. [59]. The proposed flow meter can minimize thermal loss through conduction, and provide a thin velocity boundary layer in order to enhance the sensitivity and power efficiency of gas flow meters.

Time-of-Flight sensors measure the fluid velocity via defined heating pulses generated at the heater. These pulses travel through the fluid and are measured by one or more sensing elements. At the sensing elements, the measured pulse arrives damped and time delayed. However, as long as the sensor can recognize an incoming pulse (damping small enough), the time difference can be used to determine the fluid velocity.

Thermocapacitive Sensors

A thermocapacitive flow sensor works similar to a thermoresistive one. In contrast to the thermoresistive principle, the temperature dependence of the dielectric constant of a material, instead of the temperature coefficient of resistance, allows the realization of a thermal flow sensor. There is a heater as well as a nearby capacitor. When the heater is powered, it causes the temperature of the capacitor to rise. The dielectric constant of the capacitor increases with temperature, result-

ing in an increase in the capacitance. When the fluid flows through the capacitor, the temperature of the capacitor will decrease due to the convective heat transfer from the capacitor to the fluid. Thus the capacitance will also be reduced. By measuring the capacitive value, the flow velocity can be obtained by a calibration relationship between the flow rate and the capacitance. Kerpel et al. [60] used such capacitive sensors to study two-phase flow frictional pressure drop of a refrigerant flow of a sharp return bend. To be able to explain the effect of the pressure drop, the flow behavior was measured at several locations up- and downstream of the return bend. From this capacitive signal, the void fraction and wavelet variance were derived. Rivadeneyra et al. [61] presented a printed capacitive-resistive double sensor for toluene and moisture measurement. The sensor was manufactured with inkjet printing to define the electrodes and screen printing to deposit the sensitive material.

Thermoelectric Sensors

With the thermoelectric effect, or Seebeck[4] effect, temperature differences can also be measured. Thermoelectric sensors yield a potential difference between two connected metals or semiconductors. Inside a metal or semiconductor not all electrons are bound to specific atoms. The number of these free electrons (electron gas) differs from material to material and when such two materials are connected, their electron gas diffuse into each other. Due to the different densities of the electron gas electrically charge regions occurs. This charge changes with the temperature because the number of free electrons increase with higher temperature. The resulting voltage is defined as:

$$U_{\mathrm{TES}}(T) = \alpha_{\mathrm{s}} \triangle T \quad , \tag{1.5}$$

where $U_{\mathrm{TES}}(T)$ is the emerging voltage, α_{s} the thermoelectric coefficient, or Seebeck coefficient, and $\triangle T$ the temperature difference. The formula shows that electricity is produced directly from heat. For a given thermoelectric circuit operating in a given temperature range, the extent of the voltage depends mainly on the temperature difference between the two ends. Nagai et al. [62] used this effect to build a micro-thermoelectric gas sensor. A catalyst was integrated and the effect of the catalyst thickness and the CH_4 detection performance was evaluated for detection sensitivity to low concentrations of methane. Nevertheless, the thermoelectric effect is not always useful for one pair of materials. Therefore, many couples are connected in series to form a thermopile which multiplies the thermoelectric voltage by the number of thermocouples. Thermopiles are used for measuring heater temperature in hot-film mode. Alternatively, to measure the temperature difference between downstream and upstream, at least two thermopiles are needed. Steiner et al. [63] presented a technology feasibility study to implement flow sensors based on Ag-Ni thick-film thermopiles printed by silk screen printing on a plastic carrier film.

[4] Thomas Johann Seebeck, German physicist, 1770 – 1831

Thermoelectronic Sensors

Thermoelectronic flow sensors use the temperature dependence of pn-junctions in diodes or bipolar transistors to measure the flow [64]. The voltage drop over the forward biased base-emitter junction follows the relation [65]:

$$U_{\mathrm{BE}} = V_{\mathrm{G}} + \frac{KT}{e} \cdot \ln\left(\frac{I_{\mathrm{C}}}{I_{\mathrm{R}}}\right) \quad , \tag{1.6}$$

where V_{G} is the material's band gap, K is the Boltzmann constant, e is the elementary charge, I_{C} the collector current, I_{R} the reference current, and T the temperature. Thermoelectronic sensors can also be realized in ceramic substrates [66].

Pyroelectric Sensors

Pyroelectric sensors are based on the dependence of surface charge of a pyroelectric material on the change of the supplied heat. Hsiao et al [67] proposed a methodology for designing a multi-frequency band pyroelectric sensor. Frequency analog sensors are based on thermal excitation and evaluation of oscillating frequency. The sensing concept is based on the temperature dependence of the oscillating behavior of mechanical elements such as cantilevers and membranes. The change of temperature causes a change of mechanical stress in the element, which leads to a change of its resonant frequency. Kielbasa et al [68] used a vibrating hot wire to measure gas flow velocity.

Chapter 2

Theoretical Fundamentals

This chapter presents theoretical basics to provide fundamentals for the subsequent sections. Two topics of physics are needed: fluid mechanics and heat transfer. The first one delivers the interesting parameter mean flow velocity ($\bar{v}_\mathrm{a}$) and the relations for flow simulations of a sensor within a fluid. The other one provides convection laws for electrical into thermal energy in an environment of solids and fluids. This allows for developing models for heat transfer and thermal sensors.

2.1 Fluid Mechanics

Fluid mechanics of liquids (hydrodynamics) and gases (aerodynamics) describe the motion of fluid particles (aggregates of the fluid) in mesoscopic time and space scales. Nearby fluid particles exchange molecules and this process can change their quantities like density, impulse, internal or kinetic energy. Furthermore, important spatial characteristics of a fluid are its divergence

$$Q_\mathrm{fluid}(\vec{r},t) = \vec{\nabla}\cdot\vec{v} = \operatorname{div}\vec{v} \tag{2.1}$$

and its curl

$$\vec{\Gamma}_\mathrm{fluid}(\vec{r},t) = \vec{\nabla}\times\vec{v} = \operatorname{rot}\vec{v} \quad , \tag{2.2}$$

with $\vec{r}$ as the position vector of the fluid particles, t the time, and $\vec{v}$ the velocity of the fluid particles. The divergence (generation rate) defines either fluid particles flow out from a point (source) or in it (sink). The curl (vorticity) indicates how much the fluid spins at point $\vec{r}$ in a velocity field.

There are two descriptions [69] for the temporal change of a velocity field. The first one, the Lagrange[1] formulation, regards the acceleration of a fluid particle in a moving reference system (with the particle). Laws of conservation are described by this formulation. In the Euler[2] formulation the acceleration of a local flow field is regarded in a fixed reference system. As a consequence, different fluid particles at

[1] Joseph-Louis Lagrange, Italian mathematician and astronomer, 1736 - 1813

[2] Leonhard Euler, Swiss mathematician and physicist, 1707 - 1783

different times contribute to the local flow field at point $\vec{r}$. Equation 2.3 shows the relation between the Lagrange and the Euler formulation:

$$\frac{\mathrm{d}}{\mathrm{d}t} = \frac{\partial}{\partial t} + (\vec{v} \cdot \vec{\nabla}) \quad . \tag{2.3}$$

Based on these formulations, fluids can be classified either in ideal (Euler) or in real (Newton[3]) fluids. In ideal fluids is the motion of the fluid-particles always isentropic which implies no heat generation and no heat transport. Hence, inner forces are only pressure gradients because fluid-particles are at rest in relation to each other and do have the same temperature. Whereas, the specification of real fluids defines a change of the entropy as consequence of a molecular exchange which comes from inner friction and heat transport.

Continuity Equation

The mass flow density $\vec{j}$ describes the mass transportation phenomena of flow depended fluid particles:

$$\vec{j} = \varrho \vec{v} \quad , \tag{2.4}$$

where ϱ is the density of the fluid. Deduced from $\vec{j}$, the mass flow rate $\dot{m}$ states how much mass is passing through an area A per unit of time and it can be expressed as

$$\dot{m} = \frac{\partial m}{\partial t} = \iint_A \vec{j} \, \mathrm{d}\vec{A} \quad , \tag{2.5}$$

where m is the mass of the passing fluid. While, the volume flow rate $\dot{V}$ states how much fluid volume is passing through an area A per unit of time and it can be expressed as

$$\dot{V} = \frac{\partial V}{\partial t} = \iint_A \vec{v} \, \mathrm{d}\vec{A} \quad , \tag{2.6}$$

where V is the volume of the passing fluid. In a volume element δV mass can't be generated or destroyed because of the law of conservation of mass. Only when fluid particles flow in or out of δV, the mass changes over time. Consequently, the divergence of the mass flow density describes the in- and outflow of mass from δV. With $\delta V \to 0$ yields the continuity equation for compressible fluids:

$$\frac{\partial \varrho}{\partial t} = -\vec{\nabla} \cdot (\varrho \vec{v}) = -\mathrm{div}\,(\varrho \vec{v}) \quad . \tag{2.7}$$

In incompressible fluids the density is spatially and temporally constant. This reduces Eq. 2.7 to a pure kinematic condition (solenoidality of the flow field) expressed as

$$\nabla \cdot \vec{v} = \mathrm{div}\, \vec{v} = 0 \to \oint_A \vec{v} \, \mathrm{d}\vec{A} = 0 \quad . \tag{2.8}$$

[3] Sir Isaac Newton, English physicist and mathematician, 1643 - 1727

Hence, Eq. 2.8 implies the law of conservation of volume where no fluid arises or dries up at any point in the observed volume. Therefore, the law of conservation of volume for a pipe can be expressed as

$$\dot{V} = \bar{v}_1 A_1 = \bar{v}_2 A_2 \quad , \tag{2.9}$$

where $\bar{v}_{1,2}$ are the mean flow velocities and $A_{1,2}$ are the pipe cross-sections.

Ideal Frictionless Fluids (Euler Fluids)

An important term in fluid mechanics is the entropy which is defined by Boltzmann as the amount of freedom of arrangement [70]. The entropy can be expressed as

$$S = m_\mathrm{T} s(\vec{r}, t; T) \quad , \tag{2.10}$$

with m_T as the mass of a fluid particle, and s as the specific entropy. The index T refers to the temperature, $\vec{r}$ to the position vector, and t to the time. In ideal fluids the movement of a particle is defined to be always adiabatic. Adiabatic means that the movement occurs without loss of heat in an enclosed system. Therefore, the entropy doesn't change over time leading to the constancy of the entropy:

$$\frac{\mathrm{d}s}{\mathrm{d}t} = \frac{\partial s}{\partial t} + \vec{v}(\vec{\nabla} s) = 0 \quad . \tag{2.11}$$

Both the continuity equation (Eq. 2.7) and the constancy of the entropy (Eq. 2.11) form the thermodynamic equations of the Euler theory.

When there are only outer- and pressure forces the movement of fluid particles can be calculated through Newton's equation of motion (ideal):

$$\frac{\mathrm{d}(m_\mathrm{T}\vec{v})}{\mathrm{d}t} = \vec{F} = \vec{F}_\mathrm{o} + \vec{F}_\mathrm{p} \quad , \tag{2.12}$$

where $\vec{F}_o$ is the outer force, and $\vec{F}_\mathrm{p}$ is the pressure force. The force $\vec{F}$ can also be written as gradient of potentials because there are no friction forces. The specific enthalpy $h(s, p)$ of a fluid particle with the mass m_T contains the entropy and the pressure p and it can be expressed as

$$\mathrm{d}h = T\,\mathrm{d}s + \frac{\mathrm{d}p}{\varrho} \quad . \tag{2.13}$$

For an isentropic flow ($ds = 0$) the pressure force on the fluid particle is $\vec{F}_\mathrm{p} = -m_\mathrm{T}\,\mathrm{grad}\,h = -V_\mathrm{T}\,\mathrm{grad}\,p$. With convective derivation Eq. 2.12 can be transformed from the Lagrange description into the Euler description. The result is the general Euler equation for ideal fluids which can be expressed as

$$\frac{\partial \vec{v}}{\partial t} + (\vec{v} \cdot \vec{\nabla})\,\vec{v} = \vec{f} - \frac{\vec{\nabla} p}{\varrho} \quad , \tag{2.14}$$

where $\vec{f}$ is the outer acceleration. In conclusion, Newton's equation of motion without friction forces (Eq. 2.12) turns into the general Euler equation for ideal fluids (Eq. 2.14). It describes the degrees of freedom of the velocity $\upsilon_{\mathrm{x,y,z}}$. Further, an ideal fluid can't pass solid walls which leads to the boundary condition for a Euler fluid:

$$\vec{v}\,(\vec{r} \in A, t) \cdot \vec{n} = 0 \quad . \tag{2.15}$$

This condition must apply for every point $\vec{r}$ in a solid wall with the surface A with $\vec{n}$ as the normal vector to the wall $\vec{r}$.

Real Fluids (Newton Fluids)

Extending Newton's equation of motion for ideal fluids (Eq. 2.12) with the friction force $\vec{F}_{\mathrm{R}}$, Newton's equation of motion for real fluids is derivated:

$$\frac{\mathrm{d}(m_{\mathrm{T}}\vec{v})}{\mathrm{d}t} = \vec{F} = \vec{F}_{\mathrm{o}} + \vec{F}_{\mathrm{p}} + \vec{F}_{\mathrm{R}} \quad . \tag{2.16}$$

This friction force $\vec{F}_{\mathrm{R}}$ occurs in form of shear stress when two fluid particles are moving with a small velocity to each other (relative velocity). Hence, for compressible Newton fluids with a constant viscosity coefficient, Newton's equation of motion turns via convective derivation into the Navier-Stokes equation for compressible fluids[45]:

$$\varrho\,\frac{\mathrm{d}\vec{v}}{\mathrm{d}t} = \varrho\vec{f} - \vec{\nabla}p + \eta\triangle\vec{v} + \left(\varsigma + \frac{\eta}{3}\right)\vec{\nabla}\left(\vec{\nabla}\cdot\vec{v}\right) \quad , \tag{2.17}$$

where η is the dynamic viscosity and ς the volume viscosity. In general, viscosity can be seen as the thinness or thickness of a fluid. The dynamic viscosity, which is sometimes referred to as absolute viscosity, is the quantitative expression of a fluid's resistance to flow. Whereas, the volume viscosity, which is sometimes called the diffusivity of momentum, is a ratio of the viscous force to the inertial force. In Tab. 2.1 dynamic and kinematic viscosities of some fluids are presented.

For incompressible Newton fluids ($\vec{\nabla}\cdot\vec{v} = 0$) and with the kinematic viscosity ($\nu = \eta/\varrho$), Eq. 2.17 turns into the Navier-Stokes equation for incompressible fluids:

$$\frac{\partial\vec{v}}{\partial t} + (\vec{v}\cdot\vec{\nabla})\,\vec{v} = \vec{f} - \frac{\vec{\nabla}p}{\varrho} + \nu\triangle\vec{v} \quad . \tag{2.18}$$

Basically, the Navier-Stokes equation describes the degrees of freedom of the velocity $\upsilon_{\mathrm{x,y,z}}$. In detail, $\partial\vec{v}/\partial t$ describes the local acceleration, $(\vec{v}\cdot\vec{\nabla})\vec{v}$ the convective acceleration, $\vec{f}$ the outer acceleration, $\vec{\nabla}p/\varrho$ the pressure acceleration, and $\nu\triangle\vec{v}$ the viscose acceleration. The boundary condition for the Navier-Stokes equation is the no-slip condition where fluid particles stick to the wall because of the molecular interaction (adhesion) which means for every point $\vec{r}$ at a solid wall with the area A

$$\vec{v}\,(\vec{r} \in A, t) = 0 \quad . \tag{2.19}$$

[4] Claude-Louis M. H. Navier, french engineer and physicist, 1785 - 1836

[5] Sir George Gabriel Stokes, 1st Baronet, Irish mathematician, physicist, politician and theologian, 1819 - 1903

Fluid	**Temperature** (T)	**Dynamic viscosity** (η)	**Kinematic viscosity** (ν)
	°C	$\mathrm{Pa \cdot s}$	$\mathrm{m^2/s}$
Water	20	$1.0 \cdot 10^{-3}$	$1.0 \cdot 10^{-6}$
	100	$0.3 \cdot 10^{-3}$	$0.3 \cdot 10^{-6}$
Air	20	$1.8 \cdot 10^{-5}$	$15 \cdot 10^{-6}$
	100	$2.2 \cdot 10^{-5}$	$23 \cdot 10^{-6}$
Steam	100	$1.2 \cdot 10^{-5}$	$21 \cdot 10^{-6}$
Ethanol	20	$1.2 \cdot 10^{-3}$	$1.5 \cdot 10^{-6}$

Table 2.1: Dynamic and kinematic viscosity of some fluids at different temperatures.

Reynold Number

From the solution of the Navier-Stokes equation (Eq. 2.18)

$$\vec{v}/u = \vec{\omega}\left(\vec{r}/L,\, Re\right) \quad , \tag{2.20}$$

where u is the characteristic flow velocity, L the characteristic length (e.g.: flow channel diameter or length of a floated plate), and $\vec{\omega}$ the energy density, follows Reynolds[6] law of similarity [71]: "*Flow fields whose boundaries are geometrically similar have similar flow fields under the same Reynolds number.*" The dimensionless Reynolds number Re is defined as inertia force divided by friction force expressed as

$$Re = \frac{uL}{\nu} = \frac{\varrho u L}{\eta} \quad . \tag{2.21}$$

With the Reynolds number it is possible to predict the state of a streaming fluid. Below a critical value Re_{crit} the flow is laminar and above it turbulent. However, the passage of these two states is fluent not abrupt which means a border zone occurs at Re_{crit} where each state may be possible depending on boundary conditions.

2.2 Heat Transfer

Heat transfer describes the regularities how heat is transported between systems of different temperatures [72, 73]. In modern literature heat transfer is classified in the three principles: heat conduction, heat convection, and thermal radiation or even four by splitting convection into free and forced convection [74–76]. However, Nußelt[7] posited in his basic law of heat transfer [77] that conduction and convection

[6] Osborne Reynolds, Irish physicist, 1842 - 1912

[7] Ernst Kraft Wilhelm Nußelt, German physicist, 1882 - 1957

are not separable:

"*Es wird vielfach in der Literatur behauptet, die Wärmeabgabe eines Körpers habe drei Ursachen: die Strahlung, die Wärmeleitung und die Konvektion. Diese Teilung der Wärmeabgabe in Leitung und Konvektion erweckt den Anschein, als hätte man es mit zwei unabhängigen Erscheinungen zu tun. Man muss daraus schließen, dass Wärme auch durch Konvektion ohne Mitwirkung der Leitung übertragen werden könnte. Dem ist aber nicht so.*"

Hence, heat transfer can only occur through heat conduction or thermal radiation (Fig. 2.1). Yet, for simpler evaluation heat conduction is split into conduction between solids and static fluids (Fig. 2.1a) and into conduction in moving fluids (Fig. 2.1b), called convection. Heat conduction occurs in solids or static fluids in terms of transferring oscillation energy of nearby molecules and transferring kinetic energy of conduction electrons. Heat energy flows from the region of higher temperature to the region of lower temperature as long as there exists a temperature gradient. In such a system heat transfer depends only on the temperature gradient and on several material parameters. At convection, heat transfer is a bit more complex because enthalpy is transported in the streaming fluid. Therefore, heat transfer depends additionally on a flow depended boundary layer. There are two types of convection. The first one, free convection, occurs without any influence from the outside while if the liquid is moved from outside forces (e.g.: pressure, fan, pump) then the second one, forced convection, appears. Thermal radiation is defined as electromagnetic radiation between two or more bodies and depends on several components. These include surface area and reflectivity, temperature, emissivity, and geometric orientation.

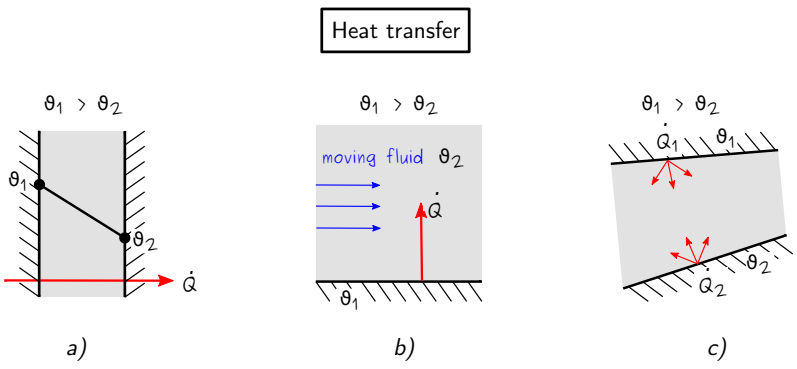

Figure 2.1: Heat transfer mechanisms: a) heat conduction in solids or static fluids; b) heat conduction from a surface into a moving fluid (convection); c) radiation between two surfaces. In these examples the temperature ϑ_1 is higher than ϑ_2. Therefore, the heat flow is form ϑ_1 to ϑ_2 and at radiation both surfaces emit a heat flow but the one from the surface with the temperature ϑ_1 is higher.

Heat Transfer Parameters

This section describes the most relevant quantities to describe the processes in heat transfer. The obvious quantities are heat and temperature which both are physical properties of a body. The heat E is the total energy in a body and often measured in Jules (J) while the temperature T in Kelvin (ϑ for Celsius[8] temperatures) gives an objective measure of hot or cold. A temperature increase is possible by transporting heat to a body. The related parameter of how much the temperature increases for different materials by the same transported heat is the specific heat capacity c_p. The heat flux $\dot{Q}$ states how much heat per unit of time is transferred and the heat flux density $\dot{q}$ describes how much heat per unit area is transferred. The heat transfer coefficient α_ht describes how much heat through an area and per unit of temperature difference is transferred. The property of a material that indicates its ability to conduct heat is summarized in the thermal conductivity λ. It defines how much heat per unit of length of the material and per degree temperature difference can be transferred.

Heat Conduction in Solids and Static Fluids

Heat conduction occurs when a temperature gradient arises in a material. The heat flux density $\dot{q}$ is defined by Fourier's Law[9] as

$$\dot{q} = -\lambda \nabla \vartheta = -\lambda \frac{\mathrm{d}\vartheta}{\mathrm{d}r} \quad . \tag{2.22}$$

The resulting heat flux $\dot{Q}$ when passing an area A is expressed as

$$\dot{Q} = \int_A \dot{q} \, \mathrm{d}A \quad . \tag{2.23}$$

When two bodies with different temperatures come into contact, their combined temperature field changes both temporally and locally which can be described with heat transfer differential equations. For derivation of the three-dimensional heat transfer differential equation a one-dimensional example is used as starting point. In this example there is a infinite long, plain plate which is in contact with a fluid. The heat transfer through the plate occurs only in x-direction because the lateral dimension is assumed as infinite. As a result of this assumption, Eq. 2.22 inserted in Eq. 2.23, turns into

$$\dot{Q}_\mathrm{x} = -\lambda A \frac{\mathrm{d}\vartheta}{\mathrm{d}x} \quad . \tag{2.24}$$

This partial differential equation represents the heat flux to a infinitesimal volume element. On the opposite position $(x + \mathrm{d}x)$ the heat flux can be expressed as

$$\dot{Q}_\mathrm{x+dx} = \dot{Q}_\mathrm{x} + \frac{\partial \dot{Q}_\mathrm{x}}{\partial x} \, \mathrm{d}x = -\lambda A \frac{\mathrm{d}\vartheta}{\mathrm{d}x} - \lambda A \frac{\mathrm{d}^2\vartheta}{\mathrm{d}x^2} \, \mathrm{d}x \quad . \tag{2.25}$$

[8] Anders Celsius, Swedish astronomer, physicist, and mathematician, 1701 - 1744

[9] Jean-Baptiste Joseph Fourier, French mathematician and physicist, 1768 - 1830

The change of the heat flux amounts then

$$\mathrm{d}\dot{Q}_{\mathrm{x}} = \dot{Q}_{\mathrm{x+dx}} - \dot{Q}_{\mathrm{x}} = -\lambda A \frac{\mathrm{d}^2\vartheta}{\mathrm{d}x^2}\,\mathrm{d}x \quad . \tag{2.26}$$

Because there is only heat transfer in x-direction, the chance of heat flux is equivalent to the temporal chance of the enthalpy (first law of thermodynamics - $\mathrm{d}p = 0$) of the material in the infinitesimal volume element

$$\delta\dot{Q}_{\mathrm{x}} = -\rho A\,\mathrm{d}x\,c_{\mathrm{p}}\frac{\partial\vartheta}{\partial t} \quad . \tag{2.27}$$

Combing Eq. 2.26 and Eq. 2.27 leads to a differential equation which represents the temporal and local temperature distribution in the plate

$$\frac{\partial\vartheta}{\partial t} = \frac{\lambda}{\rho c_{\mathrm{p}}} \cdot \frac{\mathrm{d}^2\vartheta}{\mathrm{d}x^2} \quad . \tag{2.28}$$

The expression $\lambda/(\rho c_{\mathrm{p}})$ is called thermal diffusivity a and represents a material constant, its analogous to the diffusion. It describes the temporal chance of the spatial temperature distribution. Unlike the heat conductivity, the thermal diffusivity describes transient effects rather then steady behavior of the heat transfer. Inserting the thermal diffusivity into Eq. 2.28 and expanding it into the three-dimensional space, it turns into the general three-dimensional differential equation for transient heat transfer:

$$\frac{\partial\vartheta}{\partial t} = a\frac{\mathrm{d}^2\vartheta}{\mathrm{d}r^2} = a\nabla^2\vartheta \quad . \tag{2.29}$$

Forced Convection

At forced convection heat transfer occurs via both a temperature difference and a flow. This flow is forced by an outer pressure difference caused by fans or pumps. The transport processes are described by differential equations. In particular, five unknowns (e.g., three velocity components, pressure, and temperature) from five different equations have to be calculated. One of these equations is the Continuity Equation for incompressible fluids (Eq. 2.8). Another on is Newton's equation of motion for real fluids (Eq. 2.16) from which the Reynolds number (Sec. 2.1) can be deduced for resolving velocity, viscosity, and a characteristic length. However, there are additional quantities for the description of heat transfer like thermal conductivity and heat flux density. Besides the Reynolds number there are two other interesting parameters of convection: The Prandtl number[10] and the Nusselt number.

The first one is deduced from the general three-dimensional differential equation (Eq. 2.29). The left side of this equation has to be extended by the temporal change caused by the enthalpy flow (for a streaming fluid). Therefore, the partial differential is replaced with the total differential of the temperature

$$\frac{\partial\vartheta}{\partial t} \Rightarrow \frac{\partial\vartheta}{\partial t} + \frac{\partial\vartheta}{\partial x}\cdot\frac{\mathrm{d}x}{\mathrm{d}t} + \frac{\partial\vartheta}{\partial y}\cdot\frac{\mathrm{d}y}{\mathrm{d}t} + \frac{\partial\vartheta}{\partial z}\cdot\frac{\mathrm{d}z}{\mathrm{d}t} \quad , \tag{2.30}$$

[10] Ludwig Prandtl, German engineer, 1875 - 1953

and with $\mathrm{d}x/\mathrm{d}t = c_\mathrm{x}$, $\mathrm{d}y/\mathrm{d}t = c_\mathrm{y}$ and $\mathrm{d}z/\mathrm{d}t = c_\mathrm{z}$, Eq. 2.29 turns into

$$\frac{\partial \vartheta}{\partial t} + \frac{\partial \vartheta}{\partial x}c_\mathrm{x} + \frac{\partial \vartheta}{\partial y}c_\mathrm{y} + \frac{\partial \vartheta}{\partial z}c_\mathrm{z} = a\left(\frac{\mathrm{d}^2\vartheta}{\mathrm{d}x^2} + \frac{\mathrm{d}^2\vartheta}{\mathrm{d}y^2} + \frac{\mathrm{d}^2\vartheta}{\mathrm{d}z^2}\right) \quad . \tag{2.31}$$

This equation can by switched into a non-dimensional notation by correlating the parameters to a characteristic dimension:

* Characteristic length L: $x = x^* L$
* Characteristic velocity u: $c_\mathrm{x,y,z} = c^*_\mathrm{x,y,z} u$
* Characteristic pressure $\rho \cdot u^2$: $p = p\rho u^2$
* Characteristic temperature $(\vartheta_\mathrm{F} - \vartheta_\mathrm{W})$: $\vartheta = \vartheta^*(\vartheta_\mathrm{F} - \vartheta_\mathrm{W}) + \vartheta_\mathrm{F}$
* Characteristic time L/u: $t = t^* L/u$

Now, the non-dimensional parameters are inserted into Eq. 2.31 and, via transforming, the non-dimensional notation of the temperature field equation can be expressed as

$$\frac{\partial \vartheta^*}{\partial t^*} + \frac{\partial \vartheta^*}{\partial x^*}c^*_\mathrm{x} + \frac{\partial \vartheta^*}{\partial y^*}c^*_\mathrm{y} + \frac{\partial \vartheta^*}{\partial z^*}c^*_\mathrm{z} = \frac{a}{uL}\left(\frac{\mathrm{d}^2\vartheta^*}{\mathrm{d}x^{*2}} + \frac{\mathrm{d}^2\vartheta^*}{\mathrm{d}y^{*2}} + \frac{\mathrm{d}^2\vartheta^*}{\mathrm{d}z^{*2}}\right) \quad . \tag{2.32}$$

The prefactor of the right side (a/uL) can be rewritten and, finally, the Prandtl number can be found besides the Reynolds number:

$$\frac{a}{uL} = \frac{\nu}{uL} \cdot \frac{a}{\nu} = \frac{1}{Re} \cdot \frac{1}{Pr} \Rightarrow Pr = \frac{\nu}{a} = \frac{\nu \rho c_\mathrm{p}}{\lambda} \quad . \tag{2.33}$$

The Prandtl number is temperature-dependent and defined as the ratio of momentum diffusivity to thermal diffusivity [78].

The Nusselt number is deduced from the heat flux density by using an example. A fluid with the temperature ϑ_F flows in a flow channel with the wall temperature ϑ_W. The heat flux density at any place is then

$$\dot{q} = \alpha_\mathrm{ht} \triangle \vartheta = \alpha_\mathrm{ht}(\vartheta_\mathrm{F} - \vartheta_\mathrm{W}) \quad . \tag{2.34}$$

By this definition the temperature of the fluid is assumed to be constant. However, a temperature profile analog to the velocity profile will develop. Consequently, there exists near the wall a boundary layer [79] where the temperature changes from the wall-temperature to the fluid-temperature. Directly at the wall the heat transfer will only occurs via heat conduction and Eq. 2.34 is then the same as Eq. 2.22 leading to

$$\dot{q} = \alpha_\mathrm{ht}(\vartheta_\mathrm{F} - \vartheta_\mathrm{W}) = -\lambda\left(\frac{\mathrm{d}\vartheta}{\mathrm{d}r}\right)_\mathrm{rw} \Rightarrow \alpha_\mathrm{ht} = -\lambda\frac{\left(\frac{\mathrm{d}\vartheta}{\mathrm{d}r}\right)_\mathrm{rw}}{\vartheta_\mathrm{F} - \vartheta_\mathrm{W}} \tag{2.35}$$

and by switching to a non-dimensional notation the Nusselt number can be found as

$$Nu_\mathrm{L} = \frac{\alpha_\mathrm{ht} L}{\lambda} = -\left(\frac{\mathrm{d}\vartheta^*}{\mathrm{d}r^*}\right)_{\mathrm{r}^*=1} \quad . \tag{2.36}$$

The Nusselt number is the ratio between the characteristic length and the thickness of the temperature boundary layer and is used to evaluate the heat transfer coefficients for a existing flow problem.

Natural Convection

In contrast to forced convection, natural convection only occurs via temperature differences in the fluid. These temperature differences create density differences where fluid volumes with higher density rise and those with lower density will descend. Basically, these developed layers are generated by themselves only through this temperature difference. The Nusselt number for free convection is a function of the Grashof number[11] Gr, the Prandtl number, and the geometry

$$Nu_{\mathrm{L}} = \frac{\alpha_{\mathrm{ht}} L}{\lambda} = f(Gr,\, Pr,\, \text{geometry}) u_{\mathrm{L}} \quad . \tag{2.37}$$

The Grashof number is the ratio of the buoyancy to the friction force and describes the same relationships for natural convection as the Reynolds number for forced convection. It can be expressed as

$$Gr = \frac{g \cdot L^3 \beta (\vartheta_{\mathrm{W}} - \vartheta_{\mathrm{F}})}{\nu} \quad , \tag{2.38}$$

where β is the thermal expansion coefficient and g is the gravitational acceleration. In practice, natural convection is often interfered with forced convection. Therefore, a combined Nusselt number (natural and forced convection) is formed [80]

$$Nu_{\mathrm{L}} = \sqrt[3]{Nu_{\mathrm{L,forced}}^3 \pm Nu_{\mathrm{L,free}}^3} \quad , \tag{2.39}$$

where $\pm$ depends on the direction of the flows. The two Nusselt numbers are added up if the flow of the forced convection is parallel to the flow of the natural convection and are deducted if the flows are opposite.

Radiation

Radiation is heat transfer via electromagnetic waves from a hotter body to a cooler one. The length of these electromagnetic waves is in the range from 0.8 to 400 µm. Electromagnetic waves, impinging on a body, are reflected, allowed to pass through (transmission) or absorbed depending on the properties of the body. This is described with Kirchhoff's[12] law of thermal radiation and can be expressed as

$$\alpha_{\mathrm{R}} + \rho_{\mathrm{R}} + \tau_{\mathrm{R}} = 1 \quad , \tag{2.40}$$

where α_{R}, τ_{R}, and ρ_{R} are the adsorption-, the transmission-, and the reflection ratio of an electromagnetic wave, respectively. These parameters depend on the material of the body, its thickness, and on the wave length of the radiation. When the temperature is higher than 0 K every body starts to radiate and this radiation is temperature depended. A so-called black body is able to radiate with maximum

[11] Franz Grashof, German engineer, 1826 - 1893

[12] Gustav Robert Kirchhoff, German physicist, 1824 - 1887

intensity at a certain temperature dependent wavelength. For real bodies, the quantity that takes this into account is the emission ratio ε. The emission ratio defines the radiation intensity of a real body at a certain temperature in relation to the radiation intensity of a black body for the same temperature. Regarding their adsorption, transmission, and reflection ratio bodies are classified into the following classes:

* black: all incident rays are absorbed ($\alpha_\mathrm{R} = \varepsilon = 1$)
* white: all incident rays are reflected ($\rho_\mathrm{R} = 1$)
* gray: all incident rays are absorbed over the entire wavelength range ($\varepsilon < 1$)
* colored: from the incident rays some wave lengths are reflected
* mirroring: all incident rays are reflected at the same angel (oriented to the surface normal)
* flat: incident rays are diffusely reflected in all directions

2.3 Summary of Chapter 2: Theoretical Fundamentals

Fluid mechanics:

* Describes the motion of fluid-particles in mesoscopic time and space scales. Important spatial characteristics are its divergence and its rotation.
* There are two formulations to describe the temporal change in a velocity field: The Lagrange and the Euler formulation. The relation between them is:

$$\frac{\mathrm{d}}{\mathrm{d}t} = \frac{\partial}{\partial t} + (\vec{v} \cdot \vec{\nabla})$$

* The mass flow rate $\dot{m}$ states how much mass is passing through an area per unit of time while the volume flow rate $\dot{V}$ states how much fluid volume is passing through an area per unit of time.
* The Continuity equation for compressible fluids:

$$\frac{\partial \varrho}{\partial t} = -\vec{\nabla} \cdot (\varrho \vec{v}) = -\mathrm{div}\,(\varrho \vec{v})$$

* The General Euler equation for ideal fluids:

$$\frac{\partial \vec{v}}{\partial t} + (\vec{v} \cdot \vec{\nabla})\,\vec{v} = \vec{f} - \frac{\vec{\nabla} p}{\varrho}$$

* In real fluids friction forces have to be taken into account. The Newton's equation of motion turns via convective derivation into the Navier-Stokes equation for incompressible fluids:

$$\frac{\partial \vec{v}}{\partial t} + (\vec{v} \cdot \vec{\nabla})\,\vec{v} = \vec{f} - \frac{\vec{\nabla} p}{\varrho} + \nu \triangle \vec{v}$$

* The dimensionless Reynolds number is defined as inertia force divided by friction force:

$$Re = \frac{uL}{\nu} = \frac{\varrho uL}{\eta}$$

Heat transfer:

* Describes the regularities how heat is transported between systems of different temperatures and it can only occur through heat conduction or thermal radiation. However, heat conduction is split into conduction between solids and static fluids, and into conduction in moving fluids, called convection.
* Relevant parameters are heat, temperature, specific heat capacity, heat flux, heat flux density, heat transfer coefficient, and thermal conductivity.
* Heat conduction in solids or static fluids occurs when a temperature gradient arises in a material. General three-dimensional differential equation for transient heat transfer:

$$\frac{\partial \vartheta}{\partial t} = a\frac{\mathrm{d}^2\vartheta}{\mathrm{d}r^2} = a\nabla^2\vartheta$$

* At forced convection the heat transfer occurs via a temperature difference and a flow. The Prandtl number is temperature-dependent and defined as the ratio of momentum diffusivity to thermal diffusivity:

$$Pr = \frac{\nu}{a} = \frac{\nu\rho c_\mathrm{p}}{\lambda}$$

and the Nusselt number is defined as:

$$Nu_\mathrm{L} = \frac{\alpha_\mathrm{ht}L}{\lambda} = -\frac{\mathrm{d}\vartheta}{\mathrm{d}r}_{\mathrm{r=1}}$$

* Natural convection occurs only via temperature differences in the fluid. In practice, natural convection is often interfered with forced convection. Therefore, a combined Nusselt number (natural and forced convection) is formed.
* Radiation is heat transfer via electromagnetic waves from a hotter body to a cooler one.

Chapter 3

Design and Fabrication

This chapter summarizes the boundary conditions for the thermal flow sensor, the design approaches with simulation results, and a corresponding analytical model. Furthermore, different attempts for fabricating the sensor are described from a historical point of view, pointing out results, drawbacks, and issues for different implementations. At the end, an overview of the different implementations is provided together with the varied parameters.

To avoid any misunderstanding later on, the terms sensor and transducer will be defined first. A sensor is an element that converts a physical quantity into an electrical signal, e.g. atmospheric pressure into a voltage. In many cases this conversion cannot be done within a single step. Two or more conversions are required, e.g. the atmospheric pressure is converted first into the deflection of a membrane. Such converters are called transducers. At the end of the converter chain is the readout, which indicates the membrane deflection as an electrical voltage.

3.1 Analytical Model

An analytical model was developed in order to obtain a qualitative insight of thermal flow sensors. Similar models of such sensors can be found in literature. For instance, Middelhoek et al. [81] developed a one-dimensional model starting from the conservation of thermal energy. Describing the heat balance of an infinitesimal heat flow element in a tube, Rudent et al. [82] gained a one-dimensional thermal model. Nguyen et al. [83] developed a two-dimensional model with the governing equation for the temperature field. However, these models are functional and would require adaption to meet the boundary conditions for this particular problem. Therefore, a new model had to be developed.

The corresponding cross-section of the developed model is depicted in Fig. 3.1 where the sensor is placed in the middle of a flow channel. The flow channel is assumed to be rectangular with height $2\,h_\mathrm{f} + d$. Several assumptions have been made to ease analytical treatment. First, it is assumed that the temperature field does not change along the z-axis which is justified if the lateral extension of all components is much

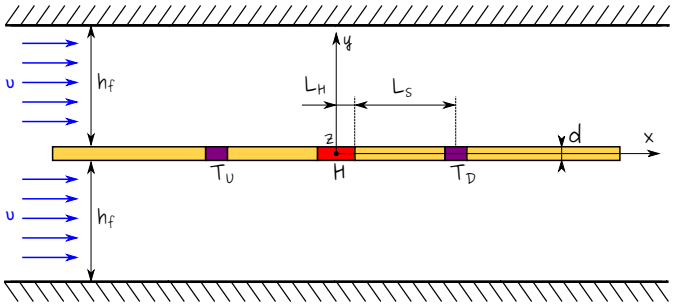

Figure 3.1: Schematic cross-section of the simplified PCB sensor between parallel plates used for analytical modeling. The abscissa coincides with a symmetry axis of the model. The heater H is marked red and the sensing location T_U and T_D are violet. L_H is the half heater length, L_S is the distance from the heater to the middle of the sensing location, h_f is the height of the substrate, d the thickness of the sensor, and v the flow velocity.

larger than their width in the direction of the flow. Next, the boundaries at the beginning ($z = 0$) and at the end ($z = w$) of the sensor in z-direction are neglected resulting in parallel plates of infinite length in z-direction. Another simplification regards the flow in the channel as a uniform flow velocity instead of the typically parabolic one. However, the influence of the flow profile on the temperature of the heater is considered with a boundary layer. Additionally, the heating power is generated by a line source at $x = 0$ and there are no heat losses in z-direction.

In the sensor geometry additional simplifications are assumed. It is modeled as a PCB of uniform thickness with temperature transducers and an embedded heater region. In most fabricated devices, heater and transducers are placed on top of the PCB and may be covered by a protective silk screen printed resist. But these simplifications are justifiable because the PCB material has a significantly larger thermal conductivity than the air in the flow channel. With thin substrates the distortion of the temperature field caused by different material layers on the substrate can be ignored for a first description.

As can be seen in Fig. 3.1, the model is symmetric around the x-axis and this was utilized for a slice to model the heat balance (Fig. 3.2). The goal of this model is to find an approximate expression for the temperature profile $\vartheta(x, y, z)$ along the x-axis as a function of both the mean flow velocity $\bar{v}$ and the heating power P. For these parameters, the temperature at the heater and two sensing positions, which are up- and downstream of the heater, are sought for. Therefore, $\vartheta(x, y)$ is split into $\vartheta(x) \cdot f(y)$ (Fig. 3.2) with

$$f(y) = -\frac{y - (h_\mathrm{s} + \delta)}{\delta} \quad . \tag{3.1}$$

Energy conservation requires that the total heat flux across all surfaces must vanish for each infinitesimal volume (Fig. 3.2), if the system is in a steady state. Due to symmetry and simplifications, there is no heat flow (Eq. 2.23 $\Rightarrow$ 0) through the bottom

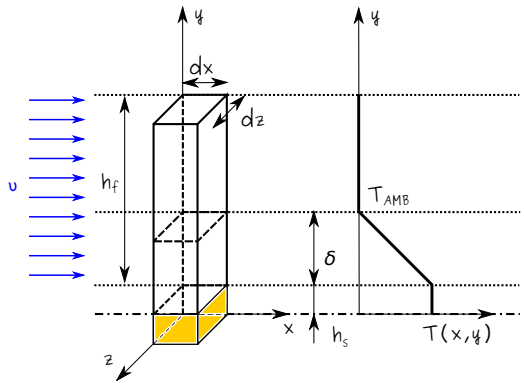

Figure 3.2: 3D slice of the arrangement of Fig. 3.1 (left) and simplified temperature profile assumption perpendicular to the flow direction (right). T_{AMB} denotes the temperature of the fluid (ambient temperature). The different heights h_{s}, h_{f}, and δ are the height of the substrate, the fluid, and the boundary layer, respectively.

boundary surface ($A_{\mathrm{bot}(y=0)} = \mathrm{d}x\,\mathrm{d}z\,(-\vec{e_{\mathrm{y}}})$) and two of the four lateral boundaries ($A_{\mathrm{lat1}(z=0)} = \mathrm{d}z\,(\mathrm{h_s} + \mathrm{h_f}) \cdot (-\vec{e_{\mathrm{z}}})$; $A_{\mathrm{lat2}(z=\mathrm{d}z)} = \mathrm{d}z\,(\mathrm{h_s} + \mathrm{h_f})\,\vec{e_{\mathrm{z}}}$) of the control volume resulting in

$$\dot{Q}_{\mathrm{bot},y} = \dot{Q}_{\mathrm{lat},z(z=0)} = \dot{Q}_{\mathrm{lat},z(z=\mathrm{d}z)} = 0 \quad . \tag{3.2}$$

At the top surface ($A_{\mathrm{top}(y=h_{\mathrm{s}}+h_{\mathrm{f}})} = \mathrm{d}x\,\mathrm{d}z\,\vec{e_{\mathrm{y}}}$) occurs only heat conduction. Therefore, combining Eq. 2.23 and Eq. 3.1 results in

$$\dot{Q}_{\mathrm{top},y} = -\lambda_{\mathrm{f}} \int_0^{\mathrm{d}z} \int_0^{\mathrm{d}x} \frac{\partial \vartheta_{\mathrm{top}}(x,y)}{\partial y}\,\vec{e_{\mathrm{y}}}\,\vec{e_{\mathrm{y}}}\,\mathrm{d}x\,\mathrm{d}z = \lambda_{\mathrm{f}}\vartheta(x)\frac{1}{\delta}\,\mathrm{d}x\,\mathrm{d}z \quad , \tag{3.3}$$

where λ_{f} is the thermal conductivity of the fluid and δ is the boundary layer thickness.

The two remaining lateral surfaces are both split into two subareas. At the first subarea ($A_{\mathrm{sub1}} = h_{\mathrm{s}}\,\mathrm{d}z\,\vec{e_{\mathrm{x}}}$) occurs only heat conduction (substrate). To ease mathematical treatment the subareas at the position $x = 0$ and $x = \mathrm{d}x$ are put together which leads to

$$\begin{aligned} \dot{Q}_{\mathrm{sub},x} &= -\lambda_{\mathrm{s}} \int_0^{\mathrm{d}z} \int_0^{h_{\mathrm{s}}} \left[\frac{\partial \vartheta_{\mathrm{sub}}(x,y)}{\partial y} \cdot (-\vec{e_{\mathrm{x}}})\,\vec{e_{\mathrm{x}}} + \frac{\partial \vartheta_{\mathrm{sub}}(x+\mathrm{d}x,y)}{\partial y}\,\vec{e_x}\,\vec{e_{\mathrm{x}}} \right] \mathrm{d}y\,\mathrm{d}z \\ &= -\lambda_{\mathrm{s}} \frac{\partial^2 \vartheta(x)}{\partial x^2} h_{\mathrm{s}}\,\mathrm{d}x\,\mathrm{d}z \quad , \end{aligned} \tag{3.4}$$

where λ_{s} is the thermal conductivity of the substrate. At the second subarea ($A_{\mathrm{sub2}} = h_{\mathrm{f}}\,\mathrm{d}z\,\vec{e_{\mathrm{x}}}$) occur both heat conduction and convection. Like before, to ease mathematical treatment the subareas at the position $x = 0$ and $x = \mathrm{d}x$ are put

together. The heat conduction part can be expressed as

$$\begin{aligned}\dot{Q}_{\mathrm{fluid,con},x} &= \lambda_\mathrm{f} \int_0^{\mathrm{d}z} \int_{h_\mathrm{s}}^{h_\mathrm{s}+\delta} \left[\frac{\partial \vartheta_\mathrm{fluid}(x,y)}{\partial x} \cdot (-\vec{e_\mathrm{x}})\, \vec{e_\mathrm{x}} + \frac{\partial \vartheta_\mathrm{fluid}(x+\mathrm{d}x,y)}{\partial y}\, \vec{e_x}\, \vec{e_\mathrm{x}} \right] \mathrm{d}y\, \mathrm{d}z \\ &= -\lambda_\mathrm{f} \frac{\partial^2 \vartheta(x)}{\partial x^2} \cdot \frac{\delta}{2}\, \mathrm{d}x\, \mathrm{d}z \quad ,\end{aligned} \tag{3.5}$$

whereas, the convective part can be expressed as

$$\begin{aligned}\dot{Q}_{\mathrm{fluid,cov},x} &= \rho c_\mathrm{p} \int_0^{\mathrm{d}z} \int_{h_\mathrm{s}}^{h_\mathrm{s}+\delta} [\vartheta_\mathrm{fluid}(x,y) \bar{v} (-\vec{e_\mathrm{x}})\, \vec{e_\mathrm{x}} \quad + \\ &+ \quad \vartheta_\mathrm{fluid}(x+\mathrm{d}x,y) \bar{v}\, \vec{e_x}\, \vec{e_\mathrm{x}}]\, \mathrm{d}y\, \mathrm{d}z \quad = \quad \rho c_\mathrm{p} \bar{v} \frac{\partial \vartheta(x)}{\partial x} \cdot \frac{\delta}{2}\, \mathrm{d}x\, \mathrm{d}z \quad ,\end{aligned} \tag{3.6}$$

where ρ is the mass density of the fluid and c_p is the specific heat capacity at constant pressure.

The sum of the heat flux (Eq. 3.2-3.6) through all surfaces is set to zero and, after simplification, the differential equation for the model is found as

$$\left(\lambda_\mathrm{f} \frac{\delta}{2} + \lambda_\mathrm{s} h_\mathrm{s} \right) \cdot \frac{\partial^2 \vartheta}{\partial x^2} - \rho c_\mathrm{p} \bar{v} \frac{\delta}{2} \cdot \frac{\partial \vartheta}{\partial x} - \lambda_\mathrm{f} \frac{1}{\delta} \vartheta = 0 \quad , \tag{3.7}$$

Inserting the thermal diffusivity a (see Sec. 2.2) and with the ansatz

$$\vartheta = c_1\, e^{\alpha x} + c_2, \quad \frac{\partial \vartheta}{\partial x} = \alpha c_1\, e^{\alpha x}, \quad \frac{\partial^2 \vartheta}{\partial x^2} = \alpha^2 c_1\, e^{\alpha x} \quad , \tag{3.8}$$

the differential equation (Eq. 3.7) can be solved with the eigenvalues

$$\alpha_{1,2} = \frac{\bar{v}\delta\lambda_\mathrm{f}}{a(\lambda_\mathrm{f}\frac{\delta}{2} + \lambda_\mathrm{s} h_\mathrm{s})} \pm \sqrt{\left(\frac{\bar{v}\delta\lambda_\mathrm{f}}{a(\lambda_\mathrm{f}\frac{\delta}{2} + \lambda_\mathrm{s} h_\mathrm{s})} \right)^2 + \frac{\lambda_\mathrm{f}\frac{1}{\delta}}{\lambda_\mathrm{f}\frac{\delta}{2} + \lambda_\mathrm{s} h_\mathrm{s}}} \quad . \tag{3.9}$$

From Eq. 3.8 follows immediately that c_2 represents the ambient temperature (T_amb). Another boundary condition is that the temperature varies continuously along the x-axis. However, the heating power has to be considered. Therefore, the temperature equilibration was expanded with the generated heating power. The boundary conditions are set to

$$\begin{aligned}\vartheta_\mathrm{U}(x=0) &= \vartheta_\mathrm{D}(x=0) \\ -\lambda_\mathrm{s} \frac{\partial \vartheta_\mathrm{U}}{\partial x}_{(x=0)} &+ \lambda_\mathrm{s} \frac{\partial \vartheta_\mathrm{D}}{\partial x}_{(x=0)} = \frac{P}{A} \quad ,\end{aligned} \tag{3.10}$$

where $\vartheta_\mathrm{U,D}$ represents the temperature behavior up- and downstream of the heater (position $x = 0$), P is the heating power, and A is the heater area. The heat source in the model is considered as a point-like source at the position $x = 0$. The real source, however, generates the heat at the area A (Fig. 3.1 - H). Therefore, the

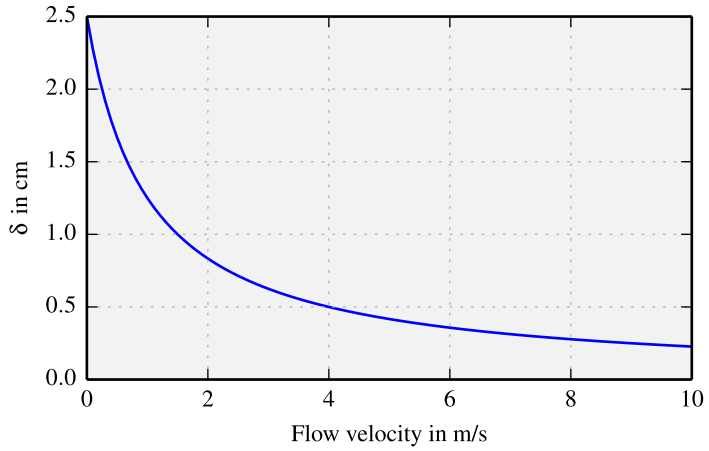

Figure 3.3: Thickness of the thermal boundary layer δ as a function of the mean flow velocity according to the mathematical model (see Eq. 3.12).

generated heating power is imposed into the model via the expression P/A. With $\alpha_1 = -\alpha_2$ and the boundary conditions (Eq. 3.10) the final solution can be found as

$$\vartheta(x) = \left\{ \begin{array}{ll} \dfrac{P}{\lambda_\mathrm{s} \cdot A} \cdot \dfrac{1}{2\alpha_2}\, e^{\alpha_2 x} + T_\mathrm{amb} & , \quad -\infty < x \leq 0 \\ \\ \dfrac{P}{\lambda_\mathrm{s} \cdot A} \cdot \dfrac{1}{2\alpha_2}\, e^{-\alpha_2 x} + T_\mathrm{amb} & , \quad 0 \leq x < \infty \end{array} \right\} \quad . \tag{3.11}$$

The assumed temperature field of the model drops linearly in y direction until the distance δ is reached (see Fig. 3.2). δ denotes the thickness of this temperature boundary layer in the flow channel. It is obvious that δ depends on the mean flow velocity $\bar{v}$. Higher velocities will increase the cooling effect and thus make this boundary layer thinner. Similar models in literature [81–83] did set the boundary layer thickness to a constant value. However, for this developed model the thickness of the temperature boundary layer is modeled as

$$\delta = \frac{h_\mathrm{s}}{1 + v_\mathrm{x}^*} \quad , \tag{3.12}$$

where v_x^* is a characteristic velocity in x-direction with $v_\mathrm{x}^* = \bar{v}/\Upsilon$ and Υ is the inflow velocity (*Anströmgeschwindigkeit* [84]). This approach gives plausible δ values also in extreme cases such as zero velocity (thermal layer extends towards the channel walls) or for very high velocities (boundary layer nearly vanishes). Figure 3.3 depicts the computed dependency $\delta\,(\bar{v})$ for the model parameters presented in Tab. 3.1.

The targeted calorimetric principle evaluates the temperature difference between two sensing positions located up- and downstream from a heater. The temperature profile along the x-axis is given by Eq. 3.11. Figure 3.4 depicts the excess temperature for a heating power of 100 mW. Without any flow (blue line) the temperature profile is symmetric at the heater. On the contrary, with flow, the excess temperature decreases because of the stronger cooling effect. Moreover, the upstream side

Symbol	Value	Parameter
h_f	25 mm	Height of the half channel diameter
d	140 µm	Thickness of the substrate
$h_\mathrm{s} = d/2$	70 µm	Height of the half substrate
L_S	1 mm	Distance sensor - heater
ρ	1.2 kg/m^3	Mass density of air
c_p	1005 J/kgK	Specific heat capacity (con. pressure) of air
λ_f	0.026 W/mK	Thermal conductivity of air
λ_s	0.3 W/mK	Thermal conductivity of FR4

Table 3.1: Parameter values used for the analytical model.

is cooled more than the downstream part, which is the expected asymmetric profile of the temperature field (green and red line).

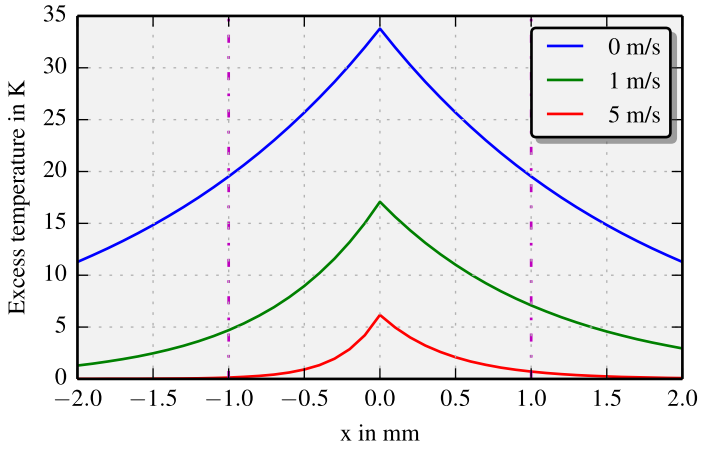

Figure 3.4: Excess temperature at the sensor surface along the x-axis. The heating power was set to 100 mW for three different velocities $(0, 1, 5\,\mathrm{m/s})$. The vertical dashed lines represent the location of the embedded temperature sensors.

In the next step, the excess temperature is evaluated at the sensor location (for example: $x_\mathrm{Upstream} = -1.0\,\mathrm{mm}$ and $x_\mathrm{Downstream} = 1.0\,\mathrm{mm}$ into Eq. 3.11) as a function of the mean flow velocity. Figure 3.5 shows both up- and downstream excess temperatures at the sensor locations as well as their difference as a function of the mean flow velocity. The temperature difference shows typical features of calorimetric sensors with a steep rise up tp the maximum followed by a slow decline which is responsible for the ambiguity of the transduction characteristic. This characteristic and the useful measurement range depends on various parameters. A decisive contribution emerges from the eigenvalues α_1 and α_2 (see Eq. 3.9). Their most substantial term

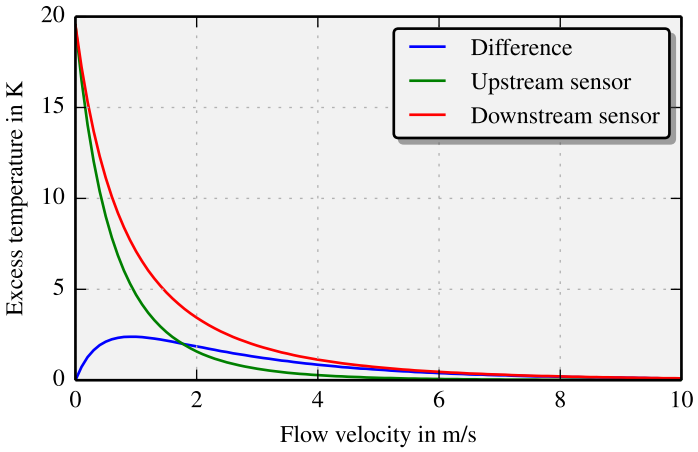

Figure 3.5: Excess temperatures of the two sensing locations as well as their temperature difference.

$\bar{v}\delta\lambda_\mathrm{f}/(a(\lambda_\mathrm{f}\delta/2 + \lambda_\mathrm{s}h_\mathrm{s}))$ reveals the peak of the excess temperature difference with respect to flow velocity. It depends strongly on the thermal diffusivity a of the medium which means for media with a smaller diffusivity the measurement range would be significantly smaller. It also depends strongly on the thickness δ of the boundary layer which favors miniaturized sensors and brings challenges for macroscopic devices like a PCB based one.

Another big influence has the fraction $P/(\lambda_\mathrm{s}A)$, see boundary conditions Eq. 3.10, which represents the generated heating power. Increasing the power will result in a higher temperature difference but a threshold, depending on the sensor and the fluid, may not be exceeded to prevent thermal damage. Therefore, suitable power values where flow rates can be measured accurate enough have to be found. The position of the temperature sensors L_S modifies also the output characteristic. As a rule of thumb, the closer the sensing points are, the larger the measurement range and the smaller the output signal.

Why only use two sensing locations? Can the sensor be improved by using more than two sensing elements? An relatively simple enhancement of the sensor characteristic can be achieved with two additional sensing elements. Now, a full Wheatstone bridge[1] can be formed as Talic et al. [85] performed with four germanium thermistors. Figure 3.6 compares readout results for the two and four location approach. Thereby, two additional sensing elements have been inserted, e.g., at the locations $x_\mathrm{Upstream} = -0.5\,\mathrm{mm}$ and $x_\mathrm{Downstream} = 0.5\,\mathrm{mm}$ ("Full bridge I"). As expected, the summed excess temperature differences increase the feasible sensor output by a factor of two and, in addition, the arrangement of four locations gives more design space for the transduction characteristic. For example, when moving the sensor locations closer to the heater ($x1_\mathrm{Upstream} = -0.25\,\mathrm{mm}$; $x2_\mathrm{Upstream} = -0.75\,\mathrm{mm}$; $x1_\mathrm{Downstream} = 0.25\,\mathrm{mm}$; $x2_\mathrm{Downstream} = 0.75\,\mathrm{mm}$) the output signal decreases while the measurement range increases ("Full bridge II").

[1] Charles Wheatstone, British physicist, 1802 - 1875

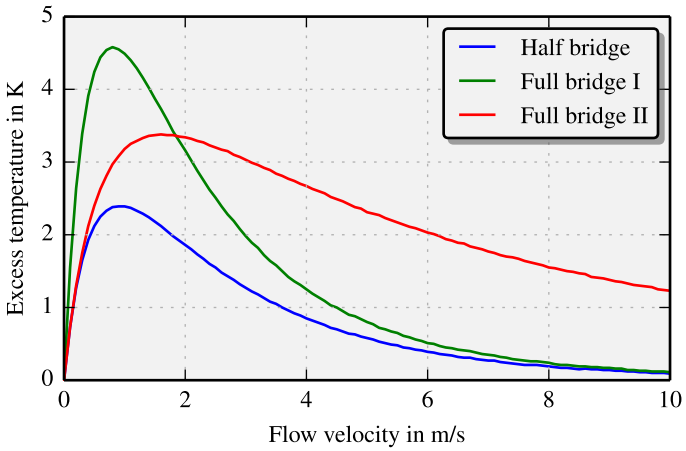

Figure 3.6: Temperature difference of two sensing locations in comparison with four sensing locations. Additionally, the position of the four sensing locations has been varied.

Nonetheless, this model provides a rough overview of the design influence on the sensor characteristic. Within the technological limits of a certain PCB producer it should be possible to finetune sensor parameters by finite element simulations for optimum measurement range or high sensor efficiency.

3.2 Simulation

2D-FEM (Finite Element Method) models were built in order to predict the sensor characteristic of feasible setups and to optimize their design parameters. Since all sensor components (sensing elements and heater) exhibit large extensions perpendicular to the flow direction, two-dimensional modeling seems reasonable. However, close to the flow channel walls there will be nearly no flow and the model-intrinsic 2D temperature profile deviates from the actual temperature field. Therefore, 3D-FEM simulations have been carried out to investigate the velocity field in the flow channel. The results of the 3D simulations are implemented into 2D simulations via a small correction coefficient (velocity magnitude) to achieve similar conditions.

The Comsol Multiphysics simulation tool has been chosen for the simulations. The applied conjugated heat transfer model combines the heat transfer module with the laminar flow module. It solves the incompressible Navier-Stokes equation (Eq. 2.18) to get the velocity field inside the flow channel and near the sensor. Subsequently, the heat transfer equations, including conductive and convective heat transfer (see Sec. 2.2), are solved. The model is based on the cross-sectional view depicted in Fig. 3.7. More detailed dimension of the design are explained in the subsequent sections whereas the corresponding CAD drawings can be found in the appendix (see Sec. A.1 and A.2).

The flow channel in the simulation has a diameter of 5 cm with a length of 10 cm. The sensor is inserted into the channel via a small slit in the channel walls and stretched

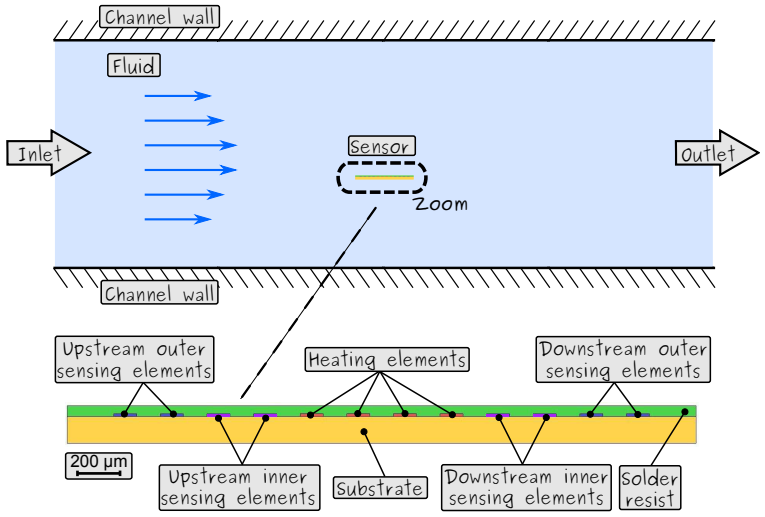

Figure 3.7: FEM model cross-section: The sensor is placed in the middle of a flow channel (height: 5 cm, length: 10 cm). Top and bottom of the flow channel are set to walls whereas the left side is an inlet and the right side an outlet of the streaming fluid. Sensor (Zoom): On top of the substrate (FR4 glass epoxy) there are the heating elements (copper), the sensing elements (copper) covered by a solder resist (polyimide).

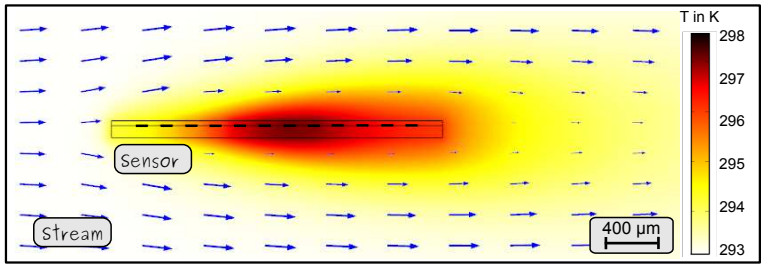

Figure 3.8: Result of the transient FEM simulation after 20 s where only a section around the sensor is shown. The color indicates the temperature distribution for a heating power of $P_{\mathrm{tot}} = 100\,\mathrm{mW}$ while the blue colored arrows indicate the velocity field at a mean flow velocity of $\bar{v} = 0.5\,\mathrm{m/s}$.

over the entire diameter. Therefore, the PCB surface is aligned longitudinal to the flow direction. Furthermore, the sensor is placed at the center of the flow channel with air as surrounding fluid. A parabolic flow velocity profile (laminar and mean flow velocity) is imposed from the left hand side inside into the flow channel (Fig. 3.8) with an entrance length of 1 m. The outlet (right side) is chosen to be a normal flow with zero pressure ($p_{\mathrm{o}} = 0\,\mathrm{Pa}$) and suppressed backflow. Additionally, the top and bottom flow channel walls, inlet, and outlet, are set to a constant temperature of 293.15 K, whereas, the non-slip boundary condition (Eq. 2.19) is applied to all solid surfaces. The sensor solid surfaces are set to an initial temperature of 293.15 K.

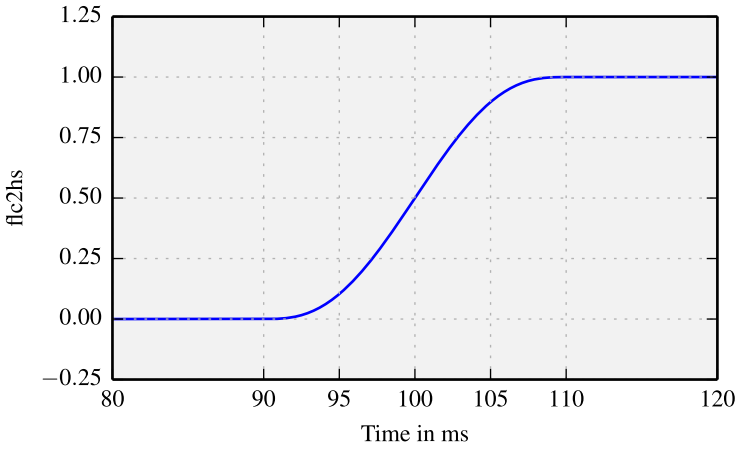

Figure 3.9: Smoothed Heaviside function (Comsol: flc2hs) with a continuous second derivative without overshoot for applying the heating power in the simulation.

The heating power is set via the overall heat transfer rate:

$$Q = \frac{P_{\text{tot}}}{V_{\text{heater}}} \quad , \tag{3.13}$$

with V_{heater} as the volume of the heater, and P_{tot} as the total generated power. The volume V_{heater} is calculated with the cross-sectional area and the extension in z-direction of the model which is set to the flow channel diameter (5 cm). The total power is applied to the system via a smoothed Heaviside [2] function with a continuous second derivative without overshoot (Fig. 3.9) [86]. This function (Comsol: flc2hs) interpolates smoothly between two values (0.09 and 0.11) based on a third one (0.01) and the returned value is clamped between 0 and 1. The function is defined as

$$flc2hs = \left\{ \begin{array}{ccc} 0 & , & t < 0.09 \\ f(t) & , & 0.09 \leq t \leq 0.11 \\ 1 & , & t > 0.11 \end{array} \right\} \quad , \tag{3.14}$$

where t is the time in seconds and f(t) is expressed as

$$f(t) = 0.5 + 0.94\frac{t-0.1}{0.01} - 0.63\left(\frac{t-0.1}{0.01}\right)^3 + 0.19\left(\frac{t-0.1}{0.01}\right)^5 \quad . \tag{3.15}$$

Constant Heating Mode

The simulations are performed in two steps. First, the laminar flow module solves the stationary Navier-Stokes equation (Eq. 2.18) because the flow velocity is assumed

[2] Oliver Heaviside, English electrical engineer, mathematician, and physicist, 1850 – 1925

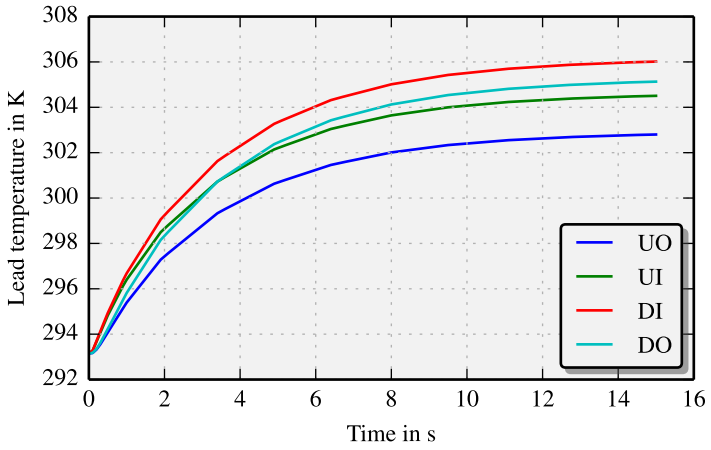

Figure 3.10: Simulated temperature transients of all four sensing leads (heating power $P_{\text{tot}} = 100\,\text{mW}$, mean flow velocity $\bar{v} = 0.5\,\text{m/s}$). The lead temperatures reach the stationary state after about 15 s (leads: D...downstream, U...upstream, O...outer, I...inner).

to be not influenced by subsequent temperature variations due to the heating power. Next, with the obtained velocity field, the transient temperature field in response to the heating power is computed with a time dependent solver. In Fig. 3.8 the temperature distribution (color) and the velocity field (arrows) after 20 s of the simulation are shown where a heating power of 100 mW and a mean flow velocity of 0.5 m/s are applied. With post processing algorithms the temperatures of all sensing leads (Fig. 3.10) are derived. In detail, four surface integrals, over the corresponding sensing lead cross-sections (UO - upstream outer, UI - uptsream inner, DI - downstream inner, DO - downstream outer), are performed for each simulation time step to get the time dependent thermal behavior of each lead. These curves reveal the delay time for the settlement of the temperature field that equals the waiting time for accurate flow measurements in case of an intermittent heater operation.

In a further step, the described simulation scheme is repeatedly executed to enable a parametric sweep where the mean inlet flow velocity is varied. The laminar flow and the heat transfer module are solved for different mean inlet flow velocities $\bar{v}$ ($0.1 - 10\,\text{m/s}$, $\Delta\bar{v} = 0.1\,\text{m/s}$). For each velocity, the time dependent thermal behavior of the sensing leads is evaluated. In a post processing step the stationary temperature of each sensing lead is calculated and then plotted over the mean flow velocity (Fig. 3.11). The results of these simulations show the temperature change of the sensing leads depending on the flow velocity and confirm that the targeted transduction principle is feasible.

Constant Temperature Mode

The simulation model is adapted to describe the constant temperature mode (see Sec. 1.3). There is no urgent need for a time dependent simulation here, only the

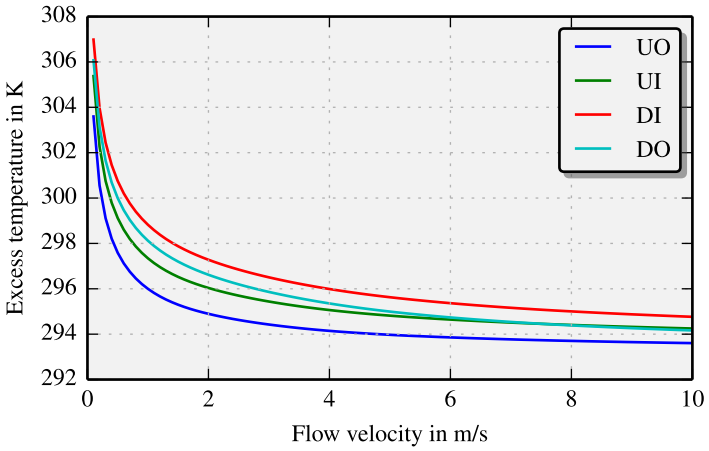

Figure 3.11: Stationary excess temperatures of the sensing leads (taken 15 s after heat onset) versus the mean inlet flow velocity ($0.1 - 10\,\mathrm{m/s}$) at 100 mW heating power (leads: D...downstream, U...upstream, O...outer, I...inner).

stationary behavior is of primary interest. First, the heating power p_H is added as additional parameter representing a variable heat source. With this parameter a parameter sweep is set up where the solver calculates pressures, velocities, and temperatures for several mean inlet velocities and heating powers. The range of the mean inlet velocity $\bar{v}$ is $0.1 - 10\,\mathrm{m/s}$ ($\Delta\bar{v} = 0.1\,\mathrm{m/s}$) and the range of the heating power p_H is $0 - 1.8\,\mathrm{W}$($\Delta p_\mathrm{H} = 4\,\mathrm{mW}$). Depending on the chosen step size of the parameter sweeps, the number of resulting pressures, velocities, and temperatures for all leads can be tremendous which causes the simulation time to increase dramatically. Therefore, only 1600 values (40×40) are set for the parameter sweeps and, consequently, 1600 temperatures (matrices) are computed for every lead. In a post processing step each matrix is enlarged to 160000 temperature values (400×400) with a bivariate spline approximation over the rectangular mesh. This time saving approximation is feasible because one matrix with 160000 temperature values was simulated, compared with the approximation and the calculated error of the approximation is below 0.01%.

Next, the signal U_2 (see Eq. 4.9) was evaluated from the four sensing lead matrices resulting in one temperature difference matrix (Fig. 3.12). A specific temperature difference was chosen and from the related contour line the corresponding matrix indices are identified. They point to the required heating power for the selected temperature difference and are stored in a heating power array. By combining the resulting heating power array with the temperature characteristic of the heating resistor, the needed heater voltage for the mean flow velocity can be calculated. Figure 3.13 depicts the heater voltage for three temperature differences ($U_2 = 2\mathrm{K}; 4\mathrm{K}; 6\mathrm{K}$) as a function of the mean flow velocity.

This simulation revealed the voltage directly needed at the heater lead. In reality, there are additional supply lines to the heater lead, contact resistances, and with the low resistance value of the heater lead (see Sec. 4.1), the resulting current may

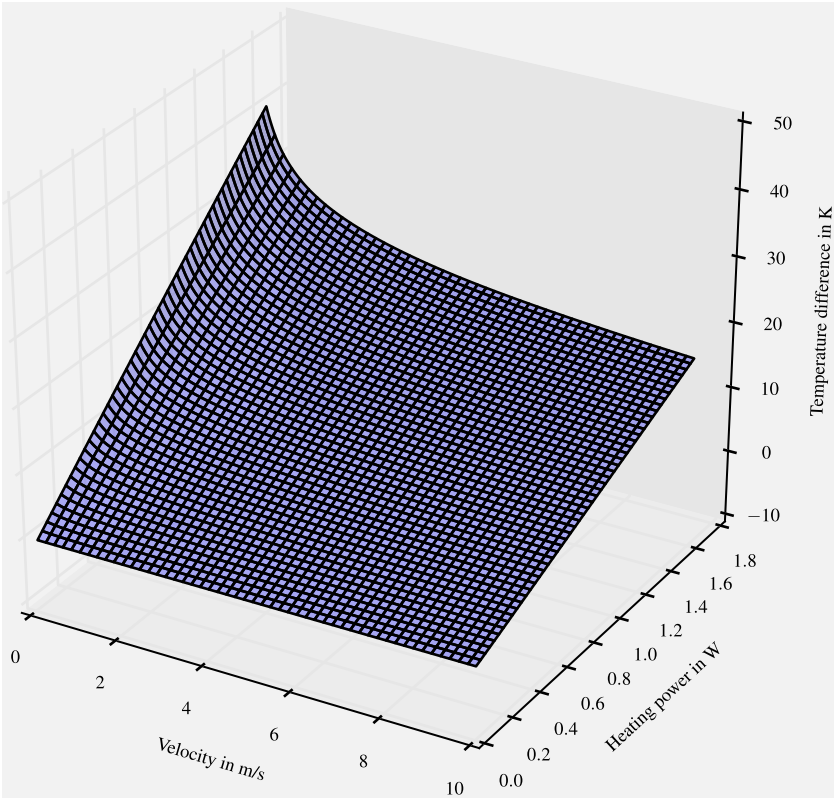

Figure 3.12: 3D plot of the simulated temperature difference as a function of the mean flow velocity as well as the heating power. The surface depicts how much temperature difference occurs between the inner sensing leads and the other ones which correspond to the signal $U_2(v, p_\mathrm{H})$. The shown data is derived from four temperature matrices (one for each sensing lead).

be to high for the IC to provide. This means, a series resistance may has to be kept in mind because the heater voltage will be higher in reality than in the simulations.

As can be seen, the function now increases monotonically with increasing flow velocity from 0 up to 10 m/s which is required for HVAC systems as for the objective of this thesis. Detailed simulation results are compared to measurements and explained in Sec. 4.1-4.3. Moreover, additional information on simulation results can be found in literature [87–89].

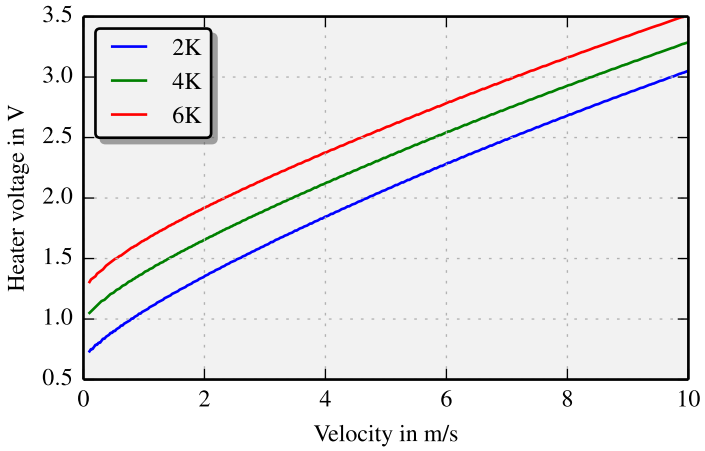

Figure 3.13: Simulated heater voltage U_{H} as a function of the mean flow velocity. Three characteristics are depicted depending on the preselected temperature difference U_2.

3.3 Proof-of-Concept

Based on the results of the analytical model and the simulations, and considering the design rules of a typical PCB producer, an initial sensor layout for a calorimetric sensor was designed. The standard flexible printed circuit board technology was chosen for an easy choice of potential producers. After comparing several PCB producers PIU-Printex GmbH was selected due to the flexibility to react to potential non-standard requests. It was also easily possible to visit the facility to get an impression of the equipment and a feeling for the required process steps.

PCB-Fabrication

The substrate of the sensor, the dielectric, is a conventional FR4 glass epoxy laminate (FR4 - 104) from Isola exhibits a thickness of $100 \pm 13\,\mu\mathrm{m}$. For manufacturing the prepreg (type MC-Rheopreg): resin, curing agent, catalyst, and solvent are mixed together to a batch which is then coated on a reinforcement (woven fiberglass cloth). Next, the coated cloth is pulled through a series of heating zones and then rewound into rolls or cut into sheets.

The laminate type MC-100MS/MC-100EX is manufactured by combining prepreg and a specific resin with the desired copper foils. Prepegs and copper foils are cut to the desired size and then stacked. These stacks are loaded into a lamination press, where pressure, temperature, and vacuum are applied to produce the desired copper clad laminate [90]. Relevant properties of this substrate for the flow sensor are the thermal conductivity $\lambda_{\mathrm{FR4}} = 0.38\,\mathrm{W/mK}$ and the specific heat $c_{\mathrm{p}} = 920\,\mathrm{J/kgK}$.

A one-sided flexible copper laminate was used for the proof-of-concept as conducting path (transducers) with an initial thickness of $18 \pm 3\,\mu\mathrm{m}$, which is the standard thickness for multilayer PCB's. Relevant properties of copper for this thesis are

the temperature coefficient of resistivity $\alpha = 3.66 \cdot 10^{-3}\,1/\mathrm{K}$ [91] and the electrical resistivity $\rho = 16.7 \cdot 10^{-9}\,\Omega\mathrm{m}$ (at 20°C) [92]. With the assessment equation of resistance [93]:

$$R = \frac{\rho L}{A} \quad , \tag{3.16}$$

the resistance of one transducer, sensing copper lead, (length, width, and thickness of 50 mm, 100 µm, and 18 ± 3 µm, respectively) is $0.9 \pm 0.18\,\Omega$ at 20°C. However, such small resistance values are not easy to measure with precision. First, the contacts between the PCB sensor and the electronic terminals may vary irregularly due to coatings, oxides or dirt. Second, the resistance of the connecting lines can be to high to measure the resistance of the copper leads accurately enough. Third, high measurement currents required for sufficient resistance resolution can pose a problem. Additionally, they require specific current sources that are hard to realize with compact microelectronic circuits. Fourth, high measurement currents can cause excessive self-heating of the sensing leads which has to be considered for accurate sensor modeling. Last, noise (e.g.: thermal noise or electromagnetic interference) will limit the ultimate resolution of resistance measurements related to a given bandwidth.

For a constant applied voltage, the thermal fluctuation of the measurement currents are in proportion to the square root of the electrical conductance of the leads. Therefore, increasing the resistance of these leads will improve the overall performance of the sensor. There are two options to achieve a higher lead resistance: Increasing the length of the sensing lead or decreasing its cross-section.

* The meander length l_M of the leads is limited by the diameter of the flow channel. Nevertheless, sensors with 10, 15, 20, 30, 50 and 60 mm meander lengths have been fabricated for a statistical investigation of the meander length to lead resistance ratio.
* Another potential improvement is to increase the number of meander loops. The drawback of this method is the broadening of the structure. By increasing the distance of the heater, the excess temperatures decreases which reduces the sensitivity of the sensor.
* The cross-section of the leads on the PCB can be decreased by reducing width and/or thickness of the lead. The width of all leads is fixed to 100 ± 5 µm by the typical design rules. So, the remaining parameter for increasing the resistance is the thickness of the lead. It can be reduced by wet etching. This is a common process step in the fabrication of PCBs to achieve the desired circuit structure.

As a result, to increase the sheet resistance of the leads, the initial thickness of 18 µm was reduced to about 9 µm by an additional run in the etching system after removing the etch resist. As a result, the expected lead resistances should increase from $0.9\,\Omega$ to $1.8\,\Omega$. Finally, the resulting leads are protected from corrosive media by a polymer layer. It is a photostructurable kapton solder resist (polyimide film) with a thickness of 30 ± 10 µm.

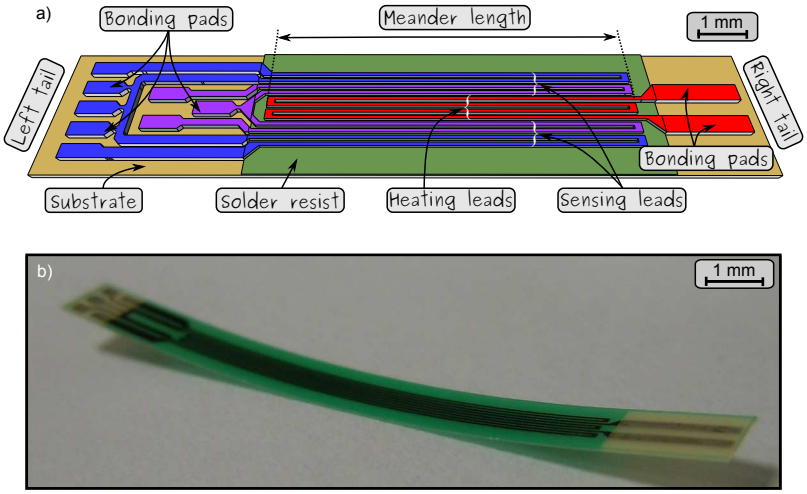

Figure 3.14: Schematic (a) and photograph (b) of the proof-of-concept sensor: The length of the meander l_M is 50 mm and the overall thickness is 130 µm (100 µm substrate and 30 µm copper with covering solder resist). The heater lead (red) is a meander of order 2, the sensing leads (purple and blue) consist of meander of order 1 each. The substrate material (brown beige) is FR4 glass epoxy on which there is a solder resist (green). At the left and right tail of the sensor there are bonding pads which are not covered with the solder resist.

Sensor Design

In the design of the proof-of-concept sensor (Fig. 3.14) one heating lead is placed in the middle of four transducers (sensing leads), two positioned upstream and two downstream. The width of all these leads as well as the gap between neighboring leads amount 100 ± 5 µm. The inner sensing leads are connected with a shared bond pad as well as the outer ones. This setup allows an easy formation of a Wheatstone bridge for a convenient sensor readout. On the right tail of the sensor there are two bond pads for the heater lead. On the left tail there are three bond pads for the inner sensing leads and five bond pads for the connection to the outer sensing leads. The three middle pads are next to each other to compensate for small resistance differences by bonding to one of them. However, this compensation was not required, so this idea was discarded in later designs.

The proof-of-concept sensor design should show that the targeted sensor principle is feasible but preliminary measurements (Sec. 4.1) revealed minor issues. First of all, the precision of the leads was worse than assumed which meant the reproducibility of the sensor was not given for the targeted application. The main reason was found in the additional etching step and therefore, another production technology without this step was mandatory. Next, at various experiments the two sided soldered interconnection proved itself as disturbing elements which lead to a rework of the interconnection. All in all, designing a new sensor was necessary at this point to continue which is presented in the next section.

3.4 PCB Sensor Prototype

First Prototype Layout

The layout of the first prototype family is depicted in Figure 3.15. PCBs with 10, 30, and 50 mm meander lengths (l_{M}) have been produced. There are several major improvements compared to the proof-of-concept design.

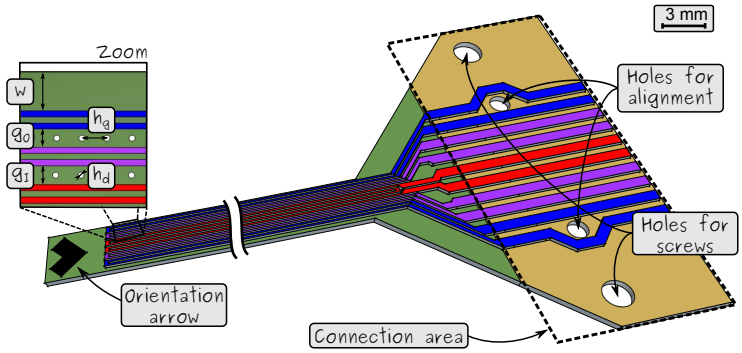

Figure 3.15: Schematic view of the first prototype sensor. The heating lead is colored red while the sensing leads are shown in blue and purple. A black arrow near the tip indicates the orientation of the sensor on the production multiple. It is intended to correlate experimental results with respect to the direction of the etchant flow. The green color represents the area covered by a solder resist layer and the substrate is colored brown-beige. The bonding pads are replaced by an area for an connector, equipped with holes for alignment pins and screws. A detail of the sensor gives an overview of the varied parameters: g_{I} and g_{O} denote the gap between the inner and outer sensing leads, respectively. h_{d} means the diameter of perforation holes, h_{g} is the hole spacing, and w specifies the distance between the outmost lead and the PCB edge (=wing).

First of all, a new laminate in form of electro-deposited copper foils is used for the production of the copper layer on the PCB. These copper foils are fabricated from a high grade pure copper which is dissolved in sulfuric acid (H_2SO_4) forming the copper electrolyte solution. Proprietary additives allow the modification of the resulting copper foil structure. The solution is pumped through filtering systems into large plating tanks containing partially immersed titanium drums. As the drum rotates slowly, a thin film of very pure copper is electro deposited onto its surface and rolled up (drum foil). Afterwards, the drum foil is processed through a sequence of chemical and electro-chemical processing steps to meet the specific final product attributes. Finally, the foil (functional foil) is sliced to the precise widths and attached onto a carrier foil. This $70 \pm 7\,\mu\mathrm{m}$ thick carrier protects the thin functional foil from contamination and mechanical damage during stacking and lamination. An intermediate layer based on metallic chromium is inserted between carrier and functional foil to provide the release of the functional foil. This organic-free layer

totally adheres on the carrier foil after peeling, leaving an ultra clean functional copper laminate surface. The achieved uniformity of the copper thickness is much better than what can be obtained by thinning 18 µm foils down with any large area etching step. For the first sensor prototype, the height of the remaining functional copper layer is 9 ± 2 µm while the width of the leads remains the same as in the proof-of-concept design with 100 ± 5 µm.

Another improvement is that the bond pads of the heater lead are placed between the sensing leads pads for better interconnectivity. The width of the heater leads are slightly increased as they come near to the bond pads to minimize the heating effect outside the flow channel. However, preliminary simulations have revealed that this improvement is very limited. These studies focused on excess temperature distribution due to joule heating in the copper of the heater lead. The overall dissipated power was 100 mW while the share of the connection pads ranged under 0.5 mW. Hence, all connections can be located nearby without causing thermal problems.

After measurements of the reproducibility of the contact resistance of soldered connections to the bond pads, this method was abandoned in favor of mechanical contacts between contact areas and female PCB edge connectors (see Tab. 4.1). This connection technology greatly simplifies the handling of the sensor in various experiments and measurements. Additionally, the region near the pads was equipped with holes for screws and alignment pins to position the sensor exactly with respect to the connector pins. Thereby, a reliable low resistance connection can be established.

Another feature is the orientation mark (arrow) on the tip of the sensor in comparison to the proof-of-concept design. This mark is deposited on top of the solder resist as part of a legend layer and indicates the orientation and placement of the sensor on the PCB master during fabrication. The sensors on the PCB master are oriented in all four orthogonal directions. This was necessary to reveal possible dependencies of the lead characteristics on the flow direction of the copper etchant. After measuring the resistance values (see Sec. 4.1) and relating the results to the orientation on the master PCB, the suspicion of a preferred lead orientation could be withdrawn.

Another design variation concerns the gap between the leads. The gap width has been enlarged in steps of 100 µm starting from the initial 100 µm to 300 µm, to study its influence on the sensor conversion characteristic (see Fig. 4.16). To vary the heat conduction in the substrate, one-dimensional hole arrays have been drilled through the substrate between neighboring leads of several prototypes. These holes have 100 µm in diameter and 100 µm or 300 µm spacing between each other. See Tab. 3.2 for detailed information.

The first prototype layout confirmed a correlation between the resistance change while heating and the flow velocity in the flow channel. Additionally, the precision of the leads improved dramatically but was not satisfying at the point. Moreover, the targeted measurement range could not be covered, therefore, another layout was necessary.

Second Layout

Figure 3.16 depicts the second prototype sensor design. Only sensors with a meander length l_M of 50 mm were manufactured. Further improvements have been implemented based on results of previous flow measurements.

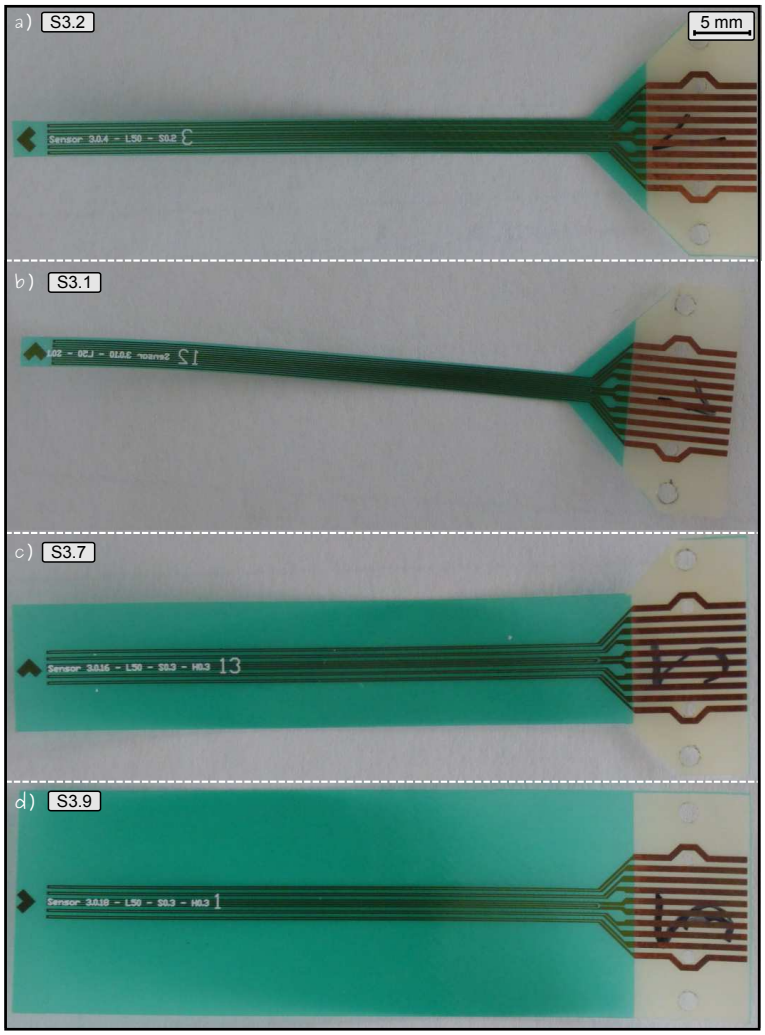

Figure 3.16: Photograph of the different sensors designs. Yellow represents the FR4 substrate, green the solder resist, brown the copper leads, and white the label. The first design (a - S3.2) has an increased gap, the second one (b - S3.1) shows the standard sensor, the third one (c - S3.7) has increased gap with holes between the leads and an increased wing, and the last one (d - S3.9) has an increased gap with holes between the leads and the maximum wing.

First of all, the most important change concerns the thickness of the leads. The PCB manufacturer is able to use a copper foil with $5 \pm 1.7\,\mu m$ instead of $9 \pm 2\,\mu m$ thickness on a $35\,\mu m$ carrier foil while the width remains the same. Thereby, the mean resistance values as well as the reproducibility of the leads will further increase.

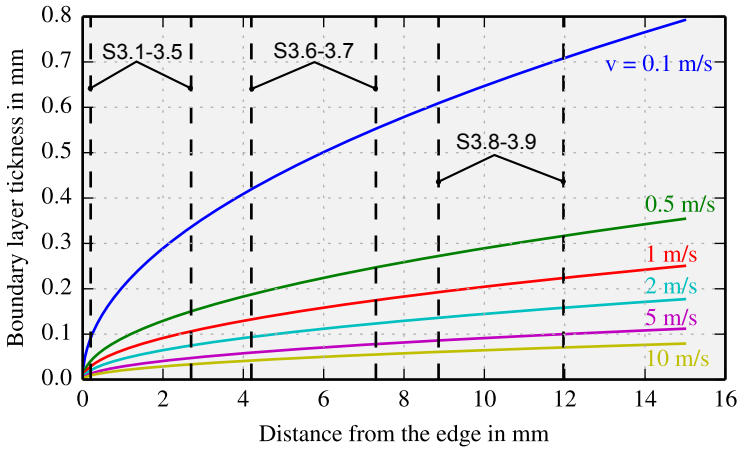

Figure 3.17: Evaluation of the boundary layer thickness for different flow velocities. The edges of the outer copper leads of the designs are marked with the vertical dashed lines (first pair...S3.1-3.5, second pair...S3.6-3.7, third pair...S3.8-3.9).

Another change regards the so-called wing w (Fig. 3.15 - Zoom) which is defined as the distance from the outer sensing leads to the edges of the substrate. The minimum wing amounts to 0.2 mm in the older designs. In contrast, the new designs feature wings of 4.2 and 8.86 mm. The first reason for increasing the wing is the tuning of the flow transduction by manipulation of the flow depended boundary layer [84].

A velocity boundary layer will develop along thin plates which are streamed lengthwise by a real fluid because, directly on the plate, the velocity is zero (non-slip condition). The evolving thickness of this boundary layer can be expressed as

$$\frac{\delta_{99}(x)}{l} = \frac{5}{\sqrt{Re_l}}\sqrt{\frac{x}{l}} \quad , \tag{3.17}$$

where $\delta_{99}(x)$ is the thickness of the boundary layer at a velocity of the outer flow of 99%, l is the length of the plate, Re_l is the Reynolds number related to the length of the plate, and x is the distance starting from the edge of the plate. Figure 3.17 depicts the boundary layer thickness as a function of the flow velocities for the different sensor designs.

A thermal boundary layer will develop similar to the velocity boundary layer when a heater is placed somewhere at a thin plate. These two boundary layers are linked where a rough estimation of their thickness can be made with the Prandtl number (Eq. 2.33). For the majority of gases under normal conditions the Prandtl number amounts $\sim$ 1.0 (for air: 0.7148 at 20°C) which means both velocity and thermal boundary layer have the same thickness [94].

The second reason for increasing the wing is a better mechanical stiffness of the sensor. From a mechanical point of view, the sensor is a doubly clamped beam with one degree of freedom (Fig. 3.15 z-direction) in the flow channel. When the flow becomes turbulent, vortices will induce vibrations of the sensor [95,96] but this effect can be countered by increasing the damping of the cantilever which depends

on material and geometrical parameters [97]. Therefore, an increase of the wing width will also increase the mass of the whole sensor proportionally.

Nevertheless, for small channels these effects become irrelevant because the PCB sensor length is short. But in HVAC systems big cross-sectional dimensions can occur which means the PCB length increases where this effect can cause problems. Within the laboratory setup such vibrations have not been observed while in a more realistic experiment (see Fig. 4.26) these vibrations were measured in high velocity regimes ($> 7\,\mathrm{m/s}$) when the sensor was not mounted with enough tension. These vibrations were recorded with a microphone and their spectrum was analyzed. The dominant frequency was found at 176 Hz.

After characterizing the second prototype design, the targeted sensor principle seems feasible. However, the measurable velocity range was limited to the experimental setup in the laboratory. Experiments in a realistic environment with a wider velocity range had to be carried out which means the sensor layout had to be adapted to the new dimensions. The next section explains this new layout.

Third Layout

The third prototype (Fig. 3.18) is designed for field tests in a realistic environment. In cooperation with the University of Applied Science Burgenland measurements in the "Energetikum" were performed. This facility is a living lab with sensors and actuators placed all over the building. There is permanent research parallel to the normal use of the building. The focus of this building lies on energy consumption research and building technology, and provides intelligent communication between electricity supplier, consumer, and energy storage operator. The HVAC system installed in the building is easy accessible and precisely monitored. The idea is to install the PCB sensor into the HVAC system and measure it via the monitoring system of the building.

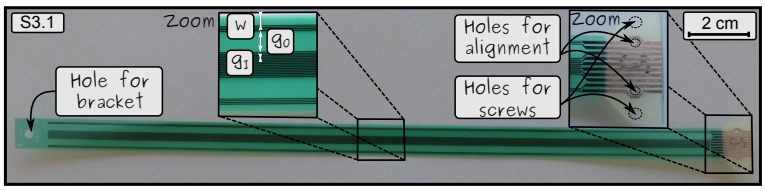

Figure 3.18: Picture of the third layout (S3.1). The left zoom section shows the copper leads in detail: g_I and g_O denote the gap between the inner and outer sensing leads, and w specifies the distance (wing width) between the outmost leads and the PCB edges. Whereas, the right zoom section shows the interconnection area of the sensor. On the left end there is a hole for a bracket to fasten the sensor to the pipe.

Therefore, the sensors must be redesigned in order to fit the pipes of the HVAC system of the Energetikum facility. The meander length l_M of the sensors is enlarged

to 250 mm, the inner gap g_{I} is set to 0.1 mm, the outer gap g_{O} is increased to 2.5 mm, and the wing w is decreased to 1 mm because of the increase of the outer gap (see zoom section in Fig. 3.18). Additionally, the order of meander loops is increased to four and eight for the sensing leads and heater, respectively. All other dimensions remain the same as in the second prototype. On the left end of the sensor a hole is drilled for a bracket to fasten the sensor to the measured flow channel.

3.5 Overview of the Designs

In Chap. 4 experiments and results are presented where different sensors were tested. Table 3.2 gives an overview of the investigated sensors and their geometrical parameters like meander length (l_{M}), inner and outer gap (g_{I} and g_{O}) , holes diameter (h_{d}) and gap (h_{d} and h_{g}), and wing (w). Sensor category S1 denotes the proof-of-concept design (PoC), S2, S3, S4 the first (1Pty), second (2Pty), and third prototype design (3Pty), respectively.

Sensor	**Design**	l_{M}	g_{I}	g_{O}	h_{d}	h_{g}	w
		mm	µm	µm	µm	µm	mm
S1	PoC	10, 15, 20, 30, 50, 60	100	100	-	-	0.55
S2.1	1 Pty	10, 30, 50	100	100	-	-	0.20
S2.2	1	10, 30, 50	200	200	-	-	0.20
S2.3	1	10, 30, 50	300	300	-	-	0.20
S2.4	1	10, 30, 50	300	300	100	100	0.20
S2.5	1	10, 30, 50	300	300	100	300	0.20
S2.6	1	10, 30, 50	300	300	-	-	4.20
S2.7	1	10, 30, 50	300	300	100	300	4.20
S3.1	2 Pty	50	100	100	-	-	0.20
S3.2	2	50	200	200	-	-	0.20
S3.3	2	50	300	300	-	-	0.20
S3.4	2	50	300	300	100	300	0.20
S3.5	2	50	300	300	100	100	0.20
S3.6	2	50	300	300	-	-	4.20
S3.7	2	50	300	300	100	300	4.20
S3.8	2	50	300	300	-	-	8.86
S3.9	2	50	300	300	100	300	8.86
S4	3 Pty	250	100	2500	-	-	1.00

Table 3.2: Orientation table of the different sensor designs and their geometrical parameters: l_{M}: meander length, g_{I}: inner gap, g_{O}: outer gap, h_{d}: holes diameter, h_{g}: holes gap, w: wing. The design column denotes the corresponding sensor design: PoC: proof-of-concept, 1 Pty: first prototype, 2 Pty: second prototype, 3 Pty: third prototype.

3.6 Summary of Chapter 3: Design and Manufacture

* An analytical model was developed to obtain a qualitative insight of thermal flow sensors. Several simplifications have been made to ease analytical treatment. The energy conversation was applied to an infinitesimal 3D slice to derive a differential equation of the model:

$$\left(\lambda_\mathrm{f}\frac{\delta}{2}+\lambda_\mathrm{s}h_\mathrm{s}\right)\frac{\partial^2\vartheta}{\partial x^2}-\rho cp\bar{v}\frac{\delta}{2}\cdot\frac{\partial\vartheta}{\partial x}-\lambda_\mathrm{f}\frac{1}{\delta}\vartheta=0 \quad .$$

The solution for the temperature field is

$$\vartheta(x)=\left\{\begin{array}{ll}\dfrac{P}{\lambda_\mathrm{s}\cdot A}\cdot\dfrac{1}{2\alpha_2}\,e^{\alpha_2 x}+T_\mathrm{amb} & , \quad -\infty<x\leq 0\\[2ex] \dfrac{P}{\lambda_\mathrm{s}\cdot A}\cdot\dfrac{1}{2\alpha_2}\,e^{-\alpha_2 x}+T_\mathrm{amb} & , \quad 0\leq x<\infty\end{array}\right\}$$

with the eigenvalues

$$\alpha_{1,2}=\frac{\bar{v}\delta\lambda_\mathrm{f}}{a(\lambda_\mathrm{f}\frac{\delta}{2}+\lambda_\mathrm{s}h_\mathrm{s})}\pm\sqrt{\left(\frac{\bar{v}\delta\lambda_\mathrm{f}}{a(\lambda_\mathrm{f}\frac{\delta}{2}+\lambda_\mathrm{s}h_\mathrm{s})}\right)^2+\frac{\lambda_\mathrm{f}\frac{1}{\delta}}{\lambda_\mathrm{f}\frac{\delta}{2}+\lambda_\mathrm{s}h_\mathrm{s}}} \quad .$$

The excess temperatures at the measurement locations are evaluated as a function of the mean velocity. The model provides a rough overview of the design influence on the sensor characteristic.

* A 2-D-FEM simulation with Comsol Multiphysics was developed where the conjugated heat transfer model was utilized. Thereby, the thermal behavior of the PCB sensor inside a flow channel was simulated for two different operation modes, constant heating and constant temperature. The simulations revealed moderate response times and sufficient excess temperatures which proved the usability as a flow sensor.
* Four sensor layouts were designed:

1. Proof-of-concept - Substrate material is a FR4 glass epoxy with a thickness of 100 µm. For the copper leads a one sided flexible copper laminate with an initial thickness of 18 µm was used. These leads were narrowed down to 9 µm with a additional etching step. On top there is a cover layer (Kapton solder resist) with a thickness of 40 µm. In this design one heating element is placed in the middle of four sensing elements, two positioned upstream and two downstream of the heater, with a width of 100 µm. The heater has a meander of order four while each sensing lead has a order of two with meander lengths of 10, 15, 20, 30, 50, or 60 mm.
2. First prototype (changes to 1.) - New copper laminate with a thickness of 9 µm was used. Bond pads are replaced with a contact area for a female connector to

simplify handling the sensor. An orientation mark was placed on the tip of the sensor to indicate the placement during fabrication. The gap between the leads was increased to 200 µm and 300 µm. Holes have been drilled in the substrate to decrease the parasitic heat conduction. The holes have 100 µm in diameter and 100 µm or 300 µm spacing between each other. Sensors with 10, 30, 50 mm meander length were manufactured.

3. Second prototype (changes to 2.) - Another new laminate was used with a thickness of 5 µm. The wing was enlarged from 0.2 to 4.2 and 8.86 mm. Sensors with 50 mm meander length were manufactured.
4. Third prototype (changes to 3.) - The third prototype was designed for field tests in a realistic environment. The meander length was increased to 250 mm and the order of the meanders was doubled, the heater to eight and the sensing leads to four. The inner gap is 0.1 mm, the outer gap is 2.5 mm, and the wing is 1 mm.

∗ At the end of this chapter an orientation table gives an overview of the produced designs.

Chapter 4

Experiments and Results

This section describes the experimental approach to characterize the sensor. The various measurement setups, the performed measurements as well as their results are discussed in detail. First, an experimental setup regarding resistance measurements is explained and evaluated. Afterwards, the precise evaluation of the reproducibility of low DC resistance of the copper leads is described, followed by the investigation of the velocity dependence with a lock-in amplifier and a circuit on which the leads are connected in a Wheatstone bridge configuration. Then, measurements in a constant temperature mode are explained and evaluated. Finally, experiments in a realistic environment are presented.

Instrumentation for numerous routine measurements should be computer controlled as much as possible. The programming language Python was chosen to control the instruments. It offers several benefits [98, 99] such as:

* Easy to understand and has multiple features to control hardware (e.q. multimeter, lock-in amplifier, etc.)
* Many implemented algebraic, numerical and graphical functions due to comprehensive scientific packages like NumPy or SciPy
* Ability to build numerical algorithms that are 10-fold faster than those generated by compiled languages
* Integrated debugging environment
* Huge user community
* Open-source software which allows implementation on all standard PC platforms (Linux, Mac OS X, Unix, Windows).

All in all, Python is an impressive software basis that satisfies all needs for the conducted experiments.

In order to control several instruments with Python with a PC, a specific hardware link and the corresponding communication protocol is needed. The IEEE-488 bus (GPIB [100]) was chosen because the lock-in amplifier used featured only this bus. Measurements typically produce megabytes or even gigabytes of data that have to be stored in a standard data format for easy post processing. This is one of the reason why HDF was used. Another reason is the option to store additional meta data of

measurements or the collected data. Moreover, the data does not need much storage space in comparison to excess or csv. However, the HDF package [99, 101, 102] by itself consists merely of a format definition and of associated libraries. Therefore, Python offers several Application Programming Interfaces (APIs) like Pandas, H5py or PyTables to work with HDF.

4.1 Resistance Measurements

Because the resistance of the copper leads is rather low, the instruments and interconnections are characterized to reveal their limits and uncertainties. Then the sheet resistance is introduced for a straightforward comparison of the various sensor designs and typical measurement results are presented. Finally, the transient resistance changes of the sensor components in response to excessive Joule heating are evaluated.

Equipment Characterization and Low Resistance Interconnection Studies

To characterize the measurement setup, the sensitivity and reproducibility were measured at low resistance values. A precision resistor (12 Ω) served as a sample and was repeatedly measured (10 Hz measuring rate for 10 min) with four different multimeters (Keithley 195a, Keithley 2000, Picotest M3500A, GWInstek GDM-8261A). The four wire measurement method was used in all cases. All in all, the highest deviation was 1.7 mΩ which correlates with the specified errors and confirms that all instruments are classified for the planned measurements.

To form a reliable connection between PCB flow sensor and measurement device soldering as interconnection was considered first. Consequently, the first experimental study was devoted to explore the contact resistances of various soldered interconnections. The copper wires to the multimeters were soldered on and off ten times from each bond pad of the proof-of-concept sensor (S1) and the total resistance of these circuits were measured with a high precision LCR meter (Agilent E4980A). It can be assumed that the resistivity differences due to soldering are small enough (worst case: $1.732 \pm 0.008\,\Omega$) to allow sufficiently efficient temperature transduction via small resistivity changes.

Unlike the proof-of-concept design, the prototype designs are connected to the environment via a female connector placed on an adapter board (Fig. 4.1). The female connector type is a low profile and elevated one piece FSI connector from Samtec. At the top there are two holes for screws and in the middle there are mechanical springs with gold coating. The sensor is placed upside down on these springs and fastened via a plate with screws to establish a low resistance interconnection with the adapter board. At the bottom of the adapter board there are several miniature test sockets for interconnection to the read out equipment.

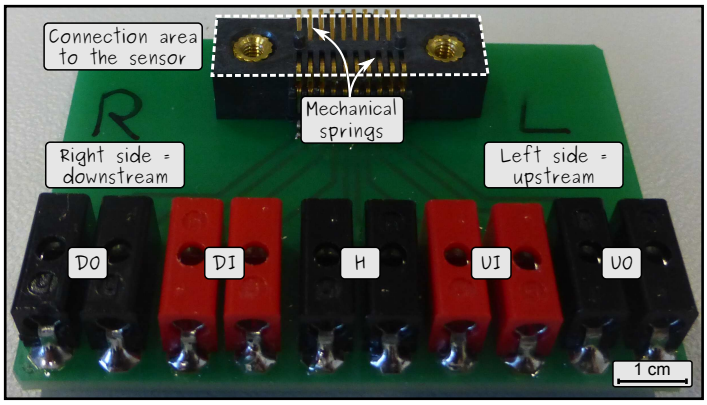

Figure 4.1: Photograph of the connector mounted on an adapter PCB board to connect the leads of the sensor with the readout equipment. The sensor is placed upside down on the connector which means left and right are swapped. There are holes for screws and mechanical springs for a low resistance interconnection. At the bottom there are miniature test sockets for connecting the read out equipment. For the subsequent measurements the right side is downstream and the left side is upstream.

The ohmic influence of this connector was compared with a soldered connection to see the differences between the two connection methods. Each lead of the sensor (S2.1) was accessed by measuring wires via the described connector and the resulting resistance was measured ten times. Afterwards, labor wires were soldered on and off ten times on the leads without the connector and measured. In both cases the four wire method was used with a standard deviation of std $= \pm 0.003$ of reading $+ 0.003$ of the multimeter [103]. Table 4.1 summarizes the resistance differences between the soldered interconnection and the adapter board. As expected, the connections with the board have slightly higher resistance values ($1.2-2.7\%$) than the soldered version but the resistance values of the adapter board are small enough to have no relevant influence on the sensor. Therefore, the more convenient connector based setup was preferred for all subsequent measurements.

Sheet Resistance

First, the resistance of each lead was measured to determine their reproducibility and, then, a statistical evaluation (median values, upper and lower quartiles, and the minimums and maximums) of all resistance values was made. Surprisingly, the precision of the leads is worse than the tolerances predicted by the specifications of the PCB producer. One reason for this is the small height of the leads where small etching rate variations have a relatively large influence. For a systematic comparison of the different leads, a parameter called sheet resistance [104] is most appropriate. This sheet resistance can be expressed as

$$R_{\mathrm{s}} = R\frac{w}{l} \quad , \tag{4.1}$$

Lead	Soldered	Connector
	Ω	Ω
Heater	7.093 ± 0.005	7.181 ± 0.003
DO (RO)	4.054 ± 0.003	4.147 ± 0.002
DI (RI)	3.929 ± 0.003	4.002 ± 0.003
UO (LO)	4.020 ± 0.002	4.094 ± 0.002
UI (LI)	4.259 ± 0.003	4.378 ± 0.004

Table 4.1: Measured DC resistances of the sensor leads for both connector and soldered interconnection. Ten measurements for each lead were carried out and then mean value and standard deviation were calculated (D...downstream, U...upstream, R...right, L...left, O...outer, I...inner).

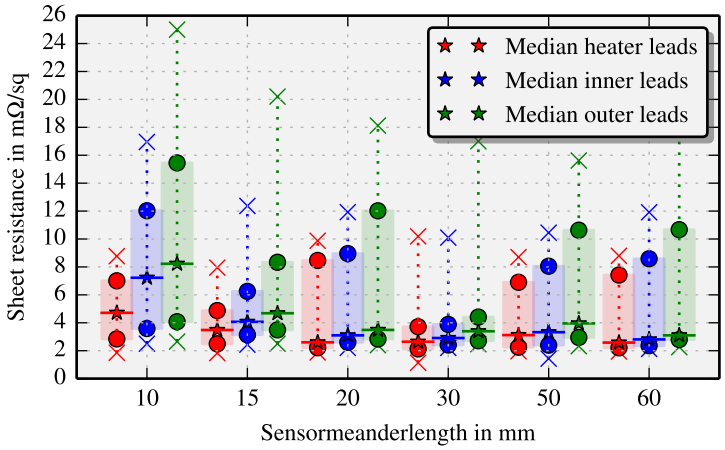

Figure 4.2: Nominal sheet resistance of the copper leads of the proof-of-concept designs (S1). For each meander length ($n_{\text{heater}} = 15$, $n_{\text{inner}} = n_{\text{outer}} = 30$) the median sheet resistance (stars with lines), the upper and lower quartile (dots), and the minimum and maximum (crosses) are shown. (colors: red...heater, blue...inner leads, and green...outer leads)

where R is the measured resistance of the lead, w and l are the width and length of the lead, respectively. This would require measuring these geometrical parameters (width and length) for each lead. However, the nominal width and length are added in Eq. 4.1 and the calculated parameter is called nominal sheet resistance in this thesis. Although there are errors with this method, it is feasible because these errors are small in comparison to others. Figure 4.2 depicts the results of this nominal sheet resistance for the proof-of-concept design where a distinction was made between the heater, inner, and outer sensing leads in addition to the meander length.

These results revealed that the computed median of the nominal sheet resistances

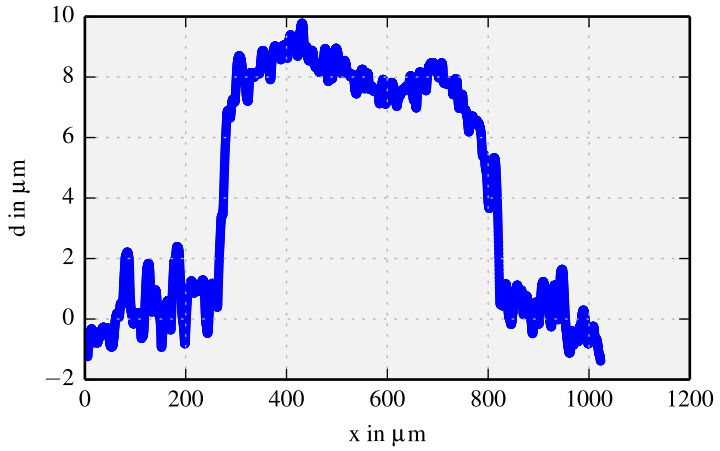

Figure 4.3: Sheet thickness measurement of a connection pad of the sensor (S2.5). The surface roughness was recorded over the width of the sensor. In the diagram the detail around a connection pad (300 to 800 µm at the $x-$abscissa) is plotted.

does not significantly depend on the length of the meander. However, the 10 mm sensors are the exception. One reason is that there were problems at the soldered connection. The other one is that the circular parts of the meander were not taken into account. The relative influence of these regions is larger for shorter meanders.

On the contrary, for the interquartile range (IQR) there are some differences. For the 15 and 30 mm sensors the IQR is very small which means the precision of these leads is very high. Moreover, the heater leads have the smallest median of the nominal sheet resistance with the smallest IQR while the outer sensing leads have the highest median with the highest IQR. According to this finding, leads which are surrounded by further copper areas are more uniform than the ones neighbored by large substrate areas. Thus, the etch rates seem to be different in both cases. To improve the uniformity of the etch rate, sacrificial copper areas may be added outside to the sensor structures to improve the precision lead resistances.

What is actually the precision of a single lead? To answer this question, the sensor's topology was scanned with a contact profilometer (Dektak Stylus). The radius of the tip was 5 µm and the bearing-strength was specified as equivalent mass with $5-10$ mg. To get the lead height a region without solder resist is required. Therefore, the connection pads were investigated and Fig. 4.3 depicts the surface roughness over the width of a connection pad. The resulting mean thickness is 8.0 ± 0.7 µm which is even better than the producer specified. Nevertheless, according to the manufacturer this may not be related for the smaller leads because a pad is larger and detached from other structures. As a result, the roughness due to the etching of a lead surface is worse than the measured one from a connection pad. Unfortunately, this statement could not be verified with measurements.

Another question is the difference between left and right side leads. Therefore, for each sensor, left and right, inner and outer sensing leads were compared to each other. Thereby, the resistance difference ($\triangle r$) between two leads related to their

mean resistance can be expressed as

$$\triangle r = \frac{R_{\text{left}} - R_{\text{right}}}{\frac{R_{\text{left}}+R_{\text{right}}}{2}} \quad , \tag{4.2}$$

where R_{left} and R_{right} is the resistance of the left and right sensing lead, respectively. Figure 4.4 depicts $\triangle r_{\text{i}}$ (inner leads) versus $\triangle r_{\text{o}}$ (outer leads). The meander lengths are highlighted with different colors to reveal any length related pattern, but none could be revealed.

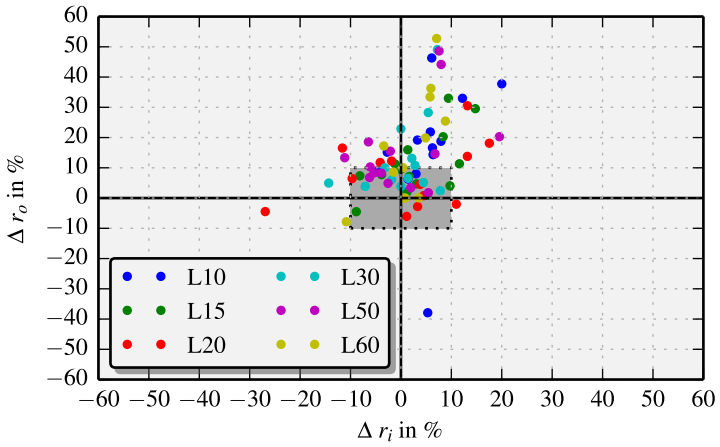

Figure 4.4: Normalized resistance differences of the sensing leads $\triangle r_{\text{i}}$ (inner leads) versus $\triangle r_{\text{o}}$ (outer leads) in percent of the proof-of-concept design (S1). Additionally, a distinction between the meander lengths was created (colors) to reveal any length related pattern. A positive value means the left lead is higher and a negative determines the right one is higher. The gray rectangle shows a section to compare with other produced designs and will be explained in detail later.

For the calculated $\triangle r_{\text{i}}$ no pattern could be revealed either. However, $\triangle r_{\text{o}}$ shows a strong tendency to the left side. The manufacturer stated that the etching rate of the additional etching step may not be homogeneous over the whole substrate and due to etchant streaming the etching process can exhibit a preferred direction. Moreover, the outer sensing leads act as etchant buffer for the inner leads leading to a smaller surface roughness and slightly increases lead thickness of the inner ones. This was verified with the nominal sheet resistance measurements (see Fig. 4.3). According to the manufacturer, it is difficult to find optimal process parameters for such small lead resolution to achieve high etching uniformity over the entire processed PCB area.

The precision of the sensor quality has to be improved further for the targeted application. The main reason for the differences of the leads was attributed to the additional etching step used for thinning of the copper leads. An obvious idea is to completely avoid this step. This would decrease the sensor resistor by about 50% making a high-resolution readout more challenging. Another way would be to place

Length	**Lead**	**Proof-of-Concept**		**1.Prototype**	
		Median	**IQR**	**Median**	**IQR**
mm		mΩ/sq	mΩ/sq	mΩ/sq	mΩ/sq
10	Heater	7.71	4.16	3.82	0.25
	Inner sense	7.23	8.44	4.78	0.37
	Outer sense	8.23	11.38	5.31	0.53
30	Heater	2.64	1.59	3.53	0.46
	Inner sense	2.91	1.48	3.96	0.63
	Outer sense	3.39	1.70	4.39	0.52
50	Heater	3.12	4.65	4.10	0.78
	Inner sense	3.33	5.66	4.64	1.30
	Outer sense	3.96	7.68	4.89	0.95

Table 4.2: Comparison of the nominal sheet resistance (S1 - S2.7) with the median and interquartile range between the proof-of-concept and the first prototype. Additionally, the results are classified according to meander length as well as the heater, inner sensing, and outer sensing function.

sacrificial areas near the outer sensing leads or optimize the process parameters for the etching step. In the meantime, new, thinner copper foils for the PCB technology became available which allow the production of thinner leads, thus eliminating the need for the critical etching step.

The lead resistances of the first prototype design were measured the same way as the leads of the proof-of-concept devices. Afterwards, the nominal sheet resistance was calculated and compared with the proof-of-concept results. Table 4.2 summarizes these results in which the reproducibility of the leads increased dramatically (IQR decreases).

Moreover, the precision of the copper leads of the second prototype design improved further due to use of thinner copper foils. Figure 4.5 compares the nominal sheet resistance of three designs (proof-of-concept, first prototype, and second prototype). In numbers, the median nominal sheet resistances for the leads of the second prototype are: 3.36 (IQR = 0.08) mΩ/sq for the heater leads, 3.54 (IQR = 0.11) mΩ/sq for the inner sensing leads, and 3.58 (IQR = 0.08) mΩ/sq for the outer sensing leads which is an improvement factor of ten.

Next, $\triangle$R was calculated for the new designs to reveal the impact of the thinner copper foils with higher precision. Therefore, Fig. 4.4 is updated with the first and second prototype sensing lead differences (Fig. 4.6). In detail, the proof-of-concept

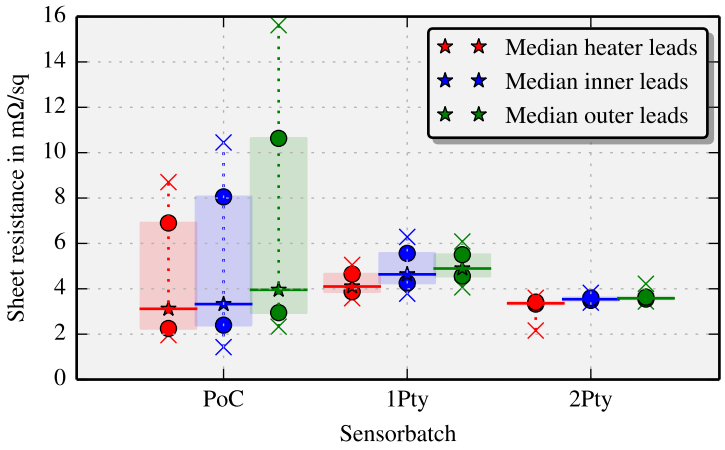

Figure 4.5: Nominal sheet resistance (S1 - S3.9) at proof-of-concept (PoC), the first (1Pty) and the second prototype (2Pty). Only meander lengths of 50 mm are depicted. For each sensor batch the median (stars), the upper and lower quartile (dots), and the minimum and maximum (crosses) are shown. (colors: red...heater, blue...inner leads, and green...outer leads)

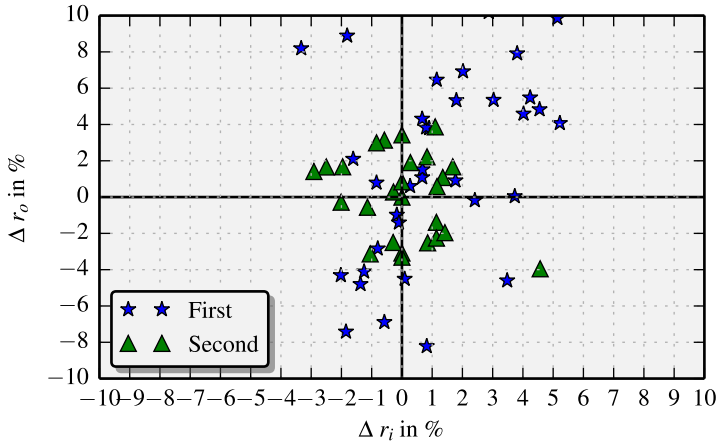

Figure 4.6: Normalized resistance differences at the sensing lead pairs (S2.1 - S3.9). The diagram range corresponds to the gray shaded area of Fig. 4.4 and contains the $\triangle r$ values of both the first and second prototype layout.

resistance differences are 20% (inner sensing leads) and up to 60% (outer) in relation to their mean value. However, the first prototype differences are 5% (inner) and 10% (outer) and less than 3% (inner) and 6% (outer) for the second prototype. Now, the lead precision seems to be sufficient for the desired thermal flow transduction. Furthermore, it is to be expected that this precision can improve further due to technological advances and gained experience. However, the current differences of the resistance between the leads will require a calibration of each individual sensor. Corresponding procedures and results can be found in [105].

Especially large PCB devices expose the weaknesses of the production process. The

field test sensors (S4.1) have much longer meanders (250 mm) leading to higher lead resistances. Twelve sensors have been produced whereby nine sensors are fully functional and, therefore, used for the measurements. Nine sensors are not sufficient for sound statistics evaluation and this must be kept in mind when reading the results. Nevertheless, the median for the heater is 8.4 (IQR = 3.3) mΩ/sq, for the inner sensing leads it is 8.0 (IQR = 2.5) mΩ/sq, and for the outer ones it is 9.1 (IQR = 5.1) mΩ/sq. These results revealed once more the large variations of the resistances. According to the producer, these variations are caused by the large size of the device which are close to the limits of the etching equipment. However, the sensor dimensions are pre-specified by the targeted pipe diameter of the test channel. To reduce the IQR, a larger etching equipment would be required as well as optimal process parameters. Nevertheless, the focus of the field test is to characterize the sensors in a realistic environment where the resistance variation of the sensors is of minor importance.

Transient Characteristics

Heating and cooling cycles are applied to the heater lead of the sensors (S1) to determine their transient behavior. A typical cycle is depicted in Fig. 4.7 where after an idle period of 5 s (heating time t_h) a heating power of 100 mW is applied for 30 s (cooling time t_c). The subsequent temperature relaxation is recorded for 10 s. The parameters delay time t_d, rise time t_r, on time t_ON, storage time t_s, fall

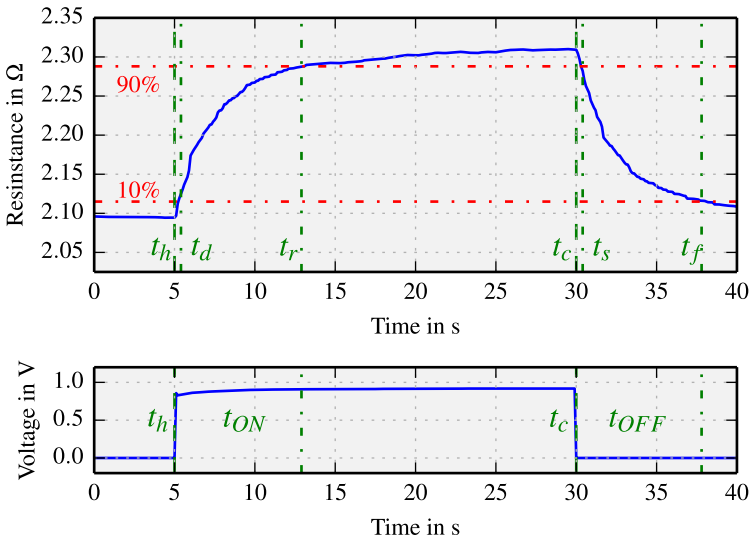

Figure 4.7: Resistance change during one heating and cooling phase for a proof-of-concept heater lead (S1). The heating power (100 mW) is enabled at $t_\mathrm{h} = 5$ s and switched off at $t_\mathrm{c} = 30$ s. Two horizontal lines (red dot-dashed) mark the 10% and 90% thresholds of the resistance change. The vertical lines (green dot-dashed) represent the characteristic time parameters: delay time t_d, rise time t_r, on time t_ON, storage time t_s, fall time t_f, and off time t_OFF.

Heating power	**Delay time**	**Rise time**	**On time**	**Storage time**	**Fall time**	**Off time**
mW	s	s	s	s	s	s
200	0.44	9.1	9.5	0.42	8.5	8.9
	±0.03	±0.2	±0.2	±0.03	±0.2	±0.2
100	0.47	9.3	9.8	0.46	9.0	9.5
	±0.03	±0.2	±0.2	±0.04	±0.2	±0.3
50	0.43	9.7	10.1	0.42	9.7	10.1
	±0.03	±0.3	±0.3	±0.03	±0.2	±0.2
25	0.35	11.1	11.4	0.38	12.3	12.8
	±0.03	±0.3	±0.3	±0.03	±0.4	±0.4
12	0.26	16.6	16.9	0.28	16.7	17.0
	±0.04	±0.8	±0.8	±0.04	±0.7	±0.7
6	0.19	20.5	20.7	0.21	22.2	22.4
	±0.03	±0.9	±0.9	±0.04	±0.9	±0.9

Table 4.3: Transient parameters of the proof-of-concept sensors (S1) for different heating powers where the mean values with standard deviation are calculated.

time t_{f}, and off time t_{OFF} are derived from such transients [106]. For the current work, the delay time t_{d} elapses between the onset of heating and the time where the measured resistance change of 10% of its total change during the heating period. The rise time t_{r} covers the period of normalized resistance change from 10% to 90%. Accordingly, the sum of delay and rise time is termed on time t_{ON}, the period required to reach quasi saturation. Storage time t_{s} is defined as the period from turning off the heating power to the point where the normalized resistance change reaches 90% again while the fall time t_{f} covers the transition from 90% to 10% of the resistance change. The sum of storage and fall time is defined as off time t_{OFF}, which is required for a nearly complete cool down.

The transient behavior was then studied for different heating powers and the corresponding results are summarized in Tab. 4.3. These results reflect the dynamic behavior of the sensor at zero flow and are in good agreement with the corresponding simulation. Figure 4.8 depicts a comparison between the simulated temperature curve and the curve calculated from the measured resistance of a heater lead. These results validated the heat transfer model used for numerical simulations. The study delivered the period which is needed to reach thermal saturation for intermittent flow measurements.

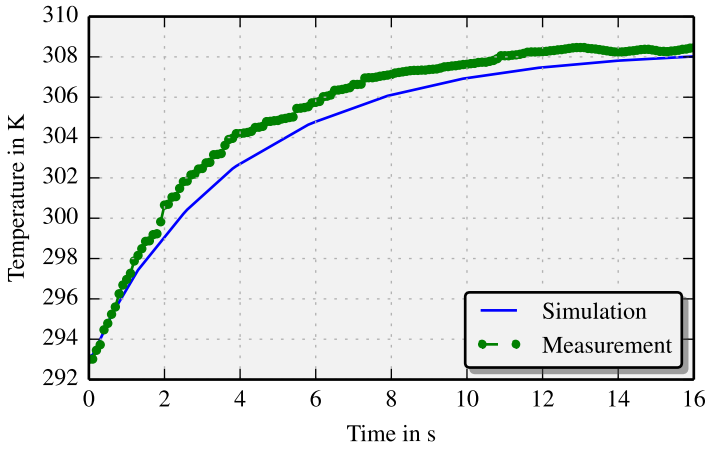

Figure 4.8: Comparison of the simulated and measured temperature change of the heater when a heating power of 100 mW is applied at zero flow. In this case, thermal saturation is reached after 16 s.

4.2 Lock-In Measurements

Lock-in amplifiers are used to detect and measure very small AC signals at a well-defined frequency [107]. They are needed to acquire tiny AC signals even when they are obscured by a huge noise level. In principle, the lock-in amplifier is a phase-sensitive detector in combination with large averaging time constants. This phase-sensitive detection (PSD) technique picks out the interesting spectral component at the specific reference frequency of any broadband signal. Employing two phase-sensitive detectors with the same reference frequency, but different phases, enables continuous phase estimation of the respective spectral component of the investigated signal. Therefore, lock-in measurements require a pure sinusoidal reference signal $V_{\mathrm{ref}} \cdot \sin(\omega_{\mathrm{ref}} t + \Theta_{\mathrm{ref}})$ that interacts with the spectral component of the amplified measured signal $V_{\mathrm{s}} \cdot \sin(\omega_{\mathrm{s}} t + \Theta_{\mathrm{s}})$. This signal is then multiplied by the reference signal. The output signal of the multiplicator V_{psd} is:

$$\begin{aligned} V_{\mathrm{psd}} &= V_{\mathrm{s}} V_{\mathrm{ref}} \cdot \sin(\omega_{\mathrm{s}} t + \Theta_{\mathrm{s}}) \cdot \sin(\omega_{\mathrm{ref}} t + \Theta_{\mathrm{ref}}) \\ &= \frac{1}{2} V_{\mathrm{s}} V_{\mathrm{ref}} \cdot \cos([\omega_{\mathrm{s}} - \omega_{\mathrm{ref}}]\, t + \Theta_{\mathrm{s}} - \Theta_{\mathrm{ref}}) \quad - \\ &\quad \frac{1}{2} V_{\mathrm{s}} V_{\mathrm{ref}} \cdot \cos([\omega_{\mathrm{s}} + \omega_{\mathrm{ref}}]\, t + \Theta_{\mathrm{s}} + \Theta_{\mathrm{ref}}) \quad , \end{aligned} \tag{4.3}$$

where V_{s} and V_{ref} are the amplitude of the measured and reference signal, ω_{s} and ω_{ref} are the angular frequencies, Θ_{s} and Θ_{ref} are zero phase angles, and t is the time. The output of the multiplier consists of two AC signals, one at the difference frequency $\omega_{\mathrm{s}} - \omega_{\mathrm{ref}}$ and the other at the sum frequency $\omega_{\mathrm{s}} + \omega_{\mathrm{ref}}$. This signal passes a low pass filter that suppresses AC components, leaving only spectral content in the vicinity of ω_{ref} left. Specifically, for $\omega_{\mathrm{s}} = \omega_{\mathrm{ref}}$, the filtered PSD output becomes

a DC signal which is proportional to the signal amplitude at ω_{ref}:

$$V_{\mathrm{psd}} = \frac{1}{2} V_{\mathrm{s}} V_{\mathrm{ref}} \cdot \cos(\Theta_{\mathrm{s}} - \Theta_{\mathrm{ref}}) \quad . \tag{4.4}$$

Now, if the measurement exhibits noise or uncorrelated interfering signals, the sequence of multiplier and low pass filter ensures that only signals whose frequencies are close to the reference frequency appear at the PSD output which is converted into a slowly varying DC voltage. Signal components at frequencies far from the reference are efficiently attenuated at the PSD output by the low pass filter. The attenuation depends on the bandwidth of the low pass filter. Therefore, the low pass filter determines the bandwidth of detection and only signals at the reference frequency will result in a true DC output. That's why lock-in amplifiers always need a reference signal that has the same frequency as the targeted signal. Lock-in amplifiers can generate the reference signal by themselves or they synchronize the internal reference oscillator to an external source that is correlated with the experiment. This task accomplishes a phase-locked-loop (PLL) that locks the internal reference oscillator to this external reference, resulting in a sine wave at $\omega_{\mathrm{s}} = \omega_{\mathrm{ref}}$ with a fixed phase shift of Θ_{ref}.

Most common lock-in amplifiers are dual-phase which means they have two PSDs allowing them to generate four alternative outputs. The first two ouputs represent the input signal as a position vector relative to the lock-in reference and are named X and Y. X is called 'in-phase' component and is defined as:

$$X = V_{\mathrm{s}} \cdot \cos(\Theta) \quad , \tag{4.5}$$

where $\Theta = (\Theta_{\mathrm{s}} - \Theta_{\mathrm{ref}})$ is the phase difference between the signal and the lock-in reference. Y is called 'quadrature' component and is generated from the second PSD via shifting the signal by 90°. Y can be expressed as:

$$Y = V_{\mathrm{s}} \cdot \sin(\Theta) \quad . \tag{4.6}$$

The other two outputs are the magnitude R and the phase Θ of the signal vector and are defined as:

$$R = \sqrt{X^2 + Y^2} \quad ; \quad \Theta = \tan^{-1}\left(\frac{Y}{X}\right) \quad .$$

Another important question about lock-in amplifiers is what they display on their outputs and in which unit. As a general rule, lock-in amplifiers display the signal in Volt RMS (Root Mean Square).

Experimental Setup

An experimental flow channel (Fig. 4.9) is used to characterize the behavior of the sensor (S1 - S2.7) at well-defined flow velocities. The flow channel consists of an acrylic glass pipe with a total length of 82 cm and an inner diameter of 5 cm where

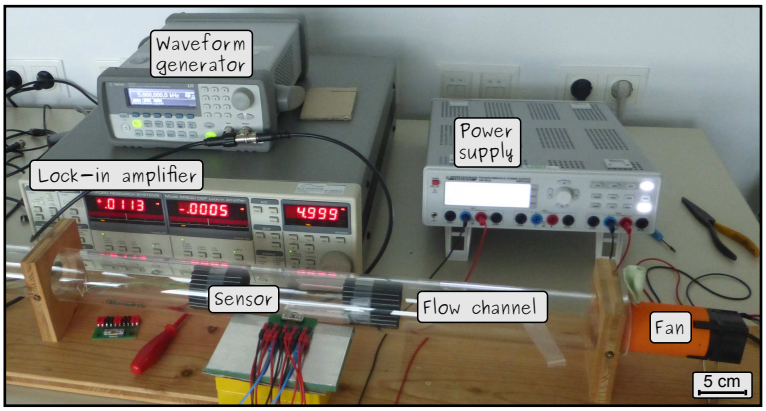

Figure 4.9: Photograph of the measurement setup to characterize the sensors. The device being tested is placed in the middle of a flow channel and supplied with a constant current (heater) as well as with an AC sinusoidal signal (sensing leads) from a waveform generator. Variable air flow rates are imposed by the suction with a fan positioned at one end of the tube. The four sensing leads form a Wheatstone bridge that is excited by the internal reference oscillator of the lock-in amplifier which measures also the bridge detuning voltage.

the sensor is stretched across this pipe via two slots. A double vane fan (AVC, 12 V DC) is located at the end of the pipe which establishes the flow by suction. The flow velocity inside the channel is adjusted by regulating the electrical current $I_{\mathrm{FAN}} = 50 - 300\,\mathrm{mA}$ of the fan with a power supply (Hameg HMP 2030) and the corresponding flow velocities are measured with an industrial anemometer (Testo 435 - hot wire probe). The anemometer was placed precisely in the middle of the flow channel and with the manufacturer specification table (correction factor) the anemometer velocity was converted into a mean flow velocity. Figure 4.10 displays the measured fan characteristic. As a result of this measurement, a parabolic fit to the fan characteristic was computed for simple conversion of flow measurement results:

$$v_{\mathrm{FLOW}} = -12.3\, I_{\mathrm{FAN}}^2 \frac{\mathrm{m/s}}{\mathrm{A}^2} + 16.8\, I_{\mathrm{FAN}} \frac{\mathrm{m/s}}{\mathrm{A}} - 0.5\,\mathrm{m/s} \quad , \tag{4.7}$$

where I_{FAN} is the supply current of the fan.

For the flow transduction experiments exploiting the lock-in measurement technique, the heater of the sensor was supplied with a constant current to regulate the injected heating power. The four sensing leads were connected to a Wheatstone bridge to avoid large bias signals at the lock-in input terminals enabling a higher signal gain. The bridge was supplied by a waveform generator (Agilent 33220) with a 5 V sinusoidal at 5 kHz. A resistor of 1 kΩ was inserted in series with the bridge which determines the AC current through the bridge and guarantees negligible self heating of the sensing leads. An SR830 Stanford Research Systems lock-in amplifier with Digital Signal Processing techniques was used to perform phase sensitive detection. The internal reference oscillator locks to the trigger output of the waveform generator.

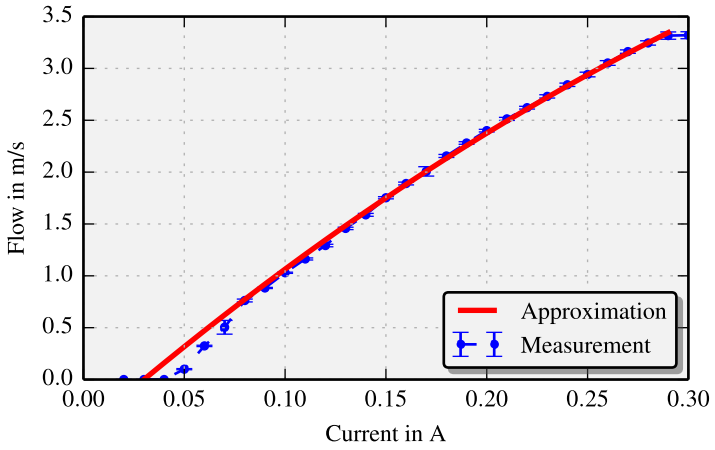

Figure 4.10: Measured and approximated flow velocity in the flow channel as a function of the fan current. The fan starts to rotate at 50 mA (0 m/s) and reaches its saturation at 300 mA (3.4 m/s). A parabolic approximation to the experiment was derived (red). Below 0.5 m/s the approximation does not fit the measurement resulting in a error. One reason for the kink in the measured data is, that at these current levels the fan does not rotate smoothly.

Reynolds Number

After identifying the feasible flow velocity range, the related Reynolds number range (see Sec. 2.1) can be evaluated. With Eq. 2.21, the physical parameters of the fluid ($\rho = 1.205\,\mathrm{kg/m^3}(20°\mathrm{C})$, $\eta = 19.83\,\mu\mathrm{Pa}$), and the diameter of the flow channel ($L = 0.05\,\mathrm{m}$), Reynolds numbers can be calculated for this flow arrangement. Up to a Reynolds number of $Re = 2300$, corresponding to a mean flow velocity of 0.76 m/s over the flow channel cross-section, the flow in a sufficiently long circular channel is laminar. For $Re > 4000$ turbulent flow results in the flow channel.

However, to extend the flow range with a stable flow velocity profile around the flow sensor position, flow collimators were inserted before and after it. The collimators are tubes of length 70 mm that exhibit a diameter of 5 mm each. Around 100 pieces are oriented in parallel and fill the entire cross-section of the flow channel. These incorporations decrease the apparent Reynolds number by a factor of ten. Therefore, the threshold velocity for the onset of turbulences increases up to 7.57 m/s. At least, it can be assumed that the flow is laminar in the measurement range with the given setup. Moreover, the collimators induce a rather uniform flow velocity distribution compared to the parabolic velocity profile that would evolve in the flow tube without collimators.

Preliminary Measurements

Bridge Imperfection

Due to the resistance mismatch of the copper leads, the bridge is detuned causing an offset even without any flow. To counter this effect, an offset compensation is required to measure very small relative deviations caused by the introduced flow. The SR830 lock-in amplifier has the option to remove such an offset signal manually or automatically. The auto offset automatically adjusts the signal offset to zero with the start of actual flow measurements. Nevertheless, tracking the offset values is important because it will reveal the drift of the bridge mismatch. In Fig. 4.11 the measured X (in-phase) and Y (quadrature) signals are shown as a function of the bridge supply voltage in a range from $V_{\text{Bridge}} = 5 - 10\,\text{V}$. Additionally, two linear regression lines are derived from these data points. As expected, the offset voltage increases linearly with increasing bridge supply voltage.

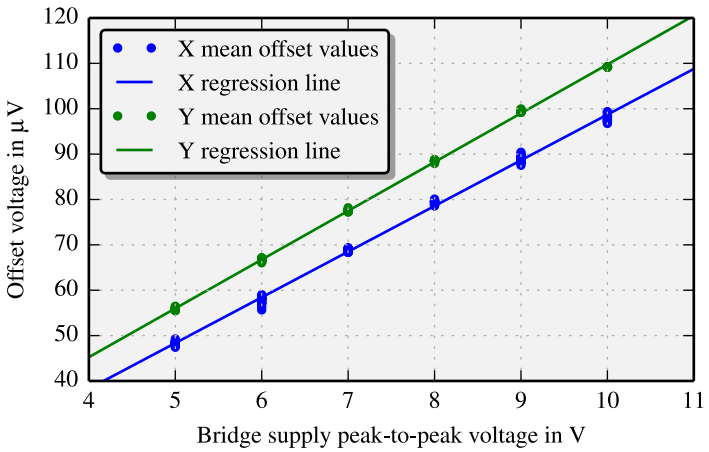

Figure 4.11: X (in-phase) and Y (quadrature) mean offset voltages over the bridge supply voltage in a range from $V_{\text{Bridge}} = 5-10\,\text{V}$ at zero flow velocity (S1). Additionally, for X and Y a linear regression line is shown with $X_{\text{Regression}} = 10.07 \cdot V_{\text{Bridge}} - 1.99$ and $Y_{\text{Regression}} = 10.75 \cdot V_{\text{Bridge}} + 2.24$.

Another interesting question is if the offset voltage changes with time or flow velocity (without heating). Therefore, in advance of each lock-in flow transduction measurement (see Sec. 4.2) both offset values were recorded prior to the turning-on of the heating but with the sensing lead bridge already supplied. Figure 4.12 depicts the corresponding offset voltages. The offset measurement was performed for several sensor designs (S2.1 - S2.7) and the results are summarized in Tab. 4.4. The measurements show no drift or flow velocity dependence of the offset voltage. This means, the self heating of the sensing leads caused by the supply of the Wheatstone bridge is small enough. Moreover, compensating the offset voltage before each flow transduction experiment allows measuring small voltages changes caused by the heating with sufficient accuracy.

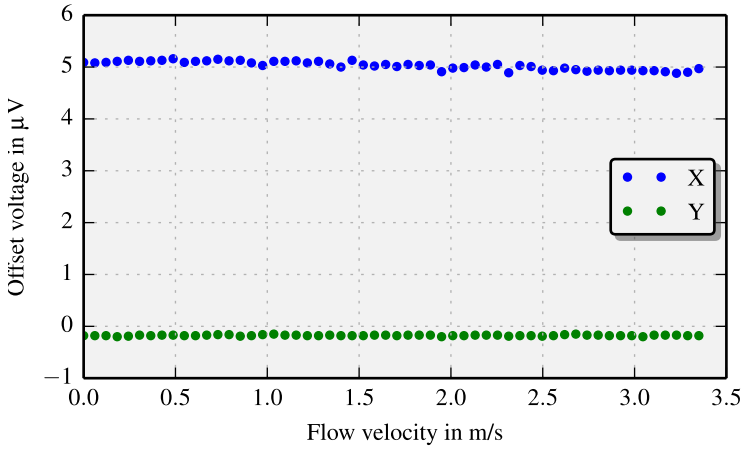

Figure 4.12: Offset voltages (X and Y) as a function of the flow velocity. The sensing lead bridge (S2.1) is supplied but without heating.

Sensor number	***X*** µV	***Y*** µV
S2.1	5.03 ± 0.08	-0.18 ± 0.01
S2.2	-36.85 ± 0.07	-1.03 ± 0.08
S2.3	91.2 ± 0.20	-2.1 ± 0.10
S2.4	-58.7 ± 0.40	-0.54 ± 0.05
S2.5	17.2 ± 0.30	-1.7 ± 0.10
S2.6	-48.7 ± 0.10	-0.44 ± 0.03
S2.7	56.5 ± 0.80	-0.55 ± 0.05

Table 4.4: Mean Offset voltages (X and Y) and the deviation of the lock-in for typical instances of different sensors types (S2.1 - S2.7). For each sensor 56 measurements were performed.

Bridge Voltage

After measuring and compensating the offset voltages of the lock-in amplifier, transients of the bridge detuning voltage are recorded in response to pulses of the heating power for different flow velocities. Figure 4.13 depicts a typical result where only the in-phase signal (X) changes with the onset of heating power at $t = t_{\mathrm{ON}} = 10\,\mathrm{s}$. In detail, the bridge detuning voltage raises to 82 µV and reverts back to zero after turning off heating ($t = t_{\mathrm{OFF}} = 70\,\mathrm{s}$). As expected, the quadrature signal (Y) with respect to the bridge supply signal remains zero during the whole measurement confirming that all elements of the Wheatstone bridge are pure resistive at the applied frequency of 5 kHz. Therefore, only the in-phase signal is considered further on.

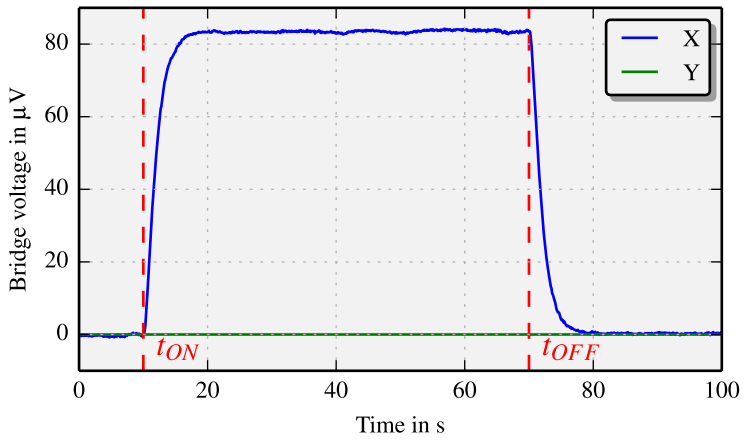

Figure 4.13: Typical bridge detuning voltage of a lock-in measurement (S2.1). Both X and Y components have been recorded at a flow velocity of 1 m/s and a heating power of 100 mW. The heating is turned on at 10 s and turned off at 70 s.

To gain the flow characteristic, the saturated in-phase signal was recorded for each instance of a set of fan currents starting from $I_{\mathrm{FAN}} = 30 - 300\,\mathrm{mA}$ with an increment of $\Delta I = 5\,\mathrm{mA}$. The current levels are converted into the corresponding flow velocities using Eq. 4.7. Finally, the bridge detuning voltage is plotted versus the flow velocity yielding Fig. 4.14, for example. The shown characteristic is typical for the transduction behavior of calorimetric sensors. As can be seen, the maximum in-phase signal change for the sensor type (S2.1) is 95 µV at 0.47 m/s in response to the applied heating power. Two sensitivities are extracted from the slope of the conversion characteristic. The first one amounts 399 µV/m/s and applies to the flow regime between 0.16 and 0.39 m/s while the mean value for the decreasing region is −9.7 µV/m/s in the flow regime taken between 0.55 and 3.44 m/s.

Subsequently, the heating power was typically halved after each experiment to estimate the minimal power for flow measurements with a sensitivity higher than 0.1 µV/m/s. Figure 4.15 depicts the related results. These series of measurements were terminated at a heating power of 1 mW because of the insufficient signal to noise ratio. For each heating power value the maximum bridge detuning voltage,

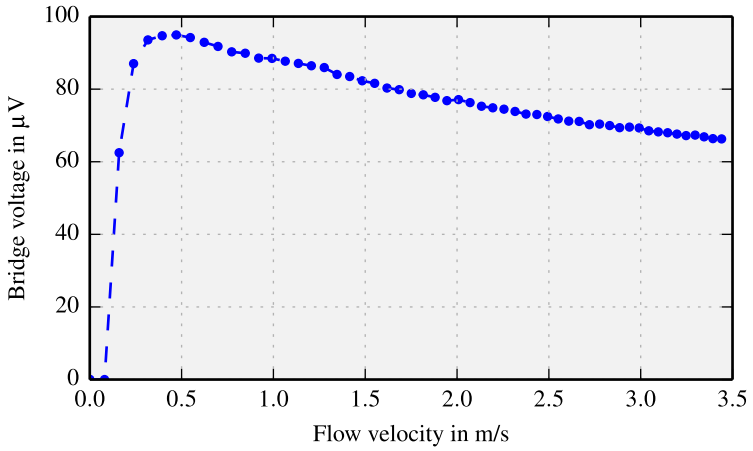

Figure 4.14: Characteristic of the sensor type S2.1 which is typical for the calorimetric principle. 56 measurements at different flow velocities were performed with a constant heating power of 100 mW. The bridge detuning voltage after saturation of each transient is plotted versus the mean flow velocity.

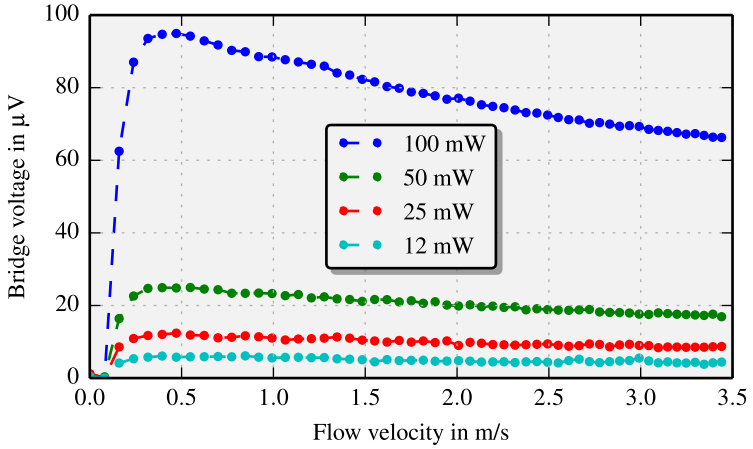

Figure 4.15: Characteristics of the sensor type S2.1 for different heating powers.

the corresponding flow velocity where the maximum bridge voltage was noted, and two mean sensitivities are presented in Tab. 4.5. At the maximum characteristic the sensitivity of the sensor is zero. However, there is a small low-flow regime of very high sensitivity while after the maximum the sensitivity is negative, its magnitude drops with increasing flow rate, but it remains the same over wide range. Even with 3 mW heating power the lock-in amplifier measurements provide a small but exploitable signal.

With a further study, the influence of layout variations like lead gap distance, substrate perforations between neighboring leads, or wing widths was explored. Each sensor type was measured with the previous setup using 100 mW DC heating power.

Figure 4.16 depicts three flow transduction characteristics where only the gap between the leads was 100, 200, and 300 µm. This variation leads to different temper-

P_{H}	$\bar{S}_1$	Range for $\bar{S}_1$	$V_{\mathrm{Bdg,max}}$ ($v_{\mathrm{Bdg,max}}$)	$\bar{S}_2$	Range for $\bar{S}_2$
mW	µV/m/s	m/s	µV (m/s)	µV/m/s	m/s
100	399.0	$0-0.47$	94.9 (0.47)	-9.7	$0.47-3.5$
50	78.9	$0-0.55$	25.0 (0.55)	-7.6	$0.55-3.5$
25	49.6	$0-0.55$	12.4 (0.55)	-1.1	$0.55-3.5$
12	9.7	$0-0.85$	6.1 (0.85)	-0.5	$0.85-3.5$
6	6.4	$0-0.70$	3.6 (0.70)	-0.2	$0.70-3.5$
3	6.0	$0-0.47$	1.7 (0.47)	-0.1	$0.47-3.5$
1	x	x	x	x	x

Table 4.5: Bridge voltage maximum $V_{\mathrm{Bdg,max}}$ with respect to flow velocity variations for different magnitudes of the heating pulse (P_{H}). The corresponding sensitivities $\bar{S}_1$ and $\bar{S}_2$ of the sensor S2.1 are given as well as their flow range.

atures of the sensing leads because the developed temperature profile at the sensor's surface remains nearly unchanged. If the gap is small then the temperature difference between the individual sensing leads is not the highest possible which results in a smaller bridge voltage but an increase of the measurement range. By increasing the gap the flow dependent temperature difference becomes higher as does the bridge voltage but saturation is reached faster. Comparing the bridge voltage maxima reveals that the design S2.2 does have a 12.5% higher and S2.3 a 33.2% higher maximum than design S2.1. An increase of the distance between neighboring leads beyond 300 µm promises further increase of the maximum signal. However, at some point, the gap is getting too large and the heat influence drops. Therefore, the bridge voltage will decrease. More details are summarized in Tab. 4.6.

Another comparison is depicted in Fig. 4.17. As explained in Sec. 3.4 there could be excessive heat conduction through the substrate and, to counter this effect, perforations in form of linear hole arrays have been drilled between neighboring copper leads. As anticipated, the output voltage increases for the perforated sensors since air inside drilled holes has lower thermal conductivity (0.026 W/mK) than the removed substrate (0.3 W/mK). Less thermal conduction along the PCB causes higher temperatures around the heater under the same environmental conditions. For all three designs the gap between neighboring leads of 300 µm, S2.3 does not have any holes. Design S2.4 has holes with a diameter of 100 µm and a distance between them is 100 µm resulting in a 40.12% higher bridge voltage maximum. The distance between the holes of S2.5 is 300 µm whereas the hole diameter remains the same. As a result, the transduction behavior is worse than in S2.4 but better than in S2.3 (see also Tab. 4.6).

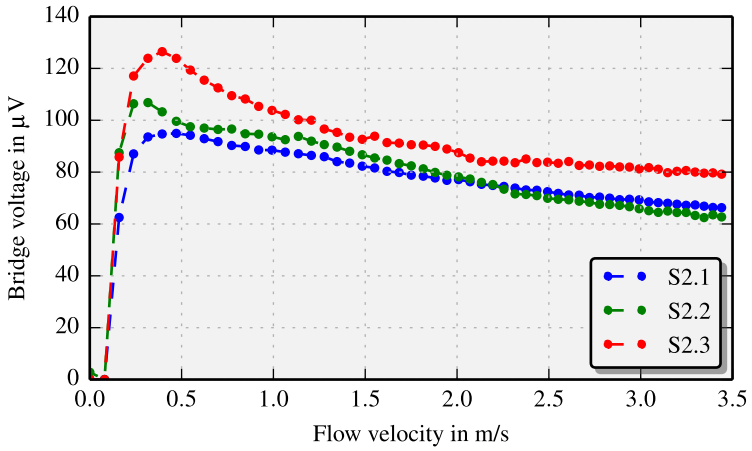

Figure 4.16: Influence of the gap distance on the sensor characteristic. S2.1 has 100 µm, S2.2 has 200 µm, and S2.3 has 300 µm gap distance.

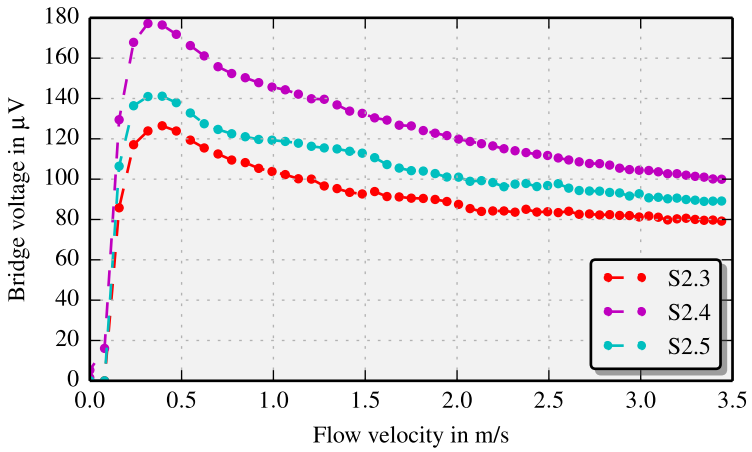

Figure 4.17: Influences of perforate substrates on the sensor characteristic. S2.3 has a gap distance of 300 µm without perforation. S2.4 has a straight line of holes with a diameter of 100 µm and a distance between the holes of 100 µm. S2.5 has holes with a diameter of 100 µm and a distance between the holes of 300 µm.

The last comparison (Fig. 4.18) illustrates the influence of the wing width of the PCB substrate. The sensors S2.3 and S2.5 have a wing width of 200 µm. S2.7 has the same hole placement and diameter as S2.5 but the wing width is enlarged to 4.2 mm. The maximum bridge voltage for S2.7 is 25.5% higher (177 µV) than the value measured for S2.5.

Table 4.6 summarizes the transduction characteristics of six different design variants (see Tab. 3.2). The maximum bridge voltage, two mean sensitivities, and their corresponding flow velocities are presented and they give an overview how design variations can improve the sensor characteristics. The next goal was to adapt the simulation models to cover the more complex designs in order to gain reasonable agreement with related experiment results. With an updated model, the design of

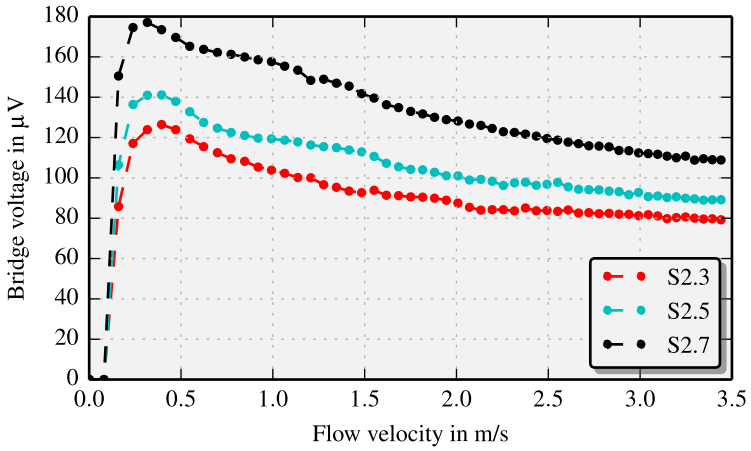

Figure 4.18: Influences of perforate substrates as well as the wing width on the sensor characteristic. S2.3 have the increased gap distance of 300 µm (same as S2.5 and S2.7) without holes and a wing width of 200 µm. S2.5 have holes with a diameter of 100 µm and a distance between the holes of 300 µm, and a wing width of 200 µm. S2.7 have holes with a diameter of 100 µm and a distance between the holes of 300 µm, and an increased wing width of 4.2 mm.

Sensor	$\bar{S}_1$	**Range for** $\bar{S}_1$	$V_{\mathrm{Bdg,max}}$ $(v_{\mathrm{Bdg,max}})$	$\bar{S}_2$	**Range for** $\bar{S}_2$
	µV/m/s	m/s	µV (m/s)	µV/m/s	m/s
S2.1	399	0 – 0.39	95(0.47)	−10	0.55 – 3.5
S2.2	1111	0 – 0.24	107(0.32)	−13	0.39 – 3.5
S2.3	746	0 – 0.32	127(0.39)	−15	0.47 – 3.5
S2.4	1440	0 – 0.24	177(0.32)	−25	0.39 – 3.5
S2.5	869	0 – 0.32	141(0.39)	−16	0.47 – 3.5
S2.7	1911	0 – 0.24	177(0.32)	−21	0.70 – 3.5

Table 4.6: Transduction measurement results for different designs of the prototype series (S2.1 - S2.7). The bridge voltage maximum and mean sensitivities are listed along with the corresponding flow velocity ranges.

improved sensors for the targeted pipe and environment will become much easier.

The lock-in measurements confirm the fundamental curve of the constant current mode. The temperature difference (up- and downstream around the heater caused by the imposed current), starting from zero flow, increases with the flow velocity because the upstream side is cooled more efficiently than the one downstream. Above a certain velocity threshold $v_{\mathrm{Bdg,max}}$, indicated by the bridge voltage maxi-

mum $V_{\mathrm{Bdg,max}}$, the overall cooling of the sensor lead to a general reduction of the local excess temperatures which outweighs the initial behavior. After this point, the temperature difference will decrease with increasing flow velocity resulting in a lower bridge voltage. This leads to the ambiguity for the interpretation of the measured signal in terms of flow velocity. For e.g. S2.1 a reading of 80 μV corresponds to two possible flow velocities: 0.25 and 1.6 m/s (see Fig. 4.14).

The basic idea is to overcome the ambiguity of the output signal by combining it with a threshold value which is gained from one or two sensing leads individually. In combination with the common velocity ranges of HVAC systems only the decreasing part (Range for $\bar{S}_2$) is used for determining the flow velocity. However, the sensitivity $\bar{S}_2$ is very small and thermal saturation is reached around 4 m/s. Therefore, several geometric parameters were varied to increase this sensitivity but regardless of how the parameters are adjusted, the measurable velocity range is still too small.

A main aim of this work is to develop flow sensors which can measure over a wider velocity range. This means, the calorimetric approach described above is not promising and another approach had to be pursued. Nevertheless, several of the results discussed so far have been already presented at scientific conferences and published in journals [108–110].

4.3 Constant Temperature Mode

This section explains the development of the evaluation electronics to use the sensor in a closed loop operation to enable a constant temperature (CT) mode. First, preliminary experiments with results are presented. Afterwards, electronics are designed which are needed to enable the CT mode and measurements with the electronics are performed. Finally, field tests at a partner university are carried out to test the new approach in higher velocity ranges and in a real environment.

Preliminary Experiments

Before the sensor was operated in the constant temperature mode, the potential of hot-film anemometry (Sec. 1.3) for the targeted HVAC application was considered. Therefore, only the heater voltage is measured where a constant heating power is applied at different flow velocities. In Fig. 4.19 the outcome of this hot-film anemometry in constant current mode is presented. In a nutshell, this mode is also not usable for the targeted application in HVAC systems because the sensitivity of the signal above 3 m/s is to small and the signal depends on the ambient temperature. Details of the measurement setup and more results can be found in this paper [111].

The constant temperature mode needs the ambient temperature for reference and control of the heat dissipation in the heating lead in order to work correctly. However, inserting an ambient temperature sensing element would require a completely altered sensor design. The actual sensor design, offers four temperature sensing leads

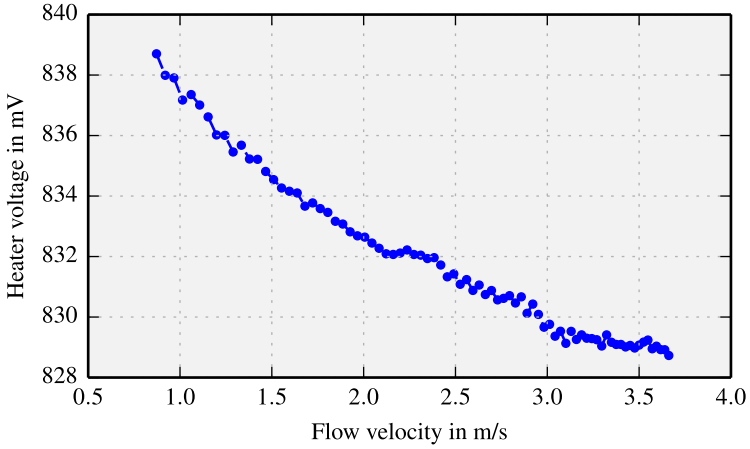

Figure 4.19: Constant current hot-film anemometry results. The heater voltage is depicted as a function of the mean flow velocity in the pipe with a constant heating current of $I_\mathrm{H} = 115\,\mathrm{mA}$ which corresponds to a heating power of 100 mW.

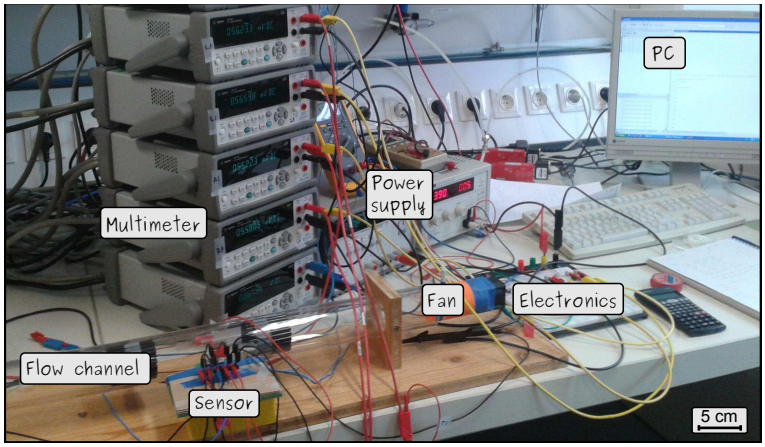

Figure 4.20: Photograph of the experimental setup for preliminary measurements for the constant temperature mode. The sensor was placed in the middle of the flow channel and supplied with a constant current ($I_\mathrm{H} = 115\,\mathrm{mA}$). A flow was induced with a fan and each sensing lead is measured individually. To keep the self-heating of the sensing leads sufficiently low, they are each supplied with a low constant current of $I_0 = 10\,\mathrm{mA}$.

for flow transduction. Initially, these sensing leads are supplied with a constant current of $I_0 = 10\,\mathrm{mA}$, to keep the self-heating sufficiently low. The sensor is measured in an experimental flow channel (Fig. 4.20) which is similar to the setup described above (see Fig. 4.9). Instead of the Wheatstone bridge configuration, seven multimeters are employed to measure each of the four sensing lead voltages individually, the temperature around the sensor, the heater voltage, and the fan current. The mean flow velocity range changed slightly in the new setup ($\bar{v} = 0.9 - 3.66\,\mathrm{m/s}$) because a different fan was used.

Figure 4.21 depicts results of this measurement where each sensing lead voltage

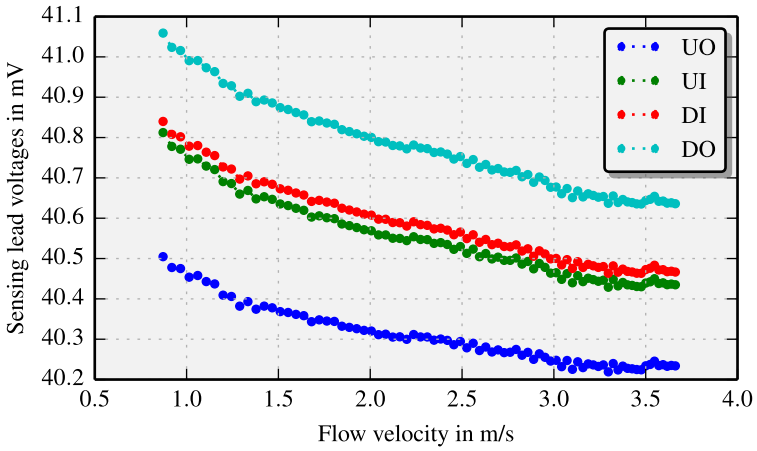

Figure 4.21: Voltages at the four sensing leads versus mean flow velocity of the sensor with constant heating power of 100 mW (leads: UO - upstream outer, UI - upstream inner, DI - downstream inner, DO - downstream outer).

is measured individually. Like the heater voltage in constant current mode (see Fig. 4.19), all sensing lead voltages decrease with increasing flow velocity when a constant heating power of 100 mW is dissipated at the heater.

Finally, three relevant signals are deduced from these four sensing lead voltages. The first one, U_1, is the sum of the upstream sensing lead voltages minus the sum of the downstream ones:

$$\begin{aligned} U_1 &= (U_{\mathrm{UO}} + U_{\mathrm{UI}}) - (U_{\mathrm{DO}} + U_{\mathrm{DI}}) \\ &\propto (T_{\mathrm{UO}} + T_{\mathrm{UI}}) - (T_{\mathrm{DO}} + T_{\mathrm{DI}}) \\ &\propto T_{\mathrm{U,mean}} - T_{\mathrm{D,mean}} \quad , \end{aligned} \tag{4.8}$$

where the indices indicate the position on PCB: U/D stands for up- and downstream and I/O for inner and outer position, U_{i} are the corresponding sensing lead voltages and T_{i} are the individual temperatures. $T_{\mathrm{U,mean}}$ and $T_{\mathrm{D,mean}}$ denote the mean temperature up- and downstream of the heater position. The second signal, U_2, is the sum of the inner sensing lead voltages minus the sum of the outer sensing lead voltages:

$$\begin{aligned} U_2 &= (U_{\mathrm{DI}} + U_{\mathrm{UI}}) - (U_{\mathrm{DO}} + U_{\mathrm{UO}}) \\ &\propto (T_{\mathrm{DI}} + T_{\mathrm{UI}}) - (T_{\mathrm{DO}} + T_{\mathrm{UO}}) \\ &\propto T_{\mathrm{I,mean}} - T_{\mathrm{O,mean}} \quad , \end{aligned} \tag{4.9}$$

where $T_{\mathrm{I,mean}}$ and $T_{\mathrm{O,mean}}$ denote the mean temperature of the inner and outer pair of the temperature sensing leads. The last signal, U_3, is the sum of all sensing lead

voltages:

$$\begin{aligned} U_3 &= U_{\mathrm{DI}} + U_{\mathrm{UI}} + U_{\mathrm{DO}} + U_{\mathrm{UO}} \\ &\propto T_{\mathrm{DI}} + T_{\mathrm{UI}} + T_{\mathrm{DO}} + T_{\mathrm{UO}} \\ &\propto T_{\mathrm{S,mean}} \quad , \end{aligned} \tag{4.10}$$

where $T_{\mathrm{S,mean}}$ denotes the mean temperature of all sensing leads of the PCB sensor. Figure 4.22 depicts the flow dependencies of these three signals. The signal U_3 represents the cooling of the PCB. It features the same trend as U_{H} in constant current mode which is not really useful, because it is ambient temperature dependent and it reaches thermal saturation above 3.5 m/s. U_1 is the mean temperature difference between upstream and downstream of the sensor. It is flow velocity dependent but it reaches saturation similar as U_3 and U_{H} in the constant current mode. Moreover, there is no ambient temperature sensing, therefore, it is not useful for a constant temperature mode but, unlike U_3 and U_{H}, this signal is flow direction dependent which is interesting for measuring the flow direction.

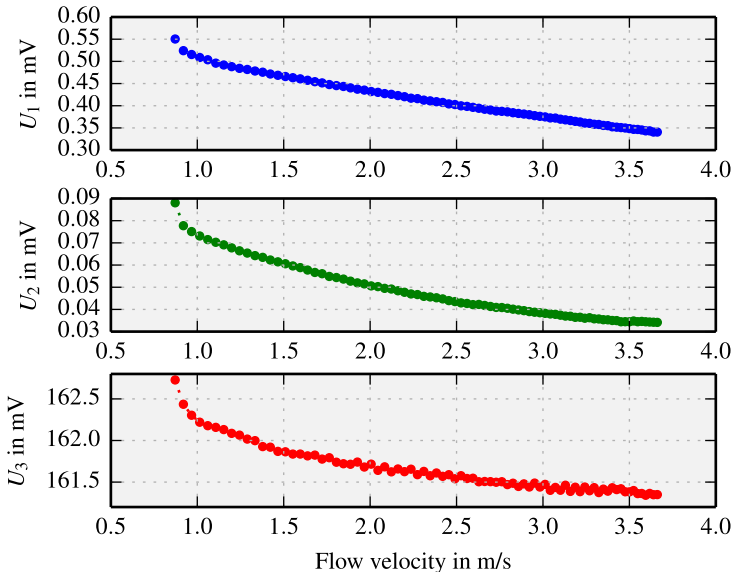

Figure 4.22: Three signals deduced from the four sensing lead voltages as a function of the mean flow velocity: $U_1 = (U_{\mathrm{UO}} + U_{\mathrm{UI}}) - (U_{\mathrm{DO}} + U_{\mathrm{DI}})$, $U_2 = (U_{\mathrm{DI}} + U_{\mathrm{UI}}) - (U_{\mathrm{DO}} + U_{\mathrm{UO}})$, $U_3 = U_{\mathrm{DI}} + U_{\mathrm{UI}} + U_{\mathrm{DO}} + U_{\mathrm{UO}}$.

Similar to U_1 is the signal U_2 which reaches saturation above 3.5 m/s in constant current mode. This signal describes the difference between the mean temperature at the middle of the sensor (measured with the inner sensing leads) and the mean temperature at the periphery of the PCB (measured by the outer sensing leads). At first glance, this signal does not seem usable since the temperature at the periphery of the PCB differs somewhat from the ambient temperature, therefore, a constant temperature mode does not seem feasible. However, when the distance between the heating lead and the outer sensing leads is large enough, the temperature of the

outer sensing leads almost reaches the ambient temperature depending on the flow velocity as well as the dissipated heating power. For the targeted application, this distance is around 3 mm.

Keeping the signal U_2 constant with an electronic controller results in a constant temperature difference between the mean temperature of the inner and outer part of the sensors ($T_{\mathrm{I,mean}} - T_{\mathrm{O,mean}} = \text{constant}$). With increasing flow velocity the electronic controller must increase the heater voltage to maintain this constant temperature difference which means the heater voltage can be used to determine the flow velocity. Above a certain velocity the temperature distribution will not change with increasing heating power causing the signal to saturate. However, this constant temperature mode promises a wider velocity range and, therefore, this approach is worth a detailed investigation.

Electronic Controller Design

The constant temperature approach has to be experimentally proven in the higher velocity ranges (up to 8 m/s). Therefore, an electronic circuit was developed which controls the heater voltage depending on the temperature difference signal U_2. This section describes the main parts of the circuit, its characteristic behavior, and its verification with measurements.

Since the signal U_2 should remain constant, each of its components must be measured individually and combined according to Eq. 4.9. To track the temperatures of the sensing leads, the minor voltages at the terminals of these low resistances (few Ohms) must be measured with sufficient precision (mΩ). Therefore, four constant current sources provide the sensing currents of 10 mA for each sensing lead. Next, four instances of a high accuracy instrumentation amplifier (INA101, Burr-Brown [112]) were used as front-ends of the controller. This instrumentation amplifier is specially designed for low-level signal amplification where three precision operational amplifiers (OpAmp) and laser-trimmed metal film resistors are integrated on a single monolithic chip. The differential gain of this IC can be set by connecting a single external resistor ($R_{\mathrm{G}} = 200\,\Omega \Rightarrow G = 201$). The INA101 offers external offset adjustment which can be used to null its output at zero flow. This allows for adjustment to the resistance differences of the sensing leads (see Sec. 4.1). Furthermore, two INA101 output signals are inverted by further OpAmps to revert the sign of the voltage of the outer sensing leads in order to easily generate the temperature difference signal U_2. Simple circuit simulations where carried out and verified with measurements on a breadboard prototype where gain and offset adjustments are tested. These simple experiments proved that the INA101 is a suitable candidate.

The next decision considers the choice of the controller for the heat source. Since, the signals of the sensing leads are small it seems appropriate to use an analog electronic controller. In addition to the printed board circuit for conditioning of the small signals, an analog controller can be easily added to form a compact sensor

interface. It can be built and easily adjusted via OpAmps with passive components. The use of OpAmps causes some problems due to their non-ideal properties [113]. First, there is an offset voltage which can be expressed as:

$$\Delta U_{\mathrm{off}}(\vartheta, U_{\mathrm{B}}, t) = \frac{\partial U_{\mathrm{off}}}{\partial \vartheta}\Delta\vartheta + \frac{\partial U_{\mathrm{off}}}{\partial U_{\mathrm{B}}}\Delta U_{\mathrm{B}} + \frac{\partial U_{\mathrm{off}}}{\partial t}\Delta t \quad , \tag{4.11}$$

where ϑ is the temperature, U_{B} is the supply voltage, and t is the time [114]. Since the final goal is to measure in HVAC systems over a long period of time combined with considerable temperature variation, the drift of the offset voltage with time and temperature will become an issue which must be investigated through long term characterization of the complete sensor in HVAC environments. Other possible issues may result from gain nonlinearity, limited suppression of the supply voltage variations, input offset voltage and input bias current, and noise. The INA101 features an offset voltage of max 25 µV with a comparable low offset drift of max 0.25 µV/°C, a nonlinearity of 0.002 %, a bias current of ±5 nA, and a noise of 13 nV/$\sqrt{\mathrm{Hz}}$.

There are several architectures of analog electronic controllers where the most common types are P-, I-, PI-, PD- and PID controllers [115]. They are classified by their feasible transient behavior. The P-controller output signal is proportional to the difference between actual value and desired value, i.e., the error signal at the controller input. This architecture enables a fast dynamic controller response but it cannot null the error signal completely. The so-called I-controller integrates the input to form the controller output signal. Therefore, any finite deviation would lead to a feedback signal increasing in magnitude with time. Thus, the integrating feedback loop prevents stationary deviation between actual and desired value. The dynamics of the integration feedback loop is determined by the respective loop gain. Again, the phase delay of this feedback loop must be considered to provide stable operation of the I-controller. Usually, I-controllers feature very limited bandwidth. On the other hand, with an increasing I-influence the attenuation of the controller output also increases. If a P-controller is combined with an I-controller, a PI-controller is established. It allows to use the advantages of both controllers and neglect their drawbacks. Actually, there are two feedback branches operating in parallel. The total feedback signal $y_{\mathrm{R}}(t)$ is then the addition of the P- and the I-amount which can be expressed as:

$$y_{\mathrm{R}}(t) = k_{\mathrm{R}}\left[e(t) + \frac{1}{T_{\mathrm{n}}}\cdot\int e(t)\ \mathrm{d}t\right] \quad , \tag{4.12}$$

where $e(t)$ is the control deviation, k_{R} is the gain, and T_{n} is the reset time. These are the two adjustable parameters of a PI-controller and they are defined by passive elements in an OpAmp based architecture.

The PD-controller combines an amount in proportion to the time derivative (D) of the deviation signal with an amount that is proportional (P) to the deviation signal. The time derivative is important whenever a controller should quickly react to fast changes of the deviation signal. By combining the three basic elements (P, I, and

D) a PID-controller is established which can be expressed as:

$$y_{\mathrm{R}}(t) = k_{\mathrm{PR}} \left[e(t) + \frac{1}{T_{\mathrm{n}}} \cdot \int e(t)\ \mathrm{d}t + T_{\mathrm{v}} \frac{\mathrm{d}e(t)}{\mathrm{d}t} \right] \quad , \tag{4.13}$$

where k_{PR} is the gain and T_{v} is derivative time (rate time). The PID-controller is the most flexible of the presented architectures but requires the highest effort for optimum adjustment of its parameters. Therefore, the most common way to build a PID-controller is to generate each component of the controller feedback signal (P, I, and D- signal) separately. However, it is possible to realize the controller with a single amplifier. By using only a single OpAmp for the controller circuit, its gain and time parameters are not independently adjustable. The appropriate design of such controller circuits is very challenging and typically restricted to mass products where a costly design procedure is payed back by large scale production. The preferable approach for prototyping is the use of separate OpAmps for each elementary feedback function.

Not every controller architecture is suited to combine well with a specific controlled system: this can lead to instability. Instability is one of the most unpleasant effects. Therefore, exploring the transient behavior of the controlled system is the first essential step. The sensor's transient behavior is already known from Sec. 4.1. However, the transient behavior including the signal conditioning electronics is required for the design of the controller. Therefore, the step response of the sensor with electronics is measured for a heating voltage of 10 V. The transient behavior of this system is identified as a $\mathrm{PT}_2 -$ system (Fig. 4.23). From the step response characteristic parameters of the controlled system (Fig. 4.23) are extracted which are then used to design the controller and, further, to optimize it. According to the diagram, a down time $T_{\mathrm{u}} = 0.4\,\mathrm{s}$ follows, i.e., the time from the applied step to the point where the inflectional tangent crosses the abscissa. The time from the point where the inflectional tangent crosses the abscissa to the point where the tangent crosses the set point is called adjusting time and amounts $T_{\mathrm{g}} = 4.5\,\mathrm{s}$. Finally, the stationary gain of the controlled system is identified as $K_{\mathrm{s}} = 0.054$.

After characterizing the controlled system, a PI-controller was chosen. While a PID-controller would be faster but the time constants of the system are rather slow (20 s), it indicates that a D-element is not necessarily required. Moreover, the D-element in combination with the down time may tend to instability. However, the step response of the controlled system was not specified when the analog circuit was designed. Hence, a flexible PI-controller architecture was placed on the printed board electronics. Figure 4.24 depicts the corresponding analog circuit with separate adjustment of the P (R1) and I (R2 and C2) branch. The main goal is to design the controller in such a way to achieve an advantageous dimensioning of the whole control circuit. The composition of the controller has to consider the dynamic quality, the quality factor in the time- and frequency domain, and the response of a change of the reference or/and the error variable.

A theoretical method for designing a controller is to use differential equations according to the vast control system literature [115–119]. However, there are more

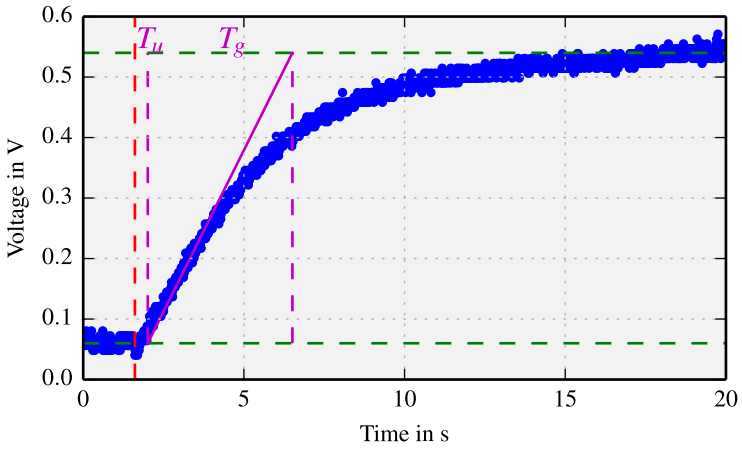

Figure 4.23: Step response of sensor (S3.1) and signal conditioning electronics when a 10 V step is applied at the heater. A sampling interval of 10 ms was applied. The evaluation of the down time T_u and the adjusting time T_g is indicated [114].

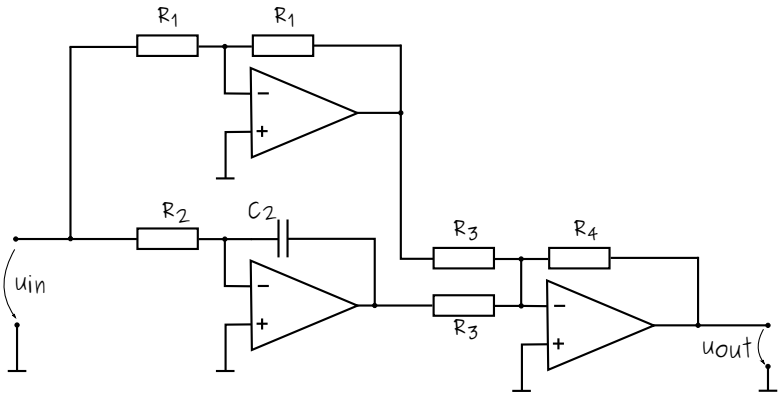

Figure 4.24: Electronic PI controller with separated adjustment for P and I parameters (inverting). The controller branches are combined with an inverting summation OpAmp circuit.

practical tuning rules where the substantial effort of solving differential equations are avoided. There are popular design rules [114] from Ziegler and Nichols, from Chien, Hrones, and Reswick, or the T-sum-control rule. The tuning rules from Chien, Hrones, and Reswick are based on the step response of the controlled system (see Fig. 4.23). Table 4.7 gives an overview of different dimensioning formula for the controller parameters k_R, T_N, and T_V for the P, PI, and PID controller architectures. There are four specific cases of controller dimensioning to choose from depending on the targeted application. Two refer to a step change of a disturbance of the controlled system and another two for the tracking of step changes of the set point signal. Each case is further divided in an aperiodic control response with zero overshoot and a control progress with, e.g., 20% overshoot.

The disturbance related response is of relevance when the flow velocity changes. However, the dynamics of the controlled system also changes and the control loop may deviate from optimum behavior. Therefore, the fastest control progress with

Type	Parameter	Disturbance step		Guide step	
		Aperiodic control progress ($\ddot{u} = 0\%$)	**Control progress** ($\ddot{u} = 20\%$)	**Aperiodic control progress** ($\ddot{u} = 0\%$)	**Control progress** ($\ddot{u} = 20\%$)
P	k_R	$0.3\frac{T_\mathrm{g}}{T_\mathrm{u} \cdot k_\mathrm{S}}$	$0.7\frac{T_\mathrm{g}}{T_\mathrm{u} \cdot k_\mathrm{S}}$	$0.3\frac{T_\mathrm{g}}{T_\mathrm{u} \cdot k_\mathrm{S}}$	$0.7\frac{T_\mathrm{g}}{T_\mathrm{u} \cdot k_\mathrm{S}}$
PI	k_R	$0.6\frac{T_\mathrm{g}}{T_\mathrm{u} \cdot k_\mathrm{S}}$	$0.7\frac{T_\mathrm{g}}{T_\mathrm{u} \cdot k_\mathrm{S}}$	$0.35\frac{T_\mathrm{g}}{T_\mathrm{u} \cdot k_\mathrm{S}}$	$0.6\frac{T_\mathrm{g}}{T_\mathrm{u} \cdot k_\mathrm{S}}$
	T_N	$4.0 \cdot T_\mathrm{u}$	$2.3 \cdot T_\mathrm{u}$	$1.2 \cdot T_\mathrm{g}$	$1.0 \cdot T_\mathrm{g}$
PID	k_R	$0.95\frac{T_\mathrm{g}}{T_\mathrm{u} \cdot k_\mathrm{S}}$	$1.20\frac{T_\mathrm{g}}{T_\mathrm{u} \cdot k_\mathrm{S}}$	$0.6\frac{T_\mathrm{g}}{T_\mathrm{u} \cdot k_\mathrm{S}}$	$0.95\frac{T_\mathrm{g}}{T_\mathrm{u} \cdot k_\mathrm{S}}$
	T_N	$2.4 \cdot T_\mathrm{u}$	$2.0 \cdot T_\mathrm{u}$	$1.0 \cdot T_\mathrm{g}$	$1.35 \cdot T_\mathrm{g}$
	T_V	$0.42 \cdot T_\mathrm{u}$	$0.42 \cdot T_\mathrm{u}$	$0.50 \cdot T_\mathrm{g}$	$0.47 \cdot T_\mathrm{g}$

Table 4.7: Setting values for the controller parameters as per Chien, Hrones, and Reswick (only usable for $T_\mathrm{g}/T_\mathrm{u} > 3$). The down time T_u, the compensation time T_g, and the system gain k_s are calculated from the step response of the controlled system while $\ddot{u}$ is the overshoot, k_R is the proportional coefficient, T_n the reset time, and T_V the lead time (Tab. 10.3-3 and 10.3-4 [114]).

20% overshoot for the step response was reached with the setting values $k_\mathrm{r} = 125$ and $T_\mathrm{N} = 1.6\,\mathrm{s}$. These values are achieved by the parameter of passive components in the PI-controller circuit (see Fig. 4.24) and the values of the passive components are calculated with the equations:

$$\begin{aligned} k_\mathrm{R} &= \frac{R_4}{R_3} \\ T_\mathrm{N} &= R_2 C_2 \quad . \end{aligned} \tag{4.14}$$

As can be seen, some values of the passive components have to be chosen and the corresponding ones calculated with Eq. 4.14 to: $R_1 = 10\,\mathrm{k\Omega}$, $R_2 = 220\,\mathrm{k\Omega}$, $C_2 = 6.9\,\mu\mathrm{F}$, $R_3 = 1\,\mathrm{k\Omega}$, $R_4 = 120\,\mathrm{k\Omega}$. Now, all components are dimensioned and the circuit is ready for testing. The complete analog circuit is depicted in Sec. B.1.

Controller Measurements

The sensors were connected with the signal conditioning circuits followed by the PI-controller and then measured under the same conditions as described in Sec. 4.3

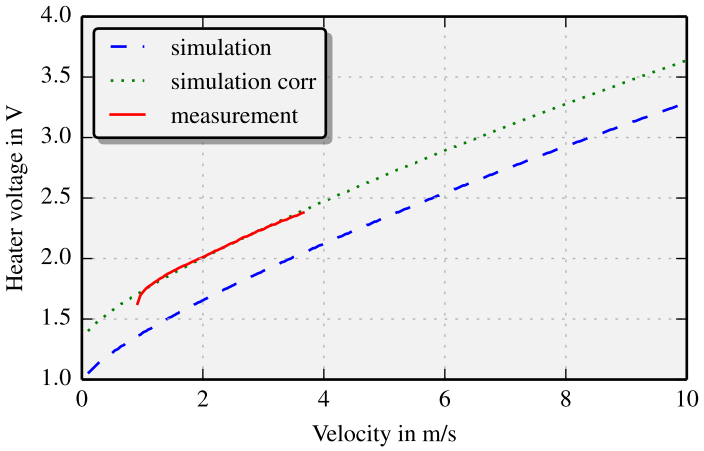

Figure 4.25: Result of the PI-controller experiments along with related simulation data. The heater voltage U_{H} is depicted as a function of the mean flow velocity in constant temperature mode.

(see Fig. 4.20). Instead of recording each of the four sensing lead signals, only the heater voltage as a function of the mean flow velocity was evaluated.

Figure 4.25 shows the flow dependence of the heater voltage of the PI-controller in comparison with corresponding simulation results. There are several reasons for the mismatch between simulation and measurement. The first one is the influence of a parasitic resistor in series with the heater occurring only in the measurements case while the simulations returned only the voltage directly at the terminals of the heating lead. Therefore, for comparison of the two results, a small offset correction is necessary. Another reason is the difference between modeled and experimental boundary conditions (tip and end of the sensor) which are not implemented in the 2D simulation. The last one regards the heating power. When the lead is heated, not the complete power contributes to the convection. In detail, the sensor heats up, which is still covered by the simulation, but there is also heating power lost backwards from the sensor (out of the pipe). This results in an offset of the applied heating power between simulation and measurement.

However, with an offset correction of $0.35\,V$ the simulation was modified and then the simulation is in good agreement with the measurement. As can be seen, the heater voltage U_{H} (measured) shows a strictly monotonically increasing behavior over the measurement range (0.9 to 3.66 m/s). According to Fig. 4.25, the flow velocity can clearly be assigned to the corresponding heater voltage. The maximum velocity of the implemented measurement setup was limited to 3.66 m/s, but in HVAC systems the velocity can reach up to 8 m/s. The tendency of the constant temperature mode and the comparison with simulation results suggests that this approach is also suitable for higher velocities. However, this has to be tested and verified with additional measurements where higher velocities are in the focus. For instance, the high density of heat dissipation in the heating leads may cause reliability issues.

Field Tests

Field tests with the third layout sensor family (Sec. 3.4) were performed at the "Energetikum" in cooperation with the University of Applied Sciences Burgenland (Fig. 4.26). This facility is a living lab with sensors and actuators placed all over the building. The main part of the setup is a coiled pipe, common in many HVAC systems, to build a realistic but also easy accessible and controllable test environment before testing the sensor in a real HVAC system. This 15 m long pipe is split into two parts where the first one is 10 m long with a pipe diameter of 250 mm. This part is used as a transition channel. It is necessary to suppress flow irregularities induced at the pipe entrance and to achieve a steady flow at low velocities. In the last third of this part the PCB sensor is stretched across the pipe (Fig. 4.26 - Control station). The second part is 5 m long and starts with a coupling of 250 mm to 400 mm. This coupling is necessary because reference flow sensor and fan have larger dimensions.

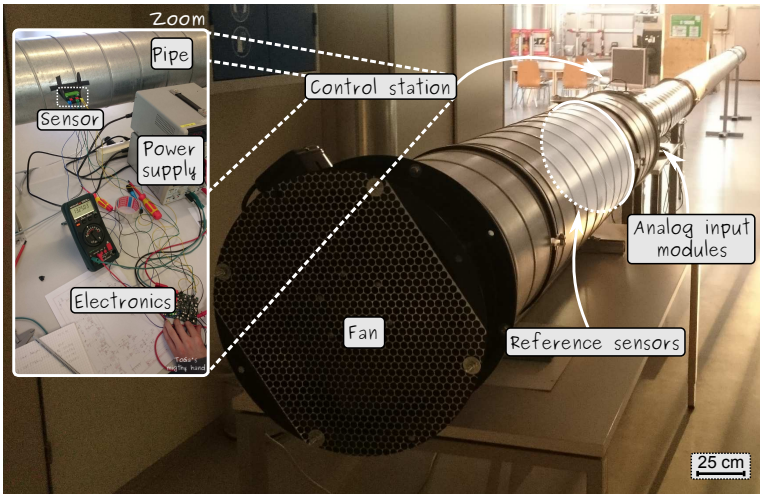

Figure 4.26: HVAC test facility at the University of Applied Sciences Burgenland. At the control section (inset) the sensor is mounted across the pipe. The power supply and PI controller are located nearby. Downstream of the control section, the reference flow meter and additional sensors (ambient temperature, humidity, ambient pressure) are placed. At the end of the pipe a fan is mounted to draw air through the pipe. At the tip of the pipe there is only a long 10 m transition channel to suppress the flow irregularities induced at the pipe entrance.

The reference sensor is a differential pressure sensor (Sec. 1.3) of the type MKS Barathon 220DD. IT operates on the variable capacitance technique. On one side of the sensor head, where the pressure has to be measured, is a tensioned metal diaphragm located. The other side is opposed to an electrode assembly and when the diaphragm deflects, a capacitance change generates a voltage linear to the pressure. The fan used for generating the volumetric air flow is the AR sileo 400E4 from J. Pichler GmbH. It has a rotor with bionic designed blades, a rated power of 240 W,

and a maximum rotational speed of $1320\,\mathrm{min}^{-1}$ to generate a volumetric air flow up to $3863\,\mathrm{m}^3/\mathrm{h}$.

There are several parameters of interest which are recorded during the measurements. The ambient temperature and humidity are recorded with a stainless steel Vaisala probe (HMP110 C15A0 C3B0). The ambient pressure is measured with a Vaisala PTB220 digital barometer. Of course the heater voltage of the flow sensor, the time, the rotational speed of the fan, and the pressure values of the reference flow sensor also have to be measured simultaneously. All these parameters are recorded via an analog digital converter FP-AI-110 from Texas Instruments. It has eight analog voltage or current input channels with 16-bit resolution.

Before the measurements could start, the sensor has to be put through the channel and mounted under slight tension to prevent the sensor from vibrating. To save time two 3D printed parts were designed for the sensor mount (see appendix Sec. A.3).

The mean air flow velocities are evaluated from the signals of a differential pressure sensor. First, the differential pressure is measured and then corrected with the offset pressure (ambient pressure - Vaisala PTB220 barometer) at zero flow in the test pipe. Next, the volume flow rate is calculated with:

$$\dot{V} = C_{\mathrm{frame}} \cdot \sqrt{dp_{\mathrm{corr}}} \quad , \tag{4.15}$$

where dp_{corr} is the corrected differential pressure, and $\mathrm{C_{frame}}$ is a characteristic of the frame including the air density. The air density is calculated from material properties, the actual values of temperature, humidity, and the ambient pressure, respectively. With the computed air density and further frame parameters, C_{frame} is read from a look-up-table of the frame data sheet. With Eq. 1.1, Eq. 4.15, and the area of the test pipe, the mean air flow velocity is evaluated. Table 4.8 depicts the measured and its consequential parameters for several interesting points. As can be seen, the correction of the differential pressure is necessary to calculate the mean flow velocity precisely. According to the maintainer of the HVAC test facility, the resulting error of the mean air flow velocity in the HVAC pipe setup then amounts $\pm 0.15\,\mathrm{m/s} + 5\%$ from reading.

The electronic circuit designed for sensor characterization works with $\pm 12\,\mathrm{V}$ supply. In connection with the typical lead resistance of a 250 mm long PCB flow sensor (S4.1), the supply voltage limits the available heating power. Therefore, flow transduction using the constant excess temperature mode was restricted to the flow range 0 to 2 m/s. In a redesign of the electronics, the supply voltage was increased to $\pm 20\,\mathrm{V}$ so a higher heating power is possible. However, the input span of the implemented analog to digital converter was limited to $\pm 10\,\mathrm{V}$ requiring an attenuation of the heater voltage in front of the ADC (analog digital converter). In the subsequent section, the according correction of the digital data is done without any further comment.

After redesign and with the new sensor layout (S4.1) the transient behavior also changed. Therefore, the procedure to design the PI controller was repeated as

dp	T	φ	dp_{corr}	$\dot{V}$	$\bar{v}$
Pa	°C	%	Pa	m^3/h	m/s
-1.462	24.14	44.40	0.002	8	0.05
-0.382	23.96	45.18	1.080	178	1.00
2.871	23.82	45.50	4.333	356	2.02
8.774	24.03	45.13	10.236	548	3.10
15.827	23.99	44.95	17.287	712	4.03
25.916	23.90	45.64	27.376	896	5.07
37.155	23.83	46.72	38.614	1064	6.02

Table 4.8: Measured parameters for calculating the mean air flow velocity in the test pipe. Differential pressure dp, ambient temperature T, and ambient humidity φ are measured while offset corrected pressure dp_{corr}, volumetric air flow rate $\dot{V}$, and mean air flow velocity $\bar{v}$ are derived from the measured ones.

described in Sec. 4.3. The new values of the controller are set to $R_1 = 10\,\mathrm{k\Omega}$, $R_2 = 220\,\mathrm{k\Omega}$, $C_2 = 6.9\,\mu\mathrm{F}$, $R_3 = 10\,\mathrm{k\Omega}$, $R_4 = 130\,\mathrm{k\Omega}$.

Before the measurements could be performed, the operating point of the sensor must be defined. All four sensing lead currents are set to 10 mA so negligible self-heating is assured. At zero flow velocity and without heating, the output signal of each front-end is set to 0.5 V. Next, the set point voltage which determines the excess temperature was adjusted to 55 mV leading to a heater voltage of 6.6 V at zero flow velocity. This is necessary because the system cannot be cooled actively, only passively by turning off heating. If the PI-controller receives a negative command value, the sign of controller output current changes but this does not mean that the heater absorbs energy. Therefore, these offset values are used to avoid a negative command value. Figure 4.27 depicts the results of the measurement at the test environment. Finally, flow velocities up to $6 \pm 0.15\,\mathrm{m/s} + 5\,\%$ from reading were easily measurable with the modified electronic setup.

For the last measurements, the same sensor (S4.1) is installed in a real HVAC system at the Energetikum (Fig. 4.28). The sensor was placed in a pipe with 250 mm diameter. This pipe is a merging pipe from two offices. Although, the space was restricted, the installation was easy and fast. Only two holes had to be drilled, the sensor was spanned across the pipe, and two mounts were attached on the pipe to hold the sensor. A reference sensor was located one meter downstream of the sensor. The reference sensor was an IVL 10 air velocity and temperature sensor (Produal Oy). The PI-controller, the power supply, and the ADC transmitter module were placed near the two measuring devices. This ADC transmitter module was an NI WSN-3226 node (National Instruments) and recorded the results from the PI-

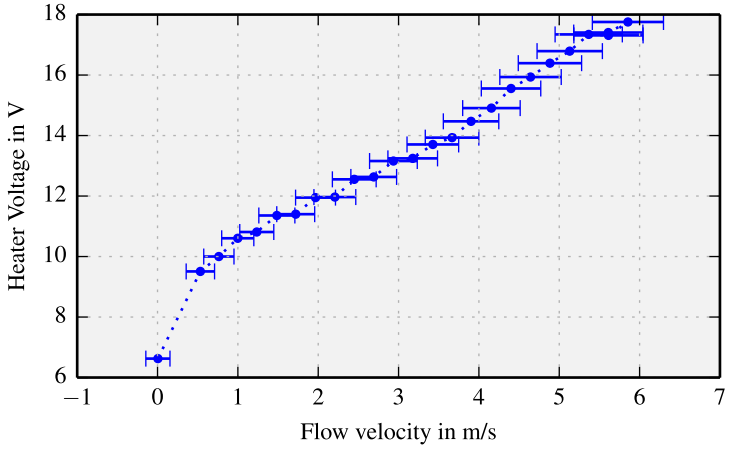

Figure 4.27: Measurement results from the field test experiments. The heater voltage U_H is plotted as a function of the mean flow velocity where the error bars indicate the error of the reference sensor. The installed fan enables flow measurements from 0.53 m/s up to 10 m/s. However, only flow velocities up to 6 m/s were measurable with the electronic setup.

controller and the reference sensor. In detail, this module was a four channel, low power, wireless voltage/resistance measuring device which communicates with gateways to form a wireless sensor network. The gateway (NI WSN-9791) was connected to a host PC, running NI LabVIEW, to display measurement results, status information, and to change the gateway or device settings. In each office, the HVAC outlet angle was controlled via a GLB181.1 E/3 compact controller (Siemens) through a central and automated monitoring system. However, it was possible to manually regulate each controller, so the air flow velocity was set at well-defined values.

Figure 4.29 depicts the results of the measurement at the Energetikum HVAC in comparison with the measurements in the recreated pipe ("Bigpipe"). The electronics are adjusted as for the measurements in the pipe of the test facility. With the overall control system of the HVAC system two outlets and the corresponding ventilators are set to generate specific flow velocities. However, this is also the reason for the difference between the measurements of the Energetikum and the Bigpipe because the velocity cannot be set exactly to zero. There is still a little slit in the outlets which causes a small volumetric flow. So, even if the electronics are set to the same zero value as in the recreated pipe, there is still an offset between the two experiments. In combination with the very limited accuracy of the reference sensor (± 0.5 m/s $\pm$ 7 % from reading) it is not possible to adjust the sensor as accurately as in the test experiments. Installing a more accurate reference sensor was not possible, because such a sensor could not be calibrated with the HVAC system. The measurements at the Energetikum should reveal how to install the sensor in an existing HVAC system and show possible improvements for building a working prototype.

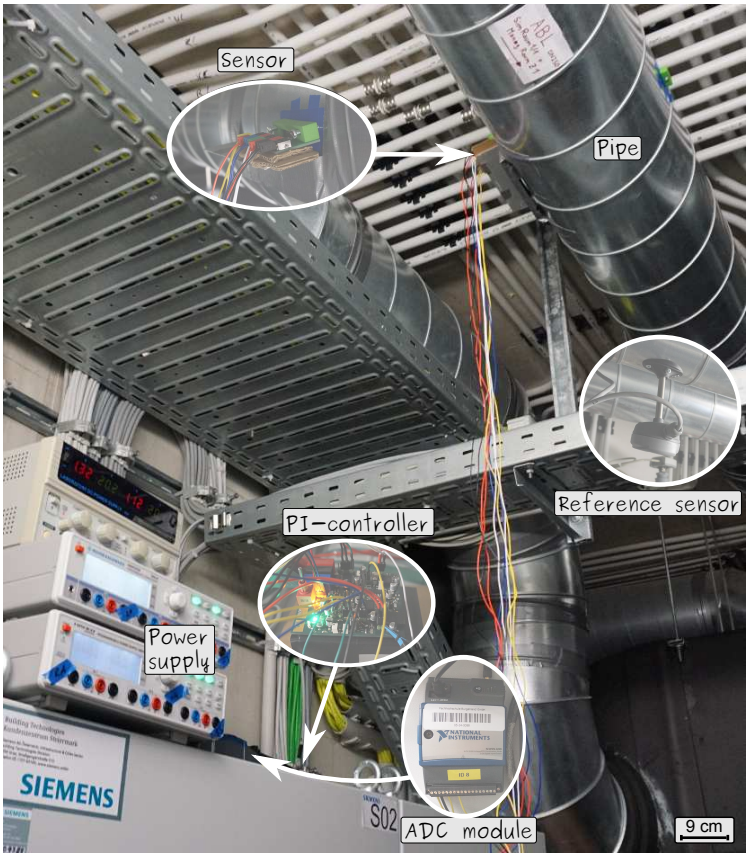

Figure 4.28: HVAC setup at the Energetikum facility. The PCB flow sensor is placed in a pipe in the same way as it was placed in the test environment. A reference flow meter (reference sensor) was located 1 m downstream of the sensor. The signals from both sensors are recorded with an ADC module which sends the data via WLAN to a central server.

Another test in the Energetikum facility focuses on the long term behavior of the S4.1 sensor (Fig. 4.30) to characterize the drift under real operating conditions. Therefore, the PCB and a reference sensor measured the flow velocity in a normal working mode over a couple of days. This means the control systems adjusted the outlets and ventilator speeds automatically to the programmed values. At night the system shuts down leading to no air flow. In the morning the system starts and keeps the temperature and fresh air flow at the defined level over the working period into the afternoon. Both PCB and reference sensor show the same behavior which proves that the PCB sensor was working correctly over three days. However, as mentioned previously, due to the accuracy of the reference sensor the PCB sensor cannot be calibrated accordingly allowing only qualitative evaluation of the PCB sensor. A major result is that there was no measurable drift of the zero point during the three days.

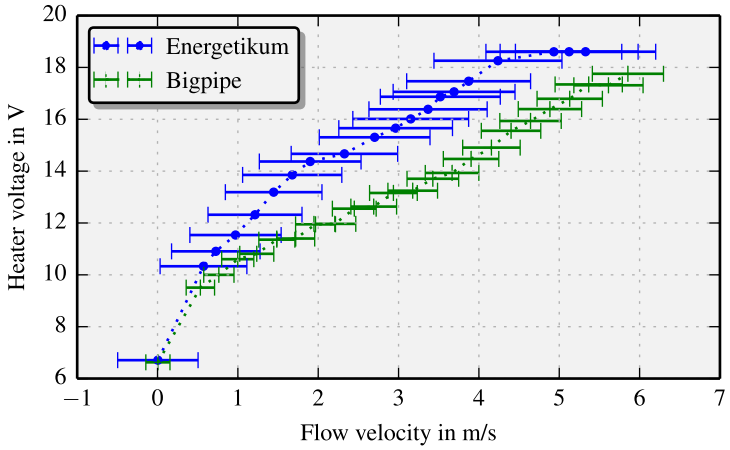

Figure 4.29: Heater voltage in dependence of the mean flow velocity. Energetikum and Bigpipe refer to the test facility Energetikum and to the the field test measurement, respectively. There is a difference between the measurements because the velocity at the Energetikum cannot be set exactly to zero and because the accuracy of the reference sensor is very limited.

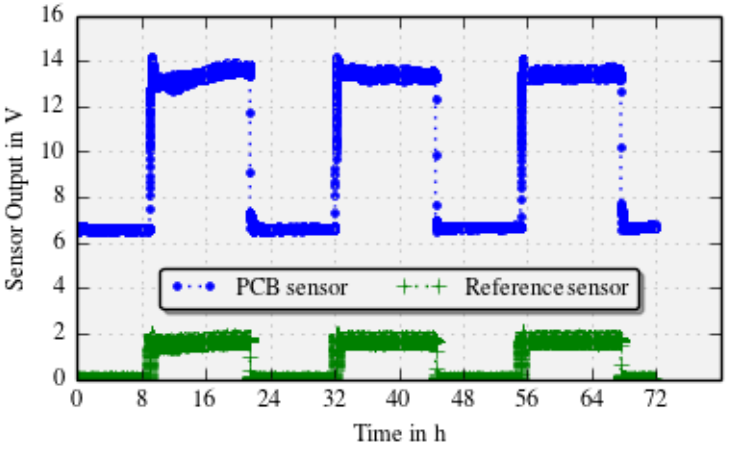

Figure 4.30: Long term measurements at the Energetikum facility. The whole HVAC system was controlled by an automatic system. PCB and reference sensor were measured every 10 s during 72 h. The scaling factor for the reference sensor is 1 V $\triangleq$ 1 m/s ($\pm$0.5 m/s $\pm$ 7% from reading) while for the PCB it is shown in Fig. 4.29.

4.4 Summary of Chapter 4: Experiments and Results

Resistance measurements were carried out regarding the resistance of the sensors and the used equipment.

* The measurement equipment was evaluated on whether it can measure small resistance changes accurately enough.
* A developed adapter board was measured to reveal its resistance influence
* The so-called sheet resistance was introduced for comparison:

$$R_{\mathrm{s}} = R\frac{w}{l} \quad .$$

* The differences between left and right copper sensing leads were analyzed:

$$\triangle R = \frac{R_{\mathrm{left}} - R_{\mathrm{right}}}{\frac{R_{\mathrm{left}}+R_{\mathrm{right}}}{2}} \quad .$$

* The measurements revealed a huge difference between the individual copper leads at the proof-of-concept design. The main reason was found in the additional etching step which was then dismissed for the next designs.
* The transient temporal behavior of the sensor was studied to verify and optimize the simulation and to find out when an accurate velocity measurement is possible.

Lock-in measurements were performed to reveal the flow velocity dependence of the sensor.

* An experimental setup with an acrylic glass pipe and a double vane fan, which was controlled via a power supply, was constructed and verified.
* The copper leads were merged to a Wheatstone bridge which was supplied with a waveform generator and read out with a lock-in amplifier.
* Several experiments were performed to find offset and bridge voltages, sensibilities, and velocity ranges for the different designs.
* The outcome of these experiments showed that the velocity range is not wide enough for the targeted application.

Other thermoresistive approaches are investigated to find a way to expand the velocity range.

* The hot-film principle is also not usable but from corresponding measurements three relevant voltages were deduced with one leading to a feasible novel operation mode.
* By keeping the sum of the mean temperature around the heater and the mean temperature at the periphery of the PCB constant, the heater voltage to achieve this becomes a function of the flow velocity.
* The simulations are adapted for this constant temperature mode in closed loop operation.

* An analog PI controller with separate adjustable parameters was developed and its components designed with the tuning rules from Chien, Hrones, and Reswick. Therefore, the step response of the system was analyzed.
* Measurements with the analog controller are performed and compared with the simulation results. There are differences between these two results but the reasons are known and are compensated via a small correction factor.
* Measurements at the University of Applied Science Burgenland are performed to test the sensor in higher velocity ranges. A new sensor was designed to fit in these larger pipes and therefore, the electronics had to be adjusted accordingly. The sensor is now able to measure flow velocities up to 6 m/s.
* The last experiments were performed in a living lab to test the sensor in a real environment over a long period.

Chapter 5

Discussion, Conclusion, and Outlook

In the last chapter the achieved results are highlighted and the most important findings are discussed. Then, the entire scientific work is concluded with additional comments and ideas that could not be considered within the research project. At the end, further steps to transfer the prototype into a commercial sensor are given.

5.1 Discussion

The first results for designing a thermal flow sensor on PCB technology are gained from the developed analytical model and from subsequent FEM simulations. From the deduced differential equation (Eq. 3.7) the excess temperature at the sensor surface (Fig. 3.4) is evaluated resulting in the typical output behavior of a calorimetric thermal flow sensor at the specified dimensions (Fig. 3.5). For increasing the sensitivity or extending the measurement range at a specific heating power, additional sensing elements are implemented and evaluated (Fig. 3.6). Therefore, by changing the sensing position or heating power, the output characteristic can be tuned to fit the required specifications.

However, there are several simplifications which limit the results of the analytical model. First, the sensor is assumed symmetric around the horizontal axis (parallel to the flow) which is not the case because heater and sensing elements are placed on top of the substrate and covered by a protective layer instead of being embedded in the substrate. Next, it is assumed that the temperature field does not change along the lateral axis (along the leads) and the boundaries at the beginning and the end of the sensor are neglected. The flow is assumed as a uniform flow velocity and the heating power is generated only by a line source where no heat losses in the out-of-plane direction are covered. Although there are several limitations in this model, the analytical model with it simplifications is used to get a qualitative insight of such flow sensors and it is the first step to a sensor design.

In the simulation model more realistic boundary conditions are implemented as well as fabrication limits of the PCB manufacturer (Fig. 3.7). At first, the transient behavior of the sensor at constant heating (constant current mode) and for different

flow velocities is evaluated (Fig. 3.8). This leads to a transient temperature of the sensing elements (Fig. 3.10). Afterwards, these transients are evaluated for different flow velocities (Fig. 3.11) confirming the analytical model and that the targeted transduction principle is feasible.

Next, the simulations are extended to compute the constant temperature mode. The new outcome is a temperature difference matrix (Fig. 3.12) where parameter sweeps with the inlet flow velocity and the injected heating power are performed. From this matrix the heating voltage as a function of the mean flow velocity is deduced (see Fig. 3.13). Now, the heater voltage increases monotonically over the targeted velocity range ($0 - 10\,\mathrm{m/s}$). However, there have to be several simplifications of the simulation taken into account which lead to these results. First and foremost, the developed simulation is a 2D FEM simulation with all its benefits and drawbacks. It is assumed that the temperature field does not change in lateral direction which may apply to the middle of the sensor. Whereas, the cooper leads are placed at the tip of the sensor reversing loops and at the bottom there are connection lines to the connection pads which both disturb the temperature field. Another drawback is that a small amount of injected heat power does not contribute to the convection heat transfer because it flows back via the connection lines disappearing completely from the flow environment. Therefore, the injected heating power in the simulation is higher than in reality and, as a result, the simulated voltage in constant temperature mode is lower than in reality. Additionally, it is only the voltage simulated which is directly needed at the heater. There are additional supply lines to the heater and contact resistances causing further deviations.

First experimental results regarding the sheet resistance of the copper leads put the project on a knife edge. The variation of the copper lead resistances was so high (Fig. 4.2), that a simple readout method seems unfeasible because it could require a sophisticated readout electronics needing more parts, place, energy, and higher costs which is contrary to the intention of the research project. The main cause for these huge differences was an additional etching step which was implemented to decrease the height of the copper leads. According to the manufacturer the etching solution is not homogeneous over the entire bath. With a new thinner laminate this devastating etching step can be avoided and with optimized process parameters the precision increased significantly for the first prototype over the proof-of-concept (Tab. 4.2). For the second prototype an even thinner laminate was used, increasing the precision further more (Fig. 4.5). The results of these measurements revealed that it is possible to produce thermal flow sensors based only on PCB technology but with limited precision.

Then, the transient behavior of the copper leads was experimentally measured (Fig. 4.7) and compared (Fig. 4.8) with simulation results for optimization. These results validate the heat transfer model confirming the time which is needed to reach sufficient thermal saturation for intermittent flow measurements.

Next, lock-in experiments study the sensor response as a function of the mean flow velocity. Therefore, the sensing leads are connected in a Wheatstone bridge

configuration and its bridge voltage is measured (Fig. 4.13) while a constant heating power is applied to the heater. This bridge voltage is evaluated for different mean flow velocities revealing the flow conversion characteristic of the sensor (Fig. 4.14) which is typical for the transduction behavior of calorimetric sensors. This result shows the limits of the pure calorimetric readout method. Major drawbacks are the ambiguity of the output signal and the limited measurement range due to thermal saturation.

To overcome this ambiguity of the output signal it is combined with a threshold value which is gained from one or two sensing leads. First, the maximum of the Wheatstone readout is shifted into a low velocity (for instance:$< 0.5\,\mathrm{m/s}$, Fig. 3.6), which is rarely in normal operation of HVAC systems, by adjusting the parameters. Then, the threshold voltage of the sensing lead (for instance: 1 mV) is gained at this velocity (Fig. 3.11). The Wheatstone signal which can occur at two flow velocities (for instance: 80 µV of 0.25 or 1.6 m/s, see Fig. 4.14) is compared to the threshold voltage. Now, it is possible to easily determine the correct flow velocity, for instance: if the threshold voltage is below 1 mV then the flow velocity is 1.6 m/s else it is 0.25 m/s.

To shift the thermal saturation into high velocity ranges, several geometric parameters are varied (Fig. 4.16 - 4.18). However, regardless how the geometric parameters are adjusted, the sensor reaches saturation around 4 m/s. Consequently, the pure calorimetric principle with constant heating power will not work in the targeted measurement range!

Experiments with the constant temperature mode focus on finding a solution how to run the sensor in a closed loop operation mode to extend the measurement range. Thereby, each copper lead is measured individually with 100 mW heating power at different flow velocities confirming the expected hot-film output behavior (Fig. 4.21). This means, all lead voltages decrease with increasing flow velocity. Then, three signals (Fig. 4.22) are deduced from these measurements to find a suitable command variable for the controller. At first glance, none of these voltages seem usable because the constant temperature mode needs the ambient temperature to work properly. So far, the ambient temperature is not measured precisely anywhere and the only option is to relocate the outer sensing leads as far away as possible from the heater to achieve this.

Nevertheless, signal U_2, which represents the temperature difference between the mean temperature around the heater and the mean temperature at the periphery of the PCB, allows to measure a constant temperature difference. By keeping this signal at a constant level, the heating voltage (U_H) is a strictly monotonous function of the velocity. This constant temperature mode will work at typical conditions in HVAC systems.

To verify this constant temperature mode an analog controller was dimensioned by applying a step response to the sensor combined with its amplifier electronics (Fig. 4.23). Subsequently, characteristic parameters from a step response were evaluated. With the tuning rules from Chien, Hrones, and Reswick the setting values

for the analog controller were calculated. The sensor was tested in the same pipe as before but this time with the controller focusing only on the heater voltage. In Fig. 4.25 the results of the measurement and the simulation are compared revealing the error of the simulation. The error of the simulation is caused by several simplifications and after implementing a correction factor, the results are in good agreement. Nevertheless, the measurement results confirm the monotonic increase of the heater voltage as a function of the mean flow velocity.

There are still two major drawbacks with the measurements (Fig. 4.25). First, due to the restrictions of the experimental setup it is still not possible to test mean flow velocities over 4 m/s. Second, it is difficult to generate a smooth flow at low velocities (< 0.5 m/s). At these velocities the fan rotates slowly so that the influence of the pulses of the fan blades is noticeable. Nevertheless, such small flow velocities are not common in HVAC systems making this problem less important.

The field tests (see Fig. 4.29) show the behavior of the sensor in a real HVAC environments. A new sensor design was developed to fit the specific dimension and the controller was adapted. It should be pointed out that even velocities up to 9 m/s were tested but at these high velocities the sensor tends to vibrate if it is not mounted tightly. To avoid any damage to the sensor and the subsequent parts (reference sensor, fan, etc) the velocity upper limit was set to 6 m/s. Up to this level the targeted monotonic characteristic was achieved. As can be seen, there are considerable differences in measurements in the two test environments caused by two main factors. First and foremost is the limited accuracy of the installed flow sensor of the Energetikum facility which severely deteriorated the reference measurement of the adjusted flow. On the one hand, this is bad news because the measurement cannot be taken seriously for any form of comparison or calibration leaving several questions unanswered. On the other hand, this stresses the urgent need for a specifically designed, robust, and cost-effective alternative flow velocity sensor. Second, the velocity could not be set exactly to zero considering an additional offset during calibration of the PCB sensor.

Finally, the long term measurements focused on typical HVAC operation over several days (see Fig. 4.30). Like the other experiments at the Energetikum, these results should be seen as a first step to an application in real HVAC environments. After evaluating the results, the PCB sensor shows the same trend as the reference sensor proving the constant temperature mode in closed loop operation as the best choice. Surprisingly, the PCB sensor senses even lower flow velocities than the reference sensor but the exact value could not be evaluated due to the lack of a confident reference value. However, the major result of this measurement is that there was no detectable drift of the zero point over the recorded three days.

5.2 Conclusion

The absolute necessity to reduce the energy demand in buildings also targets the energy consumption for heating, ventilating, and air conditioning system. Modern buildings are accordingly designed so that HVAC systems operate in an optimized mode. However, in older, existing buildings this is not the case and the systems work inefficiently. To improve this unsatisfying status a rough determination of the actual flow distributions is needed. The volume flow rate has to be measured in the duct system at several strategic locations. With the knowledge of the cross-sections of the pipes only the mean flow velocity has to be measured. There are several sensors available but there is a severe lack of sensors which measure accurately enough, are easy to install and are suitable for mass production.

In this thesis, such a sensor was developed which can measure the mean flow velocities in HVAC systems. First, the condition in HVAC systems as well as suitable flowmeters are summarized. A suitable technology for this application was found in thermal flow sensors. In particular, the thermoresistive principle was chosen as thermoelectrical conversion because it needs no moving parts, is easy to install and exchange in pipes, is robust, accurate, reliable, and suits the requirements for mass production. As production technology, the printed board technology was chosen because it is a well-established technology for mass production in electronics and a thermoresistive sensor can be realized with it.

First, an analytical model was developed to obtain a qualitative understanding of the sensor. By using the energy conversation on an infinitesimal 3D slice in combination with several simplifications a differential equation of the sensor was deduced. Its solution reveals the excess temperature at the sensor spots as a function of the mean flow velocity. This excess temperature is symmetric around the heater without any flow and becomes more and more asymmetric with the rising flow velocity. When comparing the excess temperature at two spots up- and downstream of the heater as a function of the mean flow velocity, a typical feature of a calorimetric sensor was found which is the ambiguity of the output characteristic where an abrupt rise until the maximum followed by a slow decline. At additional lead locations the output characteristic was evaluated again. This can be used either for a higher sensibility or a wider measurement range depending on these locations. Nonetheless, the purpose of this model was to get a qualitative understanding of the sensor behavior.

Next, a 2D-FEM simulation with Comsol Multiphysics was developed where the conjugated heat transfer module was utilized which combines the heat transfer module with the laminar flow module. With the incompressible Navier-Stokes equation the velocity field inside the flow channel and around the sensor was evaluated and, then, the heat transfer equations incorporating conductive and convective heat transfer were solved. Two different operation modes of the sensor were simulated.

The first one was set up with constant heating where the mean inlet flow velocity was varied while constant heating was applied. In detail, the simulation was solved in two steps where the first one solves the laminar flow module stationary because the

flow velocity is not influenced by the heating power. Whereas, the second one solves the heat transfer module with a time dependent solver taking the velocity results from the first step. The results are the temperature distribution and the velocity field in the flow channel. With post processing algorithms the temperatures as well as its transients of each sensing lead were derived. The results of these simulations show the temperature change of the sensing leads depending on the flow velocity and confirm that the targeted transduction principle is feasible.

The other simulation regarded constant temperature model. Hence, parameter sweeps of the dissipated heat and the mean inlet flow velocity were set up where the solver calculated pressures, velocities, and temperatures. The mean inlet velocity was in the range from $0.1 - 10\,\mathrm{m/s}$ and the heating power in the range from $0 - 1.8\,\mathrm{W}$. The results were temperature matrices for each sensing lead. Next, a temperature difference (e.g. $2\,\mathrm{K}$) was defined between the average temperature of the inner and that of the outer leads and the needed heating power was evaluated. The result is the heater voltage as a function of the mean flow velocity which is monotonically increasing from $0 - 10\,\mathrm{m/s}$. The simulations revealed the transients of the sensing leads and required heating power for the constant heating mode as well as the feasibility of the constant temperature mode at the targeted velocity range.

Based on model and simulation results and with the specific restrictions of the producer, the layout of the sensor was designed. The applied fabrication process was based on flexible printed circuit technology and PIU-Printex GmbH was chosen as the manufacturer. The basis of the sensor was a conventional FR4 glass epoxy as dielectric substrate material with a thickness of $100 \pm 13\,\mu\mathrm{m}$ and it was fabricated by lamination. On the substrate a copper foil was laminated with an initial thickness of $18 \pm 3\,\mu\mathrm{m}$ at first, then $9 \pm 2.0\,\mu\mathrm{m}$, and $5 \pm 1.7\,\mu\mathrm{m}$ in the last design. The width of all leads was $100 \pm 5\,\mu\mathrm{m}$ which was the lowest possible limit of the manufacturer at this time. On top of the substrate with the copper leads a protective layer (polyimide film) was placed with a thickness of $30 \pm 10\,\mu\mathrm{m}$.

The design features one heating element in the middle and two sensing elements up- and downstream of the heater. Several designs were tested in which parameters like meander length, meander number, lead gap, holes, holes gap, and wing width were varied.

Next, measurements regarding the resistance of the sensor were performed. The difference between a soldered and plugged solution was tested to see how much the plug influences the measurements. As a result, the plug does not have any relevant influence during the measurements. After measuring the resistance values of all sensors, the sheet resistance for better comparison was evaluated. Additionally, the sheet resistance differences of the heater, inner and outer sensing leads, as well as left and right sensing leads were evaluated to obtain a detailed picture of the resolution and limits of the PCB technology. The outcome of these measurements is that for increasing the resolution the reproducibility of the copper leads and by association the sheet resistance has to be improved. Heating and cooling cycles have

been applied to the sensor which revealed its transient behavior when an accurate measurement is possible.

The next measurements characterized the behavior of the sensor at well-defined flow velocities. Therefore, an experimental flow channel with an acrylic glass pipe was created. The flow was established by suction with a double vane fan and the sensor was read out with a lock-in amplifier. The expected typical transduction behavior of a calorimetric sensor was measured. It was possible to tune the signal for either a higher sensitivity or a wider measurement range with different designs. However, it was not possible to extend the range to meet the specifications of typical HVAC systems which meant that another approach was necessary.

Electronics were developed to run the sensor in a constant temperature operation to increase the measurement range. Therefore, an analog PI-controller was designed which keeps the difference between the mean temperature at the middle of the sensor and the mean temperature at the periphery of the PCB at a constant level. As a result, the heating voltage becomes a function of the mean flow velocity which was measured in an experimental setup. These laboratory measurements verified the simulations but only in a limited measurement range. Therefore, the PCB sensor with the constant temperature mode was tested in a real HVAC environment. With this, the design was adapted to meet the dimension of the real HVAC environment requirements. While the accuracy of the reference sensor was not optimal, flow velocity and long term measurements were performed to prove the sensor principle feasible. Now, it is possible to measure the mean flow velocity of an old HVAC system over the range of $0 - 10\,\mathrm{m/s}$ with the new PCB sensor.

5.3 Outlook

There are many additional considerations needed before the new sensor is ready-to-use for the commercial sensor market. While it is not the main purpose of science to build such a final commercial product, it can provide essential knowledge and experience to achieve this goal.

First and foremost, the resolution of the PCB manufacturer is a key element to get more reproducible copper leads for one sensor. Through the revealed variations it is challenging to design readout electronics without the need of calibration. While high accuracy regarding resistance values is not needed, with technological advance and experience the resolution of the PCB will improve further allowing to manufacture more symmetric sensors with smaller lead resistance variation.

In this project, a flexible PCB was used for the sensor whereas a rigid PCB was used for the front-end electronics. It would be beneficial to place both functional parts on one PCB. The electronics could be placed onto the flexible PCB or a semiflex PCB may be used. The flexible part of the semiflex PCB acts as sensor and the rigid part will be used for the electronic components. There are several benefits putting these two things together. First, the overall costs of the sensors decrease dramatically because there will be only a single PCB which means fewer masks and process steps, faster manufacturing time, etc. Second, it is also possible to let the manufacturer solder the electronic components on the PCB. Hence, the interconnections between the sensor and the electronics will become shorter and plugs can be completely avoided. Third, because there is only a single part, the sensor installation becomes easier and faster. Finally, for large quantities the cost of one sensor will be so low that a damaged sensor can just be replaced with a new one.

A major goal is the integration of several PCB sensors into a big sensor network but this is beyond the scope of this thesis. Currently, one sensor was put into a sensor network at the Energetikum facility and connected to the ADC transmitter module. The idea was to read out the sensor wireless via a hub which is connected to the network. Therefore, a micro controller (µC) with the ability to communicate over a wireless protocol would be a feasible solution. For example, a simple algorithm starts with an initialization which wakes up the µC from a sleep modus as well as the front-ends. After a short delay the sensor will be read out and will convert the measured voltage into the corresponding flow velocity. After that, the µC sets up the communication with a wireless hub and sends the data to the hub. Finally, the algorithm will put the µC to sleep and shut down the front-ends.

In the presented work the front-end as well as the controller are implemented completely analog. Inserting a µC also allows digitalizing several parts of the controller. Most µC's already have several ADCs and DACs implemented with, for example, sigma-delta modulation. Therefore, only some amplifier µC's with passive components are needed as front-ends which decrease the amount of parts as well as space.

Another benefit of using a µC is the possibility to perform a calibration of the sensor. Currently, through the resistance differences of the copper leads, the amplifier electronics have to be manually adjusted. When the µC measures these resistance values, it can then calibrate the controller automatically. Therefore, the small influence of humidity or ambient pressure can be compensated. Moreover, this calibration can be repeated after a specific time interval to counter long time drifts, to compensate dirt on the sensor, or detect a damaged lead.

Other future tasks will be the improvement of both the model and the simulation by adapting them to more realistic conditions. Improvements for the model should target the heat source and the dissipated heating power as well as the symmetry of the sensor. Additionally, the infinitesimal 3D slice should be improved in a manner so that it does not only apply at the sensor in the pipe. The performed 2D simulation should be extended into 3D allowing for superior results. But 3D simulations are more complex and time consuming in terms of design, meshing and iteration processes for achieving convergent solutions which is shown for a similar problem by Suhaimi [120]. Assuming laminar flow may be reasonable for labor experiments with small cross-section dimensions, for real HVAC systems turbulences have to be taken into account as well. Comsol Multiphysics uses k-ε-turbulence models [121] for these turbulent streams. Furthermore, for improving accuracy it is possible to implement CFD (computational fluid dynamics) models [122] into heat transfer module in Comsol.

A critical issue in installing several sensors is the placement of the sensors in the duct system. While the sensor is stretched over the whole cross-section of the pipe, it does not cover the complete area of the pipe and at some positions, like after bends or branches, inevitable turbulences may not be recognized or can cause errors. Therefore, optimal strategic positions should be targeted. The first attempt was performed by Sauter [89].

With these PCB sensors it will be possible to recalibrate HVAC systems in old buildings to work properly again which will contribute to the urgent needed energy reduction. The sensors will be easily adapted to any pipe dimensions and installed very quickly not only in HVAC systems but also in any sort of pipe with streaming fluids. Moreover, the sensors are not limited to measure only air streams, they are able to work in different fluids, like water or oils, requiring only a little redesign of the sensing locations and front-ends. Due to the fact that the sensors are covered with a protective layer, they are able to measure in hazardous environments expanding their possible applications even more. These PCB Sensors are able to measure flow accurate enough while still being cost-effective and robust enough to allow the detection of inefficiency at a more superior rate than is currently possible.

Appendices

Appendix A

Sensor Geometries and Mounting Parts

In the following, geometrical dimensions of the developed sensors and their mounts are given.

A.1 Proof-of-concept

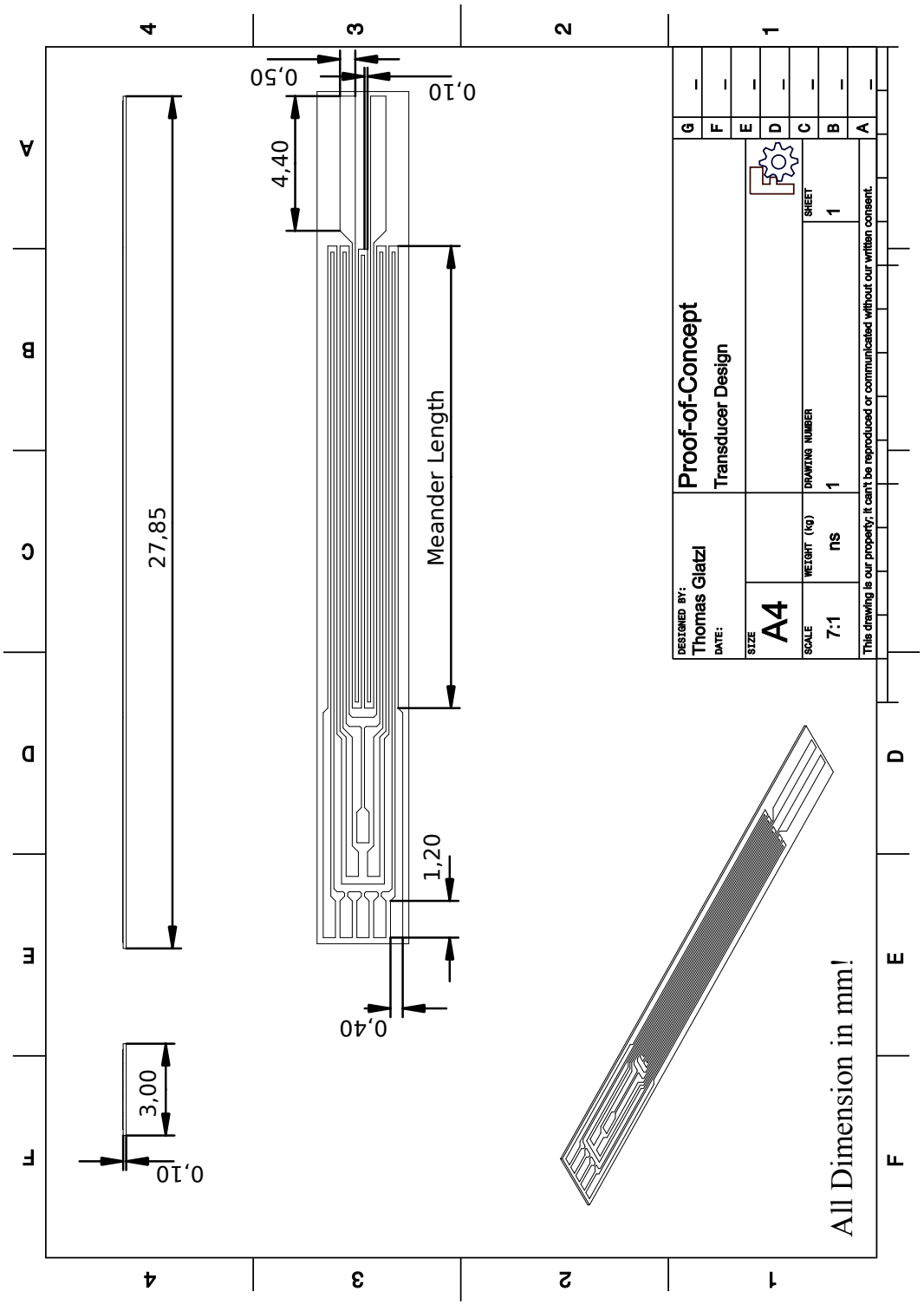

Figure A.1: CAD drawing of the proof-of-concept.

A.2 Prototype

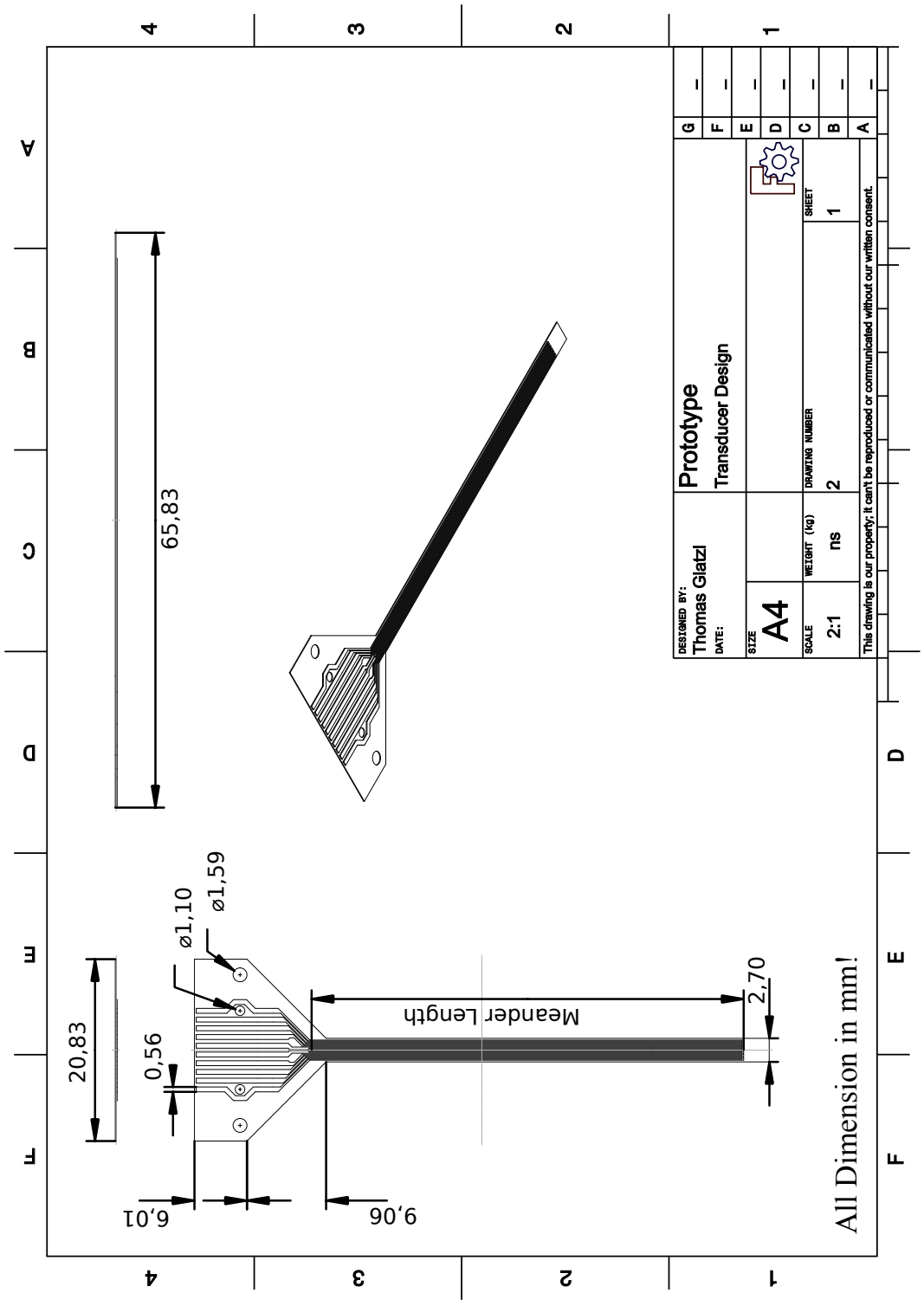

Figure A.2: CAD drawing of the prototype.

A.3 3D Printed parts for mounting the sensor

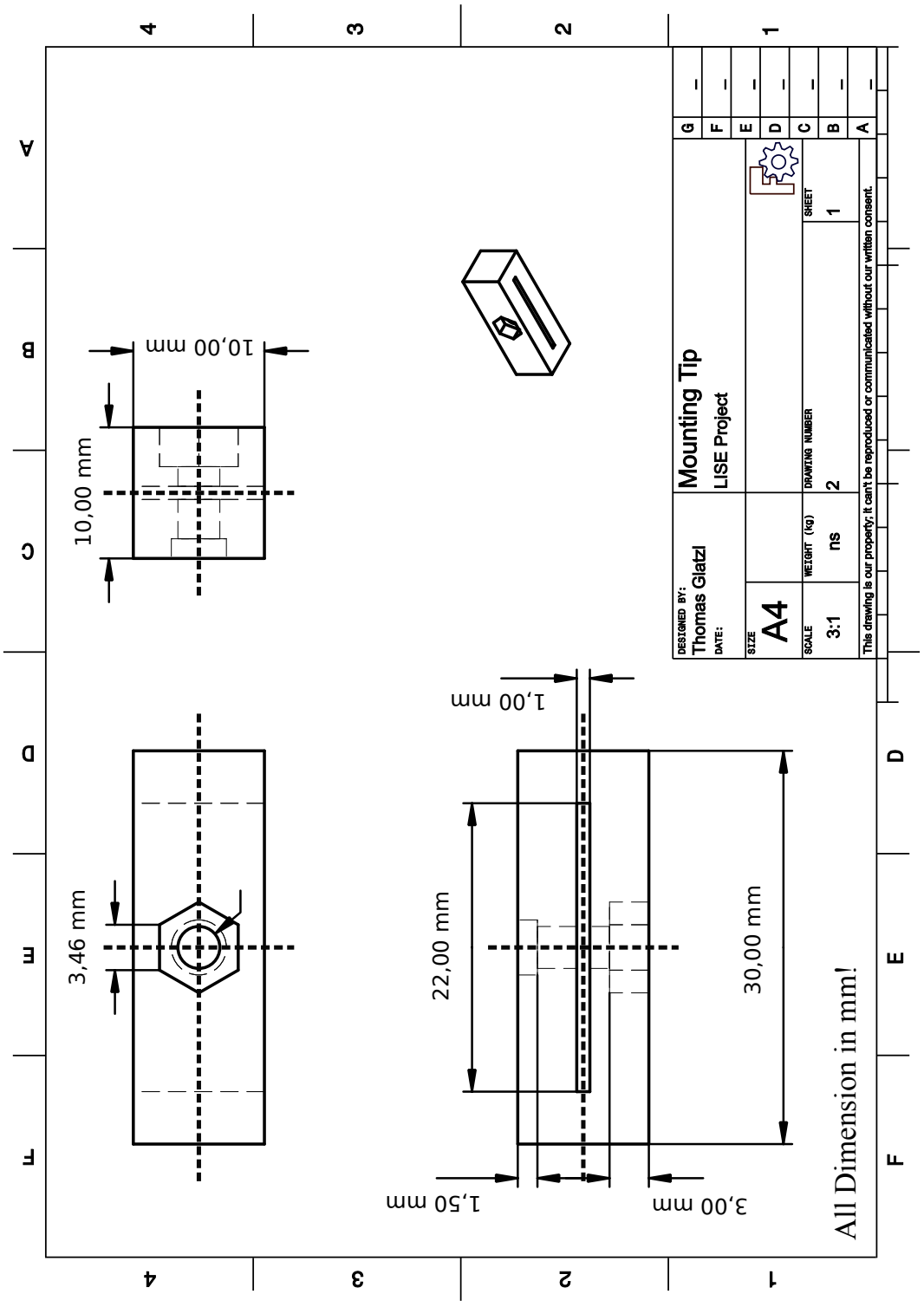

Figure A.3: Mount for the tip of the sensor

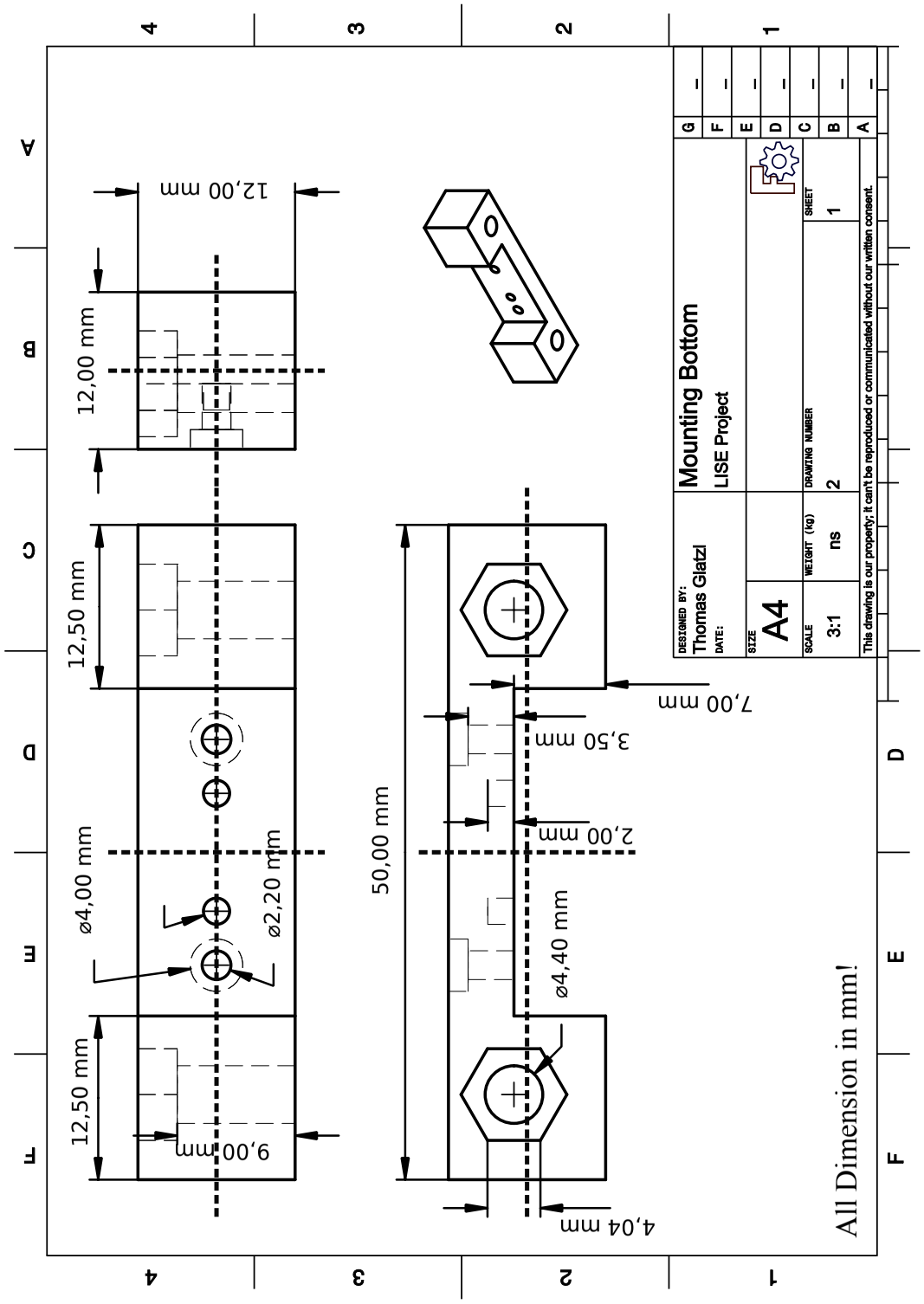

Figure A.4: Mount for the bottom of the sensor

Appendix B

Electronics

B.1 Schematics of the electronics

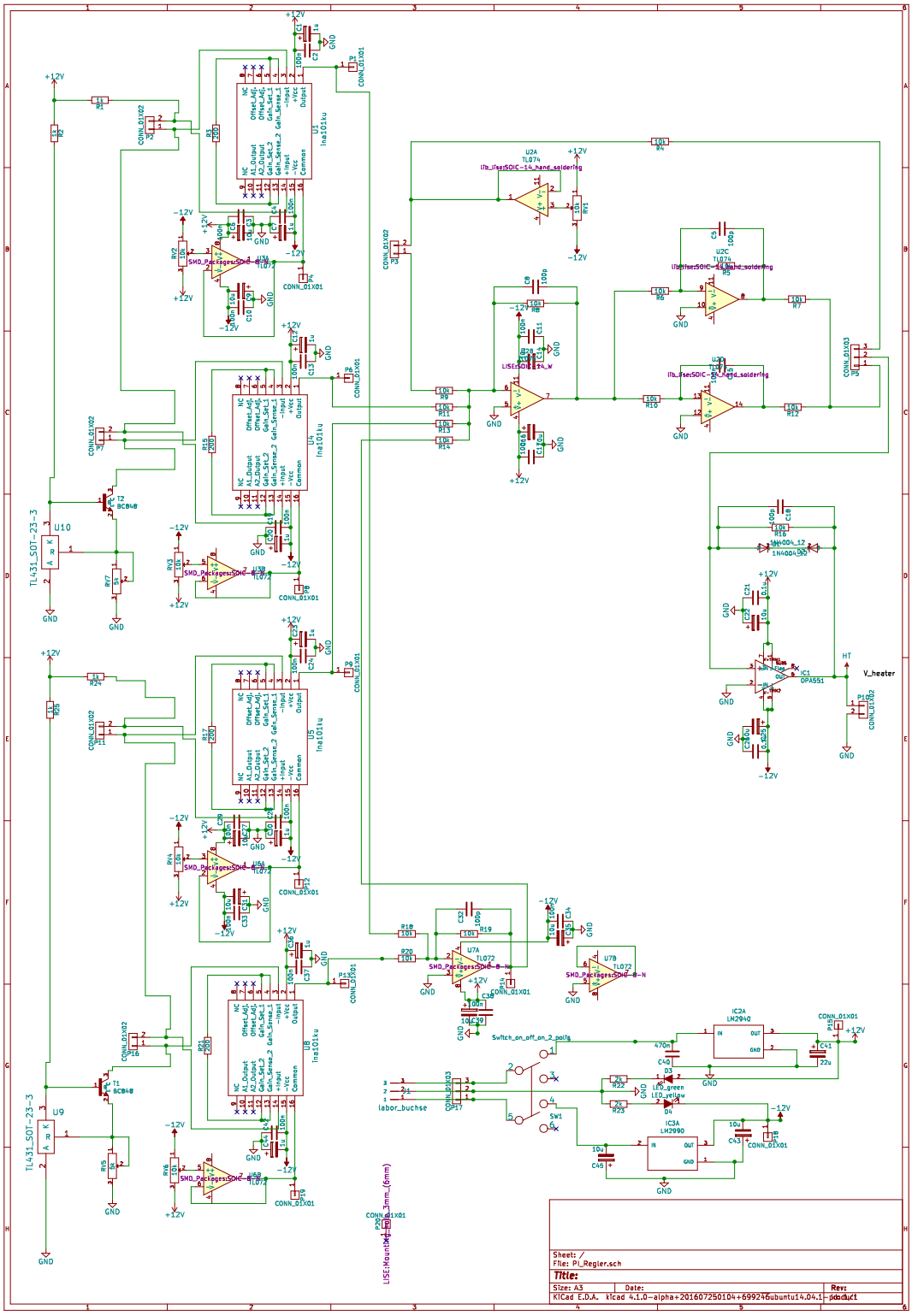

Figure B.1: Schematics of the electronics (front-ends, PI-controller, and supply) for the constant temperature mode.

Bibliography

[1] Constantinos A. Balaras, Athina G. Gaglia, Elena Georgopoulou, Sevastianos Mirasgedis, Yiannis Sarafidis, and Dimitris P. Lalas. European residential buildings and empirical assessment of the Hellenic building stock, energy consumption, emissions and potential energy savings. *Building and Environment*, 42(3):1298–1314, March 2007.

[2] Douglas Harris. *A Guide to Energy Management in Buildings*. Routledge, Abingdon, Oxon, Eng. ; New York, 1 edition edition, November 2011.

[3] EUR-Lex. Directive 2010/31/EU of the European Parliament and of the Council of 19 May 2010 on the energy performance of buildings. May 2010.

[4] European Environment Agency (EEA). Trends and projections in Europe 2015 - Tracking progress towards Europe's climate and energy targets. October 2015.

[5] Xiaodong Cao, Xilei Dai, and Junjie Liu. Building energy-consumption status worldwide and the state-of-the-art technologies for zero-energy buildings during the past decade. *Energy and Buildings*, 128:198–213, September 2016.

[6] Luis Perez-Lombard, Jose Ortiz, and Christine Pout. A review on buildings energy consumption information. *Energy and Buildings*, 40(3):394–398, January 2008.

[7] BREEAM. www.breeam.com. *Building Research Establishment Environmental Assessment Method*, 1990.

[8] HEQ. www.assohqe.org. *High Environmental Quality*, 1996.

[9] LEED. www.usgbc.org. *Leadership in Energy and Environmental Design was originated in the USA by the US Green Building Council (USGBC)*, 2000.

[10] CASBEE. www.ibec.or.jp/CASBEE/english/. *Comprehensive Assessment System for Built Environment Efficiency*, 2001.

[11] Ai Sheng. *Energy, Environment and Green Building Materials: Proceedings of the 2014 International Conference on Energy, Environment and Green Building Materials ... November 28-30, 2014, Guilin, Guangxi, China*. CRC Press, 2015.

[12] Angui Li, Yingxin Zhu, and Yuguo Li. *Proceedings of the 8th International Symposium on Heating, Ventilation and Air Conditioning: Volume 1: Indoor and Outdoor Environment: 261*. Springer, 2014 edition, September 2013.

[13] Shengwei Wang and Zhenjun Ma. Supervisory and Optimal Control of Building HVAC Systems: A Review. *HVAC&R Research*, 14(1):3–32, January 2008.

[14] Luis Perez-Lombard, Jose Ortiz, Juan F. Coronel, and Ismael R. Maestre. A review of HVAC systems requirements in building energy regulations. *Energy and Buildings*, 43(2):255–268, February 2011.

[15] Yu Huang and Jian-lei Niu. A review of the advance of HVAC technologies as witnessed in ENB publications in the period from 1987 to 2014. *Energy and Buildings*, 130:33–45, October 2016.

[16] Angui Li, Yingxin Zhu, and Yuguo Li. *Proceedings of the 8th International Symposium on Heating, Ventilation and Air Conditioning: Volume 2: HVAC&R Component and Energy System: 262*. Springer, 2014 edition, September 2013.

[17] K. J. Chua, S. K. Chou, W. M. Yang, and J. Yan. Achieving better energy-efficient air conditioning - A review of technologies and strategies. *Applied Energy*, 104:87–104, April 2013.

[18] Muhammad Waseem Ahmad, Monjur Mourshed, David Mundow, Mario Sisinni, and Yacine Rezgui. Building energy metering and environmental monitoring - A state-of-the-art review and directions for future research. *Energy and Buildings*, 120:85–102, May 2016.

[19] Luis Perez-Lombard, Jose Ortiz, and Ismael R. Maestre. The map of energy flow in HVAC systems. *Applied Energy*, 88(12):5020–5031, December 2011.

[20] Manabu Iguchi and Olusegun J. Ilegbusi. *Basic Transport Phenomena in Materials Engineering*. Springer Japan, Tokyo, 2014.

[21] Jesse Yoder and Dick Morley. *The Tao of Measurement: A Philosophical View of Flow and Sensors*. International Society of Automation, Place of publication not identified, February 2015.

[22] R. E. Oosterbroek, T. S. J. Lammerink, J. W. Berenschot, G. J. M. Krijnen, M. C. Elwenspoek, and A. van den Berg. A micromachined pressure/flow-sensor. *Sensors and Actuators A: Physical*, 77(3):167–177, November 1999.

[23] M. Richter, M. Wackerle, P. Woias, and B. Hillerich. A novel flow sensor with high time resolution based on differential pressure principle. In *Twelfth IEEE International Conference on Micro Electro Mechanical Systems, 1999. MEMS '99*, pages 118–123, January 1999.

[24] J. Lim, Q. P. Yang, B. E. Jones, and P. R. Jackson. DP flow sensor using optical fibre Bragg grating. *Sensors and Actuators A: Physical*, 92(1-3):102–108, August 2001.

[25] Y. Li, L. Cao, and Y. Wang. Design of gas turbine flowmeter based on the technology of automatic gain control. In *2015 IEEE International Conference on Mechatronics and Automation (ICMA)*, pages 392–396, August 2015.

[26] Gui-Bo Zheng, Ning-De Jin, Xiao-Hui Jia, Peng-Ju Lv, and Xing-Bin Liu. Gas - liquid two phase flow measurement method based on combination instrument of turbine flowmeter and conductance sensor. *International Journal of Multiphase Flow*, 34(11):1031–1047, November 2008.

[27] Roger C. Baker and M. Vivien Morris. Positive - displacement meters for liquids. *Transactions of the Institute of Measurement and Control*, 7(4):209–220, July 1985.

[28] Charlotte E. Morton, Roger C. Baker, and Ian M. Hutchings. Measurement of liquid film thickness by optical fluorescence and its application to an oscillating piston positive displacement flowmeter. *Measurement Science and Technology*, 22(12):125403, 2011.

[29] Tao Wang and Roger Baker. Coriolis flowmeters: a review of developments over the past 20 years, and an assessment of the state of the art and likely future directions. *Flow Measurement and Instrumentation*, 40:99–123, December 2014.

[30] R. M. Saravanan, Christ W. Raj, and M. Shanmugavalli. Design and Simulation of Coriolis Flow Tube in Meso and Micro Level to Determine Its Resonant Frequency. 2015.

[31] Zhiyong Li and Zhiqiang Sun. Development of the Vortex Mass Flowmeter with Wall Pressure Measurement. *Measurement Science Review*, 13(1):20–24, 2013.

[32] A. Venugopal, Amit Agrawal, and S. V. Prabhu. Note: A vortex cross-correlation flowmeter with enhanced turndown ratio. *Review of Scientific Instruments*, 85(6):066109, June 2014.

[33] A. Venugopal, Amit Agrawal, and S. V. Prabhu. Review on vortex flowmeter - Designer perspective. *Sensors and Actuators A: Physical*, 170(1-2):8–23, November 2011.

[34] L. C. Lynnworth and Yi Liu. Ultrasonic flowmeters: Half-century progress report, 1955-2005. *Ultrasonics*, 44, Supplement:e1371–e1378, December 2006.

[35] Fellipe Allevato Martins da Silva, Von Krueger, Marco Antonio, and Wagner Coelho de Albuquerque Pereira. Continuous flow phantom for the calibration of an ultrasonic transit-time flowmeter. *Revista Brasileira de Engenharia Biomedica*, 30(1):03–10, March 2014.

[36] Qiang Chen, Weihua Li, and Jiangtao Wu. Realization of a multipath ultrasonic gas flowmeter based on transit-time technique. *Ultrasonics*, 54(1):285–290, January 2014.

[37] C. W. Fernandes, M. D. Bellar, and M. M. Werneck. Cross - Correlation - Based Optical Flowmeter. *IEEE Transactions on Instrumentation and Measurement*, 59(4):840–846, April 2010.

[38] A. Bailleu. Ultrasonic transducer positioning system for clamp-on flowmeter applications. In *2016 IEEE Sensors Applications Symposium (SAS)*, pages 1–6, April 2016.

[39] Jae-Eun Cha, Yeh-Chan Ahn, Kyung-Woo Seo, Ho-Yun Nam, Jong-Hyun Choi, and Moo-Hwan Kim. An experimental study on the characteristics of electromagnetic flowmeters in the liquid metal two-phase flow. *Flow Measurement and Instrumentation*, 14(4-5):201–209, August 2003.

[40] T. Leeungculsatien and G.P. Lucas. Measurement of velocity profiles in multiphase flow using a multi-electrode electromagnetic flow meter. *Flow Measurement and Instrumentation*, 31:86–95, June 2013.

[41] R. Lhermitte and U. Lemmin. Open-Channel Flow and Turbulence Measurement by High-Resolution Doppler Sonar. *Journal of Atmospheric and Oceanic Technology*, 11(5):1295–1308, October 1994.

[42] R. Pinkel, M. Merrifield, J. Smith, and H. Ramm. Advances in Doppler sonar technology. In *, Proceedings of the IEEE Fifth Working Conference on Current Measurement, 1995*, pages 37–41, February 1995.

[43] Vinayakrishnan Rajan, Babu Varghese, Ton G. van Leeuwen, and Wiendelt Steenbergen. Review of methodological developments in laser Doppler flowmetry. *Lasers in Medical Science*, 24(2):269–283, January 2008.

[44] R. W. Wunderlich, R. L. Folger, D. B. Giddon, and B. R. Ware. Laser doppler blood flow meter and optical plethysmograph. *Review of Scientific Instruments*, 51(9):1258–1262, September 1980.

[45] Velocity in Ventilation Ducts. www.engineeringtoolbox.com, 2016.

[46] S. Cruz, J. C. Viana, D. Dias, and L. A. Rocha. Pressure sensing platform for health monitoring. In *Medical Measurements and Applications (MeMeA), 2014 IEEE International Symposium on*, pages 1–5. IEEE, 2014.

[47] Aneta Prijic, Ljubomir Vracar, Dusan Vuckovic, Dejan Milic, and Zoran Prijic. Thermal Energy Harvesting Wireless Sensor Node in AluminumCore PCB Technology. *IEEE Sensors Journal*, pages 1–1, 2014.

[48] Roumen Nojdelov and Stoyan Nihtianov. Capacitive sensor interface with improved dynamic range and stability. In *Instrumentation and Measurement Technology Conference (I2MTC) Proceedings, 2014 IEEE International*, pages 1373–1376. IEEE, 2014.

[49] J. C. Loetters, J. Groenesteijn, E. J. van der Wouden, W. Sparreboom, T. S. J. Lammerink, and R. J. Wiegerink. Fully integrated microfluidic measurement system for real-time determination of gas and liquid mixtures composition. In *2015 Transducers - 2015 18th International Conference on Solid-State Sensors, Actuators and Microsystems (TRANSDUCERS)*, pages 1798–1801, June 2015.

[50] Hai Nguyen Dac and Tuan Vu Quoc. Fluidic Capacitive Sensor for Detection of Air Bubble Inside Engine Lubricating Oil. 2015.

[51] Rene Petervari, Alexander Wagner, and Klaus Hannemann. Messung von Anstroemungsstoerungen in Hypersonischen Windkanaelen. pages 40–41, Goettingen, Deutschland, 2015.

[52] P. Arpaia, M. Buzio, O. Dunkel, M. D'Arco, S. Russenschuck, and G. Severino. Performance analysis of miniaturized PCB coils for small-aperture magnet qualification. In *2015 IEEE SENSORS*, pages 1–4, November 2015.

[53] K. C. Baby and N. Schwesinger. Design and fabrication of individualized capacitive microsensor for tilt measurement. In *2015 IEEE SENSORS*, pages 1–4, November 2015.

[54] Tim Williams. *The Circuit Designer's Companion*. Newnes, Oxford England; Boston, second edition edition, 2005.

[55] Joerg Scholz, Teresio Ricolfi, Wolfgang Goepel, Joachim Hesse, and J. N. Zemel. *Sensors - Volume 4: Thermal Sensors: A Comprehensive Survey*. Wiley-VCH, Weinheim, F.R.G.; New York, N.Y., USA, 1990.

[56] A. Ivanov, A. Besborodow, and G. Sattelberger. Lamination of 3d structures in LTCC using elastomer bags. In *2015 European Microelectronics Packaging Conference (EMPC)*, pages 1–6, September 2015.

[57] C. Xu, Q. Zhou, X. Guo, S. Zhan, B. Xiong, H. Jiang, and S. Liu. Analysis of measurement accuracy of air flow sensor influenced by moisture. In *2015 16th International Conference on Electronic Packaging Technology (ICEPT)*, pages 694–698, August 2015.

[58] W. Xu, B. Gao, S. Ma, A. Zhang, Y. Chiu, and Y. K. Lee. Low-cost temperature-compensated thermoresistive micro calorimetric flow sensor by using 0.35um CMOS MEMS technology. In *2016 IEEE 29th International Conference on Micro Electro Mechanical Systems (MEMS)*, pages 189–192, January 2016.

[59] Yousef Valizadeh Yaghmourali, Nima Ahmadi, and Ebrahim Abbaspour-sani. A thermal-calorimetric gas flow meter with improved isolating feature. *Microsystem Technologies*, March 2016.

[60] Kathleen De Kerpel, Sven De Schampheleire, Timothy De Keulenaer, and Michel De Paepe. Two-phase frictional pressure drop and flow behaviour up- and downstream of a sharp return bend. *Applied Thermal Engineering*, 93:824–838, January 2016.

[61] Almudena Rivadeneyra, Jose Fernandez-Salmeron, Manuel Agudo-Acemel, Juan A. Lopez-Villanueva, Alberto J. Palma, and Luis Fermin Capitan-Vallvey. A printed capacitive-resistive double sensor for toluene and moisture sensing. *Sensors and Actuators B: Chemical*, 210:542–549, April 2015.

[62] Daisuke Nagai, Maiko Nishibori, Toshio Itoh, Tsutomu Kawabe, Kazuo Sato, and Woosuck Shin. Ppm level methane detection using micro-thermoelectric gas sensors with Pd/Al2o3 combustion catalyst films. *Sensors and Actuators B: Chemical*, 206:488–494, January 2015.

[63] H. Steiner, T. Glatzl, A. Talic, S. Cerimovic, F. Kohl, M. Schlauf, T. Schalkhammer, F. Keplinger, and T. Sauter. Towards low-cost printed flow sensors. In *2015 IEEE SENSORS*, pages 1–4, November 2015.

[64] K. A. A. Makinwa and J. H. Huijsing. A 2nd order thermal sigma-delta modulator for flow sensing. In *IEEE Sensors, 2005.*, pages 4 pp.–, October 2005.

[65] Gerard C. M. Meijer. Thermal sensors based on transistors. *Sensors and Actuators*, 10(1-2):103–125, September 1986.

[66] J. B. Sun, M. Qin, and Q. A. Huang. Flip-Chip Packaging for a Two-Dimensional Thermal Flow Sensor Using a Copper Pillar Bump Technology. *IEEE Sensors Journal*, 7(7):990–995, July 2007.

[67] Chun-Ching Hsiao and Sheng-Yi Liu. Multi-Frequency Band Pyroelectric Sensors. *Sensors*, 14(12):22180–22198, November 2014.

[68] Jan Kielbasa. Measurement of gas flow velocity: Anemometer with a vibrating hot wire. *Review of Scientific Instruments*, 81(1):015101, January 2010.

[69] Paperback. *Physik Formelsammlung fuer Ingenieure und Naturwissenschaftler. Mit Anwendungen und Beispielen aus Technik*. Wiesbaden, 2008.

[70] Roman U. Sexl, John Blackmore, and Ludwig Boltzmann. *Gesamtausgabe / Internationale Tagung, 5.-8. September 1981: AusgewÃ€hlte Abhandlungen*. Akademische Druck- u. Verlagsanstalt, Graz, 1982.

[71] Minoru Nagai. *Thinking Fluid Dynamics With Dolphins*. Ios Pr Inc, Tokyo : Amsterdam, March 2002.

[72] Ernst Doering, Herbert Schedwill, and Martin Dehli. *Grundlagen der Technischen Thermodynamik*. Vieweg+Teubner Verlag, Wiesbaden, 2012.

[73] Peter von Boeckh and Thomas Wetzel. *Waermeuebertragung*. Springer Berlin Heidelberg, Berlin, Heidelberg, 2014.

[74] Ekbert Hering, Rolf Martin, Martin Stohrer, W. Schulz, and G. Kurz. *Physik fuer Ingenieure*. Springer, Berlin u.a., auflage: 10., vollst. neu bearb. aufl. edition, July 2007.

[75] Paul A. Tipler and Gene Mosca. *Physik*. Springer Berlin Heidelberg, Berlin, Heidelberg, 2015.

[76] Heinz Herwig and Andreas Moschallski. *Waermeuebertragung*. Springer Fachmedien Wiesbaden, Wiesbaden, 2014.

[77] Wilhelm Nusselt. *Das Grundgesetz des Waermeueberganges*. 1915.

[78] Frank White. *Viscous Fluid Flow*. McGraw-Hill Education, New York, NY, 3 edition edition, January 2005.

[79] Walter Wagner. *Waermeuebertragung: Grundlagen*. Vogel, Wuerzburg, 1991.

[80] Stuart W. Churchill. A comprehensive correlating equation for laminar, assisting, forced and free convection. *AIChE Journal*, 23(1):10–16, January 1977.

[81] S. Middelhoek, K. Cammann, R. Puers, N. T. Nguyen, and W. Doetzel. Asymmetrical locations of heaters and sensors relative to each other using heater arrays: a novel method for designing multi-range electrocaloric mass-flow sensors. *Sensors and Actuators A: Physical*, 62(1):506–512, July 1997.

[82] P. Rudent, P. Navratil, A. Giani, and A. Boyer. Design of a new sensor for mass flow controller using thin-film technology based on an analytical thermal model. *Journal of Vacuum Science & Technology A*, 16(6):3559–3563, November 1998.

[83] Nam-Trung Nguyen. A novel thermal sensor concept for flow direction and flow velocity. *IEEE Sensors Journal*, 5(6):1224–1234, December 2005.

[84] Hermann Schlichting and Klaus Gersten. *Grenzschicht-theorie*. Springer-Verlag, 2006.

[85] Almir Talic, Samir Cerimovic, Roman Beigelbeck, Franz Kohl, Thilo Sauter, and Franz Keplinger. MEMS Flow Sensors Based on Self-Heated aGe-Thermistors in a Wheatstone Bridge. *Sensors*, 15(5):10004–10025, April 2015.

[86] COMSOL. *Multiphysics Reference Manual*. www.comsol.com, Page 280, 1998.

[87] Thomas Glatzl, Franz Kohl, Wilfried Hortschitz, and Thilo Sauter. Concept of a thermal flow sensor integration on circuit board level. In *Emerging Technologies & Factory Automation (ETFA), 2013 IEEE 18th Conference on*, pages 1–4, 2013.

[88] Thilo Sauter, Thomas Glatzl, Franz Kohl, Harald Steiner, and Almir Talic. Thermal flow sensors based on printed circuit board technology. In *Quality Electronic Design (ISQED), 2014 15th International Symposium on*, pages 748–753. IEEE, 2014.

[89] T. Sauter, H. Steiner, T. Glatzl, W. Hortschitz, F. Wenig, and C. Heschl. Towards distributed enthalpy measurement in large-scale air conditioning systems. In *Systems Conference (SysCon), 2015 9th Annual IEEE International*, pages 460–465, April 2015.

[90] Clyde F. Coombs. *Printed Circuits Handbook*. Mcgraw-Hill Education - Europe, New York, 7 rev ed. edition, 2016.

[91] William F. Leonard and Ho-Yuan Yu. Thermoelectric power of thin copper films. *Journal of Applied Physics*, 44(12):5320–5323, December 1973.

[92] Yasunari Maekawa, Hiroshi Koshikawa, and Masaru Yoshida. Anisotropically conducting films consisting of sub-micron copper wires in the ion track membranes of poly(ethylene terephthalate). *Polymer*, 45(7):2291–2295, March 2004.

[93] Wilfried Weissgerber. *Elektrotechnik fuer Ingenieure 1: Gleichstromtechnik und Elektromagnetisches Feld. Ein Lehr- und Arbeitsbuch fuer das Grundstudium*. Springer Vieweg, Wiesbaden, 10 edition, August 2015.

[94] Jack P. Holman. *Heat Transfer*. Science Engineering & Math, 10 edition, January 2009.

[95] A. L. C. FUJARRA, C. P. PESCE, F. FLEMMING, and C. H. K. WILLIAMSON. VORTEX-INDUCED VIBRATION OF A FLEXIBLE CANTILEVER. *Journal of Fluids and Structures*, 15(3):651–658, April 2001.

[96] Chang Liu, Jin-Biao Huang, Zhenjun Zhu, Fukang Jiang, S. Tung, Yu-Chong Tai, and Chih-Ming Ho. A micromachined flow shear-stress sensor based on thermal transfer principles. *Journal of Microelectromechanical Systems*, 8(1):90–99, March 1999.

[97] C.H.K. Williamson and and R. Govardhan. Vortex-Induced Vibrations. *Annual Review of Fluid Mechanics*, 36(1):413–455, 2004.

[98] John Stewart. *Python for scientists*. Cambridge University Press, Cambridge, 2014.

[99] Andrew Collette. *Python and HDF5*. O'Reilly and Associates, Beijiing, 1 edition, November 2013.

[100] Anthony J. Caristi. *IEEE-488 General Purpose Instrumentation Bus Manual: General Purpose Instrumentation Bus Manual-488*. Academic Press Inc, San Diego, February 1989.

[101] Andrew colette. HDF5 for Python, 2015.

[102] Mike Folk. The HDF Group - Information, Support, and Software, 2015.

[103] http://www.keysight.com. Keysight True volt Series Digitale Multimeter, 2015.

[104] Dieter K. Schroder. *Semiconductor material and device characterization*. IEEE Press ; Wiley, [Piscataway, NJ] : Hoboken, N.J, 3rd ed edition, 2006.

[105] T. Sauter, T. Glatzl, S. Cerimovic, F. Kohl, H. Steiner, and A. Talic. PCB-integrated flow sensors - How good is state of the art technology? In *2016 IEEE International Instrumentation and Measurement Technology Conference Proceedings*, pages 1–5, May 2016.

[106] Afzal Khan. *Introduction to Electrical , Electronics and Communication Engineering*. Firewall Media, December 2005.

[107] F. Soukup. Lock-in amplifiers. *Ceskoslovensky Casopis pro Fyziku Sekce*, 28:271–274, 1978.

[108] Thomas Glatzl, Harald Steiner, Franz Kohl, Thilo Sauter, and Franz Keplinger. Development of an air flow sensor for heating, ventilating, and air conditioning systems based on printed circuit board technology. *Sensors and Actuators A: Physical*, 237:1–8, January 2016.

[109] T. Glatzl, H. Steiner, F. Kohl, F. Keplinger, and T. Sauter. Thermal Flow Sensor based on Printed Circuit Board Technology for Ventilation and Air Conditioning Systems. *Procedia Engineering*, 87:1342–1345, 2014.

[110] T. Glatzl, H. Steiner, F. Kohl, T. Sauter, and F. Keplinger. Characterization and optimization of a thermal flow sensor on circuit board level. In *2014 IEEE Emerging Technology and Factory Automation (ETFA)*, pages 1–7, September 2014.

[111] Thomas Glatzl, Samir Cerimovic, Harald Steiner, Almir Talic, Roman Beigelbeck, Artur Jachimowicz, Thilo Sauter, and Franz Keplinger. Development of Flow Sensors Realized with Printed Circuit Board Technology for Air Conditioning Systems. *Measurement Fair SENSOR+TEST*, May 2015.

[112] Texas Instrument. INA101, 2000.

[113] G. B. Clayton and Steve Winder. *Operational Amplifiers, Fifth Edition*. Newnes, Oxford ; Boston, 5 edition edition, August 2003.

[114] Holger Lutz and Wolfgang Wendt. *Taschenbuch der Regelungstechnik: mit MATLAB und Simulink*. Deutsch, Frankfurt am Main, 2007.

[115] Serge Zacher and Manfred Reuter. *Regelungstechnik fuer Ingenieure Analyse, Simulation und Entwurf von Regelkreisen*. Imprint: Springer Vieweg, Wiesbaden, 2014.

[116] Alexander Weinmann. *Regelungen. Analyse und technischer Entwurf: Band 1: Systemtechnik linearer und linearisierter Regelungen auf anwendungsnaher Grundlage*. Springer, 3., ueberarb. u. erw. aufl. edition edition, September 1994.

[117] Alexander Weinmann. *Regelungen. Analyse und technischer Entwurf: Band 2: Multivariable, digitale und nichtlineare Regelungen; optimale und robuste Systeme*. Springer, 3., ueberarb. u. erw. aufl. edition edition, January 1995.

[118] Alexander Weinmann. *Regelungen Analyse und technischer Entwurf: Band 3: Rechnerische Loesungen zu industriellen Aufgabenstellungen*. Springer, softcover reprint of the original 1st ed. 1986 edition edition, December 2011.

[119] Jan Lunze. *Regelungstechnik. 1, 1,*. Springer, Berlin [u.a.], 2007.

[120] Misha Suhaimi. Comparison between 2d and 3d simulations of a tray dryer system using CFD software. *World Applied Sciences Journal*, 29(10):1301–1309, 2014.

[121] B Mohammadi and Olivier Pironneau. *Analysis of the K-epsilon turbulence model*. Wiley ; Masson, Chichester; New York; Paris, 1994. OCLC: 31606749.

[122] David C. Wilcox. *Turbulence Modeling for CFD*. D C W Industries, La Canada, Calif., 3rd edition edition, November 2006.

[123] Andrew Zimmerman Jones. Third Law of Thermodynamics, June 2014.

[124] Jochen Kuntner. *Oil condition monitoring using physical chemosensors*. 2008.

[125] Craig A. Grimes, Elisabeth C. Dickey, and Michael V. Pishko. Encyclopedia of Sensors. volume 10, pages 203–217. ASP, 2006.

[126] J.P. Holman. *Thermodynamics*. Mcgraw-Hill College, 4th edition, January 1988.

[127] Reinhard Hentschke. *Thermodynamics: For Physicists, Chemists and Materials Scientists*. Springer, auflage: 2014 edition, 2013.

[128] Klaus Fitzner. *Raumklimatechnik*, volume 2. Springer, 16. edition, 2008.

[129] J.P. Holman. *Heat Transfer*. Schaum's Outline Series. McGraw-Hill, Inc. (New York), 8th edition, November 1996.

[130] S. A. Korneyev. The joint analysis of general aspects of the phenomenological thermodynamics and the kinetic Boltzmann theory. *INTERNATIONAL JOURNAL OF HEAT AND MASS TRANSFER*, 45(17), 2002.

[131] PARA QUITARlE El POlVO. Conservation of Energy. *educacion quimica*, page 160, 2008.

[132] Andrew Zimmerman Jones. First Law of Thermodynamics, June 2014.

[133] Andrew Zimmerman Jones. Zeroeth Law of Thermodynamics, June 2014.

[134] Andrew Zimmerman Jones. Second Law of Thermodynamics, June 2014.

[135] Sanford Klein and Gregory Nellis. *Thermodynamics*. Cambridge University Press, New York, 2011.

[136] Dun Yu, H. Y. Hsieh, and J. N. Zemel. Microchannel pyroelectric anemometer. *Sensors and Actuators A: Physical*, 39(1):29–35, September 1993.

[137] Shrinivas G. Joshi. Flow sensors based on surface acoustic waves. *Sensors and Actuators A: Physical*, 44(3):191–197, September 1994.

[138] Doreen Kalz and Jens Pfafferott. *Thermal Comfort and Energy-Efficient Cooling of Non-residential Buildings*. Springer, New York, 2014 edition edition, March 2014.

[139] Javad Khazaii. *Energy-Efficient HVAC Design: An Essential Guide for Sustainable Building*. Springer, New York, 2014 edition edition, October 2014.

[140] Angui Li, Yingxin Zhu, and Yuguo Li. *Proceedings of the 8th International Symposium on Heating, Ventilation and Air Conditioning: Volume 3: Building Simulation and Information Management: 263*. Springer, 2014 edition, September 2013.

[141] Javad Khazaii. *Energy-Efficient HVAC Design: An Essential Guide for Sustainable Building*. Springer, 2014 edition, November 2014.

[142] M. Javdanitehran, R. Hoffmann, J. Groh, M. Vossiek, and G. Ziegmann. Effect of embedded printed circuit board (PCB) sensors on the mechanical behavior of glass fiber-reinforced polymer (GFRP) structures. *Smart Materials and Structures*, 25(6):065016, 2016.

[143] Wen-Chi Lin and Mark A. Burns. Low-power micro-fabricated liquid flow-rate sensor. *Anal. Methods*, 7(9):3981–3987, 2015.

[144] M. Shikida, Y. Yamazaki, K. Yoshikawa, and Kazuo Sato. A MEMS flow sensor applied in a variable-air-volume unit in a building air-conditioning system. *Sensors and Actuators A: Physical*, 189:212–217, January 2013.

[145] Hermann Schlichting. *Boundary-layer theory*. McGraw-Hill series in mechanical engineering. McGraw-Hill, New York, 7th ed edition, 1979.

[146] Hermann Schlichting. *Boundary-layer theory*. McGraw-Hill series in mechanical engineering. McGraw-Hill, New York, 7th ed edition, 1979.

[147] Brook W. Abegaz, Tania Datta, and Satish M. Mahajan. Sensor technologies for the energy-water nexus - A review. *Applied Energy*.

[148] Raghbir Singh Khandpur. *Printed Circuit Boards: Design, Fabrication, and Assembly*. Mcgraw Hill/Irwin Professional, New York, September 2005.

[149] J. B. Johnson. Thermal Agitation of Electricity in Conductors. *Physical Review*, 32(1):97–109, July 1928.

[150] H. Nyquist. Thermal Agitation of Electric Charge in Conductors. *Physical Review*, 32(1):110–113, July 1928.

[151] homeworkhelp classof1. *Calculation of Maximum Root Mean Square of the Error Source*.

[152] Analog Devices. AD630, 2015.

[153] Xiao-li ZHU and Xia LI. The Design of Dual-Phase Lock-In Amplifier Based on AD630. *Mechanical & Electrical Engineering Technology 6*, 2012.

[154] Heinrich Holland. *Grundlagen der Statistik*. Gabler Verlag, Place of publication not identified, 2 edition, 2013.

[155] *Waermeuebertragung*. Springer Berlin Heidelberg, 2006. DOI: 10.1007/3-540-31433-4_1.

[156] Albert Ernest Dunstan and Ferdinand Bernard Thole. *The Viscosity of Liquids*. BiblioLife, November 2009.

[157] Thomas Glatzl, Samir Cerimovic, Harald Steiner, Almir Talic, Artur Jachimowicz, Thilo Sauter, and Franz Keplinger. Novel PCB-based Thermal Flow Sensors for Air Conditioning Systems. In *IEEE Sensors*, pages 299–302. IEEE Sensors, November 2015.

[158] Thomas Glatzl, Samir Cerimovic, Harald Steiner, Almir Talic, Roman Beigelbeck, Artur Jachimowicz, Thilo Sauter, and Franz Keplinger. Development of Flow Sensors Realized with Printed Circuit Board Technology for Air Conditioning Systems, May 2015.

[159] M. Stifter, H. Steiner, W. Hortschitz, T. Sauter, T. Glatzl, A. Dabsch, and F. Keplinger. MEMS mu-wire magnetic field detection method@CERN. In *2015 IEEE SENSORS*, pages 1–4, November 2015.

[160] Thomas Glatzl, Samir Cerimovic, Harald Steiner, Almir Talic, Roman Beigelbeck, Artur Jachimowicz, Thilo Sauter, and Franz Keplinger. Hot-film and calorimetric thermal air flow sensors realized with printed board technology. *Journal of Sensors and Sensor Systems*, 5(2):283–291, July 2016.

[161] M. Stifter, H. Steiner, W. Hortschitz, T. Sauter, T. Glatzl, A. Dabsch, and F. Keplinger. MEMS micro-Wire Magnetic Field Detection Method at CERN. *IEEE Sensors Journal*, PP(99):1–1, 2016.

[162] Glatzl Thomas. Concept of a thermal flow sensor integration on circuit board level, 2013.

[163] T. Sauter, S. Cerimovic, T. Glatzl, H. Steiner, A. Talic, and F. Kohl. Using PCB technology for calorimetric water flow sensing in HVAC systems - a feasibility study. In *2016 IEEE 25th International Symposium on Industrial Electronics (ISIE)*, pages 662–667, June 2016.

[164] NOVEL LOW - COST THERMAL AIR FLO W SENSOR AND ITS APPLICATION IN HVAC SYSTEMS. *Indoor Climate of Buildings 2016*.

Acknowledgements

Although, I wrote this thesis myself, various people have been involved over the years to make this possible. Therefore, I would like to take the opportunity to acknowledge those people who helped me finish this work and who have made an indelible impression on my career and private life.

My deep appreciation goes to my supervisor Prof. Franz Keplinger of the Institute of Sensor and Actuator Systems. He always spared time for me and without his support, guidance, and advice, this thesis would not have been possible. He may be very strict in creating figures and diagrams for publications but his suggestions have greatly improved the quality of my scientific work. I would also like to thank Dr. Franz Kohl for his guidance, sharing his large experience, and his unmatched technical understanding. He is an inspiring example in academia.

My sincere gratitude goes to Dr. Hubert Brückl for kindly agreeing to be my co-supervisor and referee of my PhD-defense as well as to Dr. Thomas Schrefl for his report. I am grateful to Dr. Thilo Sauter who was the project leader of the research projects as well as to Roman Beigelbeck for his continual support and helping hand whenever I need it. A big thank you to Marcella Sigmund for correcting this thesis regarding the English language.

Lovely thanks to all of my colleagues at the Center of Integrated Sensor Systems. Especially to Elisabeth Schiefer who is our protective lioness and who has always an open ear for everyone and everything. Of course I have to sincerely thank Harald Steiner, Wilfried Hortschitz, Michael Stifter, Astrit Shoshi, and Alexander Kovacs for making work a place to fear and laugh at the same time. Everyday is an infernal pleasure working with them!!

A kindly thank you to the colleagues from the University of Applied Science Burgenland for helping me with the measurements, definitely worth mentioning are Florian Wenig and Dr. Christian Heschl. Also, a little thank you to several students who aided me at painful time-consuming measurements, Tobias Seewald should be noted here.

A sporty thank you to the SV Weikersdorf and all people in association with it. It is not only a place to play football and have a beer, it is a place where I can spend time outside in fresh air, have useless conversations, and reset my mind. Additionally, a lovely thank you to all trainers from sportsunlimited which made me as fit as a fiddle in the past years.

I am thankful to my family and friends for their support during the recent years. Some shine out like the family Hofstätter or the three others of the "Fantastic Four": Roman Fichtl, Martin Perka, and Gregor Zehrer.

To Lisa, my little sister, I do not know what do say because a simple thank you would not be enough. She is always there for me even putting my needs before hers which I definitely do not deserve. I am very lucky and proud to have her at my side.

Last but not least, I would like to wholeheartedly thank my parents, Marion and Erwin Glatzl. They have given a child the greatest gift it can ever receive, unending love and support in every possible way, so it can fully live out its passion.

"The man who honors his teacher honors himself."

About the Author

Thomas Glatzl

was born on the 2nd of January 1987 in Wiener Neustadt. After graduating with distinction from secondary collage (Höhere technische Bundes- Lehr- und Versuchsanstalt Wiener Neustadt - Elektrotechnik, Ausbildungsschwerpunkt Informationstechnik), he studied mechatronics/microsystems at the University of Applied Sciences Wiener Neustadt, receiving is master degree in 2011. The research topic of his master thesis was in the field of integrated circuit design where he developed a FPGA based evaluation system for digital motor control. Between 2012 and 2013 he was affiliated with the Institute of Integrated Sensor Systems (Austrian Academy of Science). In particular, he worked in the field of thermal flow sensors based on printed circuit board and silk screen printing technology. Since 2011 he was with the Institute of Sensor and Actuator systems (Vienna University of Technology), pursuing a Ph.D. degree. Currently, he is with the Center of Integrated Sensor Systems (Danube University Krems), working in the field of micro and nano sensors.